Challenges in the Characterization of Bottom-Up Fabricated Graphene Nanoribbons Addressed by *Ab Initio* Simulations

Dissertation
zur
Erlangung der naturwissenschaftlichen Doktorwürde
(Dr. sc. nat.)
vorgelegt der
Mathematisch-naturwissenschaftlichen Fakultät
der
Universität Zürich

von
Leopold Talirz
aus
Deutschland

Promotionskomitee

Prof. Dr. Jürg Hutter (Vorsitz)
Prof. Dr. Jürg Osterwalder
Prof. Dr. Oleg V. Yazyev
Dr. Carlo A. Pignedoli (Leitung der Dissertation)

Zürich, 2015

Contents

Abstract

Graphene is a promising material for high-frequency electronics on flexible substrates. Its wider technological application, however, is hampered by the complete lack of an electronic band gap. The bottom-up fabrication of nanometer-wide stripes of graphene by assembly of molecular precursors on metal surfaces solves this problem and meets the extreme requirements on structural quality. Since the first successful demonstration of this approach in 2010, significant progress has been made in the characterization of the atomic and electronic structure of these graphene nanoribbons (GNRs), often aided by computer simulations of the experimentally investigated systems. This thesis reports on some of these advances made possible by the combination of scanning tunneling microscopy (STM) experiments with complementary *ab initio* simulations.

The atomic and electronic structure found at the termini of bottom-up fabricated GNRs is addressed by large-scale density functional theory (DFT) simulations that include the metal substrate. Through comparison with experiments, the exact atomic structure at the termini is pinned down, providing insight into possible obstacles during the synthesis procedure. The dependence of the electronic band gap on the termination as well as the GNR length is investigated within tight binding and DFT and compared with experimental findings. Furthermore, the band structures of selected graphene nanoribbons with armchair edges are computed within DFT and many-body perturbation theory, focusing in particular on their representation in Fourier-transformed scanning tunneling spectroscopy (FT-STS) experiments. It is shown that the tip-sample distance plays a decisive role in defining the strength and the spatial distribution of the signal arising from different bands, making the direct interpretation of experimental spectra challenging. The comparison with *ab initio* FT-STS simulations, however, provides a consistent rationalization of the experimental data, rendering FT-STS a highly accurate method to determine the band gap and the band dispersion of GNRs on metal substrates. Finally, the electronic structure at graphene zigzag edges is discussed from a theoretical point of view and compared to recent experiments, indicating that the study of their intrinsic electronic structure is possible only after electronic decoupling from the metal surface.

Kurzfassung

Graphen ist ein vielversprechendes Material für Hochfrequenz-Schaltungen auf flexiblen Substraten. Das Fehlen einer elektronischen Bandlücke erschwert jedoch den Einsatz von Graphen in vielen Technologiebereichen. Die Synthese von Graphen-Bändern mit wenigen Nanometern Breite durch gezielte Verknüpfung einzelner Moleküle auf Metalloberflächen löst dieses Problem und erfüllt die damit verbundenen extremen Anforderungen an strukturelle Präzision. Seit der ersten Vorstellung dieser Methode im Jahre 2010 ist die Charakterisierung der atomaren und elektronischen Eigenschaften dieser Graphen-Nanobänder (GNBs) bedeutend fortgeschritten. Die vorliegende Arbeit beschreibt einige dieser Fortschritte, die durch das Zusammenspiel von Rastertunnelmikroskopie mit komplementären *ab initio* Simulationen ermöglicht wurden.

Die atomare und elektronische Struktur an den *Enden* der GNBs wird mithilfe der Dichtefunktionaltheorie (DFT) untersucht, unter Berücksichtigung der Einflüsse eines metallischen Substrats. Der direkte Vergleich mit dem Experiment ermöglicht die exakte Bestimmung der atomaren Struktur und gewährt Einsicht in mögliche Hürden in der Synthese. Die Abhängigkeit der elektronischen Bandlücke von der Terminierung und Länge der GNBs wird mittels der „tight binding Methode“ sowie der DFT berechnet und mit experimentellen Befunden verglichen. Weiter wird die elektronische Bandstruktur spezifischer GNBs mit „armchair“ Rändern mittels DFT sowie Vielteilchen-Störungstheorie berechnet, mit speziellem Augenmerk auf ihrer Darstellung in Fourier-transformierter Rastertunnelspektroskopie (FT-RTS). Es wird gezeigt, dass der Abstand zwischen Spitze und Substrat sowohl in Bezug auf die örtliche Verteilung als auch auf die relative Stärke des experimentellen Signals verschiedener Bänder eine entscheidende Rolle spielt. Dies erschwert die direkte Interpretation experimenteller Spektren. Der Vergleich mit *ab initio* FT-RTS Simulationen liefert allerdings eine konsistente Erklärung der experimentellen Daten und macht FT-RTS damit zu einer höchst genauen Methode um die elektronischen Bandlücken sowie die Banddispersion von GNBs auf metallischen Substraten zu bestimmen. Den Abschluss bildet eine theoretische Diskussion der elektronischen Struktur von Graphen „zigzag“ Rändern. Der Vergleich mit aktuellen Experimenten legt nahe, dass die Charakterisierung der *intrinsischen* Eigenschaften von „zigzag“ Rändern ihre Entkopplung vom metallischen Substrat bedingt.

Preface

The work presented in this thesis was performed at the nanotech@surfaces laboratory at Empa Dübendorf. While most of its members are experimental physicists, the laboratory also hosts an embedded group of computational physicists, which I have been lucky to be a part of during the last years. This unusual constellation allows for very direct interaction between those performing experiments and those performing simulations – an opportunity that I have tried to use as much as possible and that has been indispensable for the results obtained in this thesis.

Since this theoretical work is both motivated by and closely intertwined with experiments, experimental results are presented where appropriate, with corresponding attribution. If not indicated otherwise, all simulations and theoretical considerations have been performed by myself.

The manuscript is structured in six main chapters. The introduction illustrates the reasons that make graphene a fascinating material and describes the motivation for studying graphene nanoribbons. It stands out from the rest of the manuscript in that it is aimed at a wider readership of non-specialists, while at the same time explaining important concepts and providing interesting details. The next chapter reviews the theories and computational methods that are relevant to the investigations.

The remaining chapters each address one scientific challenge in the characterization of bottom-up fabricated GNRs. Following a short introduction, they report the work done and the conclusions reached in the specific topic under investigation. These chapters are largely based on the author's contributions to publications, a complete list of which is given at the end of this thesis.

Nomenclature

$\hat{\mathcal{H}}$ Hamiltonian operator

$\rho(\mathbf{r})$ Electron density

m_e Electron mass

m_p Proton mass

7-AGNR $N = 7$ armchair graphene nanoribbon

AFM Atomic force microscopy

AGNR Armchair graphene nanoribbon

ARPES Angle-resolved photoemission

DFT Density functional theory

DOS Density of states

FT-LDOS Fourier-transformed local density of states

GGA Generalized gradient approximation

GNR Graphene nanoribbon.

LDA Local density approximation

LSDA Local spin-density approximation

STM Scanning tunneling microscopy

STS Scanning tunneling spectroscopy

ZGNR Zigzag graphene nanoribbon

CHAPTER 1

Introduction

1.1 The field effect in a semimetal

In late 2002, Andre Geim, professor of physics at the University of Manchester and already famous for levitating a frog using a powerful magnet [1], tasked his new Ph.D. student Da Jiang with one of his exploratory "lateral experiments": trying to make films of graphite "as thin as possible" [2]. The motivation behind this experiment was to investigate whether electrical conduction through the semimetal graphite could be controlled by means of the so-called *field effect*.

The field effect is the central mechanism used for electronic switching in today's information technology. The prototypical electronic switch, the *field effect transistor*, is based on a semiconducting material, which can be switched between its insulating and conducting state through a nearby *gate* electrode. Depending on the polarity of the voltage applied to the gate, the generated electric field either attracts free charge carriers into the semiconducting material or expels them.[1] By modulating the number of free charge carriers, the gate opens and closes a conducting *channel* in the semiconductor, which is directly reflected in its ability to conduct electricity.

Now, what determines whether a given material can be switched via the field effect? One obvious condition is that the number of additional charge carriers provided by the field effect needs to be sufficiently large compared to the number of free charge carriers that naturally occur in the material. Let us therefore shortly recall the order of magnitude of these two quantities.

The gate electrode must be separated from the semiconductor by an insulating dielectric barrier in order to enable the modulation of free charge carriers in the channel without an undesired continuous flow of current between channel and gate. The maximum number of induced charge carriers, per area of the gate electrode, depends on how much pull the insulator can withstand before

[1] While the elementary charge carriers in any semiconductor are the negatively charged electrons, charge transport in the valence band of a semiconductor is more elegantly described in terms of the motion of positively charged *holes*. "Charge carriers" thus refers to electrons, where transport occurs in the conduction band, and to holes, where transport occurs in the valence band.

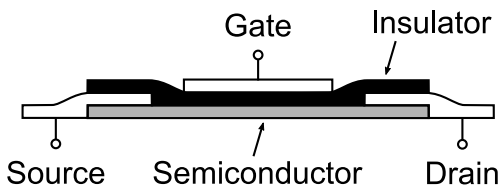

Figure 1.1: Schematic cross section of a (thin film) field effect transistor. Applying voltage to the gate electrode opens and closes a conducting channel in the semiconductor, which in turn switches the current flow between source and drain electrodes.

it breaks down, i.e. on its *dielectric strength*. Conventional dielectrics, such as SiO_2, allow for induced charge densities of around $10^{13}/\mathrm{cm}^2$, while densities approaching $10^{15}/\mathrm{cm}^2$ are nowadays achievable by making use of the electrical double layers formed at the interface with electrolytes or ionic liquids [3]. This number is to be compared against the number of free charge carriers that are present in the semiconductor when no gate voltage is applied.

In metals, the number of free charge carriers is of the order of the number of atoms in the material, i.e. about $10^{23}/\mathrm{cm}^3$. In order to allow for any appreciable field effect, a metal must therefore be made very thin. A metal film of just 1 nm thickness, which is extremely difficult to achieve,[2] already contains of the order of 10^{16} free charge carriers per cm^2. Even under ideal conditions, the field effect can therefore not be expected to modulate the conductivity of a metal by more than a few percent.

A pristine crystalline semiconductor has no free charge carriers at zero temperature.[3] At finite temperature, electrons are thermally excited across the energy band gap, giving rise to a concentration of free charge carriers that strongly depends both on temperature and the band gap itself. In the case of silicon, one finds a free charge carrier concentration of around $10^{10}/\mathrm{cm}^3$ at room temperature [4] and so a huge field effect is expected for silicon even in films of µm thickness and beyond.

Semimetals, such as graphite, are essentially semiconductors with zero or close-to-zero band gap. This yields free charge carrier densities in an intermediate range. For graphite at room temperature, one finds $2 \times 10^{19}/\mathrm{cm}^3$, which corresponds to one free electron and one free hole for every 10^4 carbon atoms [5]. By thinning graphite down to a few nanometers one could therefore expect to observe a substantial field effect that would modulate the conductivity by a factor 2 or more. Until the ground breaking experiments in the group of Andre Geim, however, this had never been accomplished [2].

1.2 Graphene – a material of superlatives

The seminal paper published in 2004 by Konstantin Novoselov, Andre Geim and coworkers reported an ambipolar field effect in graphite films consisting of only one to three atomic layers; the single atomic layer being termed *graphene* [6]. The conductivity of the films could be switched by a factor of about 10 at room temperature and about 100 at 4 K – orders of magnitude larger than what was previously achieved in films of (semi)metals [2].

Besides the large field effect, several other aspects of the work were highly remarkable. First, there was the demonstration that such thin continuous films

[2] Evaporation of such low amounts of metal typically results in separate islands rather than continuous films, since islands tend to minimize the surface energy.

[3] For brevity, the technologically important *doping* of semiconductors with impurities is not discussed here.

could be made with lateral dimensions of several tens of μm. The fact that graphite is a layered material with covalent bonds within the plane and much weaker van-der-Waals interactions between planes enabled a highly unusual method of thin film fabrication: peeling off flakes from thin graphite platelets by adhesive tape until the remaining material contained sufficient area with thickness of just a few nanometers.

Perhaps even more surprising was the reported mobility of charge carriers. When an electric field $\mathcal{E}$ is applied to a material, its mobile charge carriers are accelerated. This acceleration does not continue indefinitely, since charge carriers scatter at impurities or deformations of the lattice caused by thermal vibrations. Instead, the average velocity of charge carriers quickly approaches a *drift* velocity v_D that is, to first approximation, proportional to the applied field. The mobility μ is the corresponding proportionality constant, i.e. higher mobility (less scattering) leads to a higher drift velocity $v_D = \mu\mathcal{E}$.

The mobility is an important figure of merit for channel materials in transistor applications. A field effect transistor tries to modulate the current between source and drain electrodes by modulating the number of mobile charge carriers through the gate voltage. If the charge carriers in the channel are able to move faster, the modulation of the current increases. An increase in charge carrier mobility therefore allows to maintain the same level of current modulation with a smaller gate, thus enabling higher switching speeds.[4]

Novoselov and coworkers reported mobilities of up to $15\,000\,\frac{\mathrm{cm}^2}{\mathrm{Vs}}$ at room temperature – one order of magnitude higher than electron mobility in silicon and less than an order of magnitude below the mobility in highly ordered pyrolytic graphite (HOPG), which had been used as a starting material [6].[5] This came as a great surprise, since the thin films were processed under ambient conditions and device fabrication involved placing the unprotected films on microscopically rough SiO_2 substrates, followed by a lithography step. Still, the charge carriers in the films could move almost unobstructed, suggesting that the films were highly chemically inert and essentially remained single crystals with very few defects.

Graphene was arguably the thinnest material ever made, set the record for the field effect in a semimetal and supported current densities translating to more than $10^8\,\mathrm{A/cm}^2$ [6], orders of magnitude higher than copper. Driven by the exceptional quality of graphene crystals, even more superlatives were to follow: graphene's breaking strength was determined to be an astonishing $40\,\mathrm{N/m}$ and its Young's modulus of $1.0\,\mathrm{TPa}$ is the highest measured for any material [9].[6] A thermal conductivity of $5\,000\,\mathrm{W/(m\,K)}$ at room temperature

[4] A smaller gate results in a smaller gate capacity and the characteristic time scale required to charge a capacity C over a resistance R is given by $\tau = RC \propto C$.

[5] The mobility of HOPG was later matched in experiments on suspended graphene [7] and graphene encapsulated by hexagonal boron-nitride [8], reaching $\mu > 100\,000\,\frac{\mathrm{cm}^2}{\mathrm{Vs}}$ close to room temperature.

[6] Measured using indentation of free-standing graphene with the diamond tip of an atomic

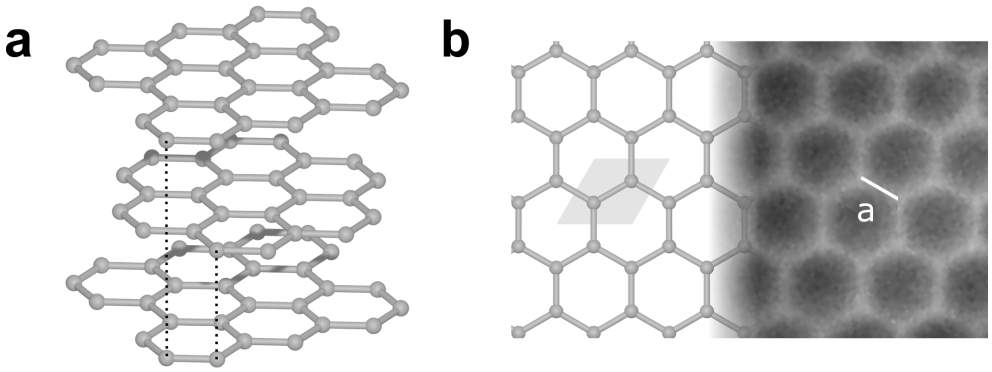

Figure 1.2: Atomic structure of graphite and graphene. (a) Graphite with Bernal (ABA) stacking of layers. (b) Graphene, a honeycomb lattice of carbon atoms. Model and frequency-shift image obtained by non-contact atomic force microscopy (courtesy of Thomas Dienel). Indicated are the unit cell containing two carbon atoms and the carbon-carbon bond length $a \approx 0.142\,\mathrm{nm}$.

was reported – again, higher than for any other material [10]. This astonishing package of properties has led research groups worldwide to start working on graphene and resulted in Geim and Novoselov being awarded the Nobel Prize in Physics in 2010, just six years after the publication of their seminal paper.

1.3 Tuning the gap

Although the high charge carrier mobility in graphene has enabled the fabrication of transistors with switching speeds of 400 GHz[7] [11], it remains to be seen whether graphene will find applications in high-frequency electronics. The lack of a band gap, which was one of the original reasons to investigate graphene, poses an obstacle here since thermal excitation of charge carriers gives rise to a significant base level of conductivity at room temperature – in other words, graphene transistors do not turn off completely. In the domain of high-frequency signal amplification, the high off-currents affect the power gain, causing it to level off at lower switching frequencies than the current gain [12]. In the domain of *digital* electronics, the problem is even more severe, since high integration densities make power dissipation of transistors in the off-state a major concern. The industry standard complementary metal-oxide-semiconductor (CMOS) technology based on silicon offers on/off ratios in the range of $10^4 - 10^7$ [12], compared to on/off ratios of about 10 for graphene transistors.

force microscope.

[7] Cited is the cutoff frequency f_T, at which the small-signal current gain drops to unity.

While this represents a drawback, graphene does offer additional interesting properties for transistor applications, even besides the high carrier mobility. The ultimately low thickness of the graphene channel is beneficial for electrostatics, allowing for further miniaturization of transistors before adverse short-channel effects set in [12]. And since graphene is mechanically flexible and can be processed at room temperature, it enables the fabrication of transistors on flexible plastic foils that outperform transistors based on other organic semiconductors by orders of magnitude [13]. Instead of disregarding graphene for transistor applications, it is therefore worth investigating whether the problem of the missing band gap can be overcome.

One natural idea is to open a band gap by lateral confinement, i.e. by cutting graphene into narrow ribbons. Through selection of the appropriate width, this approach promises the exciting possibility to tune the gap to just the optimal value for the intended application. It turns out that this route is not quite as straightforward as one might think. In order to open a band gap of 0.4 eV or more, as required for room-temperature digital logic applications [12], *ab initio* electronic structure calculations predict that the ribbon width must be below 10 nm [14]. This corresponds to just about 100 carbon atoms across the ribbon and is near impossible to achieve with standard lithographic methods. On top of this, scattering of charge carriers must be avoided if the high mobility of the parent material is to be maintained, meaning that even atomic defects at the edges of these graphene nanoribbons (GNRs) need to be avoided.

Numerous alternatives to lithography have been pursued, such as sonochemical breaking, and metal-catalyzed cutting of graphene, as reviewed in reference [15]. Similar techniques were also applied to carbon nanotubes, which can be produced with very low diameters and can be "unzipped" to obtain graphene nanoribbons [15]. However, none of these top-down approaches provide the desired GNRs with widths below 10 nm and atomically precise edges.

The strategy developed in collaboration between the nanotech@surfaces laboratory at Empa and the department for synthetic chemistry at the Max Planck Institute for Polymer research approaches the problem from a different angle. Since cutting GNRs with atomic precision is clearly challenging, why not try to stitch up GNRs from smaller building blocks? By designing the molecular building blocks, it would be possible to define the width of the GNR down to the single atom, providing ultimate control over the band gap. Furthermore, molecules can be highly purified, allowing for correspondingly low numbers of defects.

Traditional solution-based polymerization chemistry requires reactants and products to be soluble – a problem, when macromolecules containing several hundreds to thousands of atoms are to be synthesized.[8] This is where the

[8]This problem has recently been overcome by using precursors with long alkyl chains [17]. In this approach, however, the GNR edges remain decorated by the flexible alkyl chains,

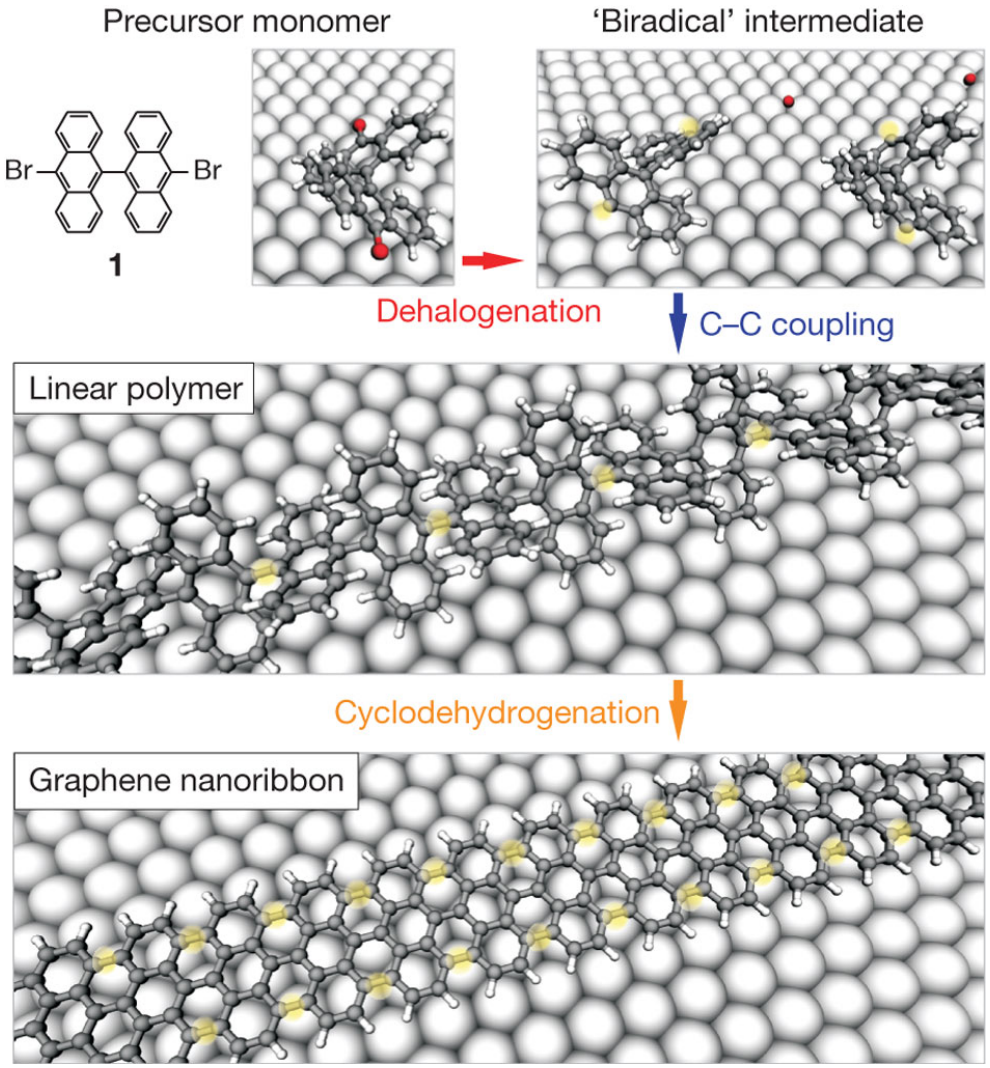

Figure 1.3: Bottom-up strategy for synthesis of atomically precise graphene nanoribbons. Grey, carbon; white, hydrogen; red, halogens; underlying surface atoms shown by large spheres. Figure reproduced with permission from Macmillan Publishers Ltd: reference [16], Copyright (2010).

emerging field of on-surface chemistry has come into play, following pioneering works in the years 2007-2009 that described the surface-supported covalent assembly of networks and conjugated molecular wires [18, 19, 20]. Figure 1.3 illustrates the recipe devised for the bottom-up fabrication of graphene nanoribbons with atomically precise edges and atomically precise width [16]. The precursor is a carefully designed molecule that determines the width of the GNR to be synthesized – here, 10,10'-dibromo-9,9'-bianthryl yields a GNR with armchair edges and a width of seven carbon atoms (7-AGNR). The precursor molecule is evaporated onto the crystalline surface of a noble metal, such as Au(111) or Ag(111), which activates the molecule by removal of its two halogen atoms. Upon heating to a temperature $T_1 \approx 200°\mathrm{C}$, the biradical species become mobile on the surface and start polymerizing into linear chains, where the building blocks are connected by single carbon-carbon bonds. After chain formation is completed, the sample is heated further to $T_2 \approx 400°\mathrm{C}$, inducing a cyclodehydrogenation reaction that transforms the polymers into planar GNRs.

Since the first successful demonstration of this approach in 2010, some of the initial questions have been addressed, such as the size of the band gap of the GNRs[9] [21] or the mechanism behind the cyclodehydrogenation reaction [22]. In this pursuit, computer simulations of the atomic and electronic structure have played a pivotal role by filling in gaps of knowledge that were not accessible experimentally and by helping to interpret and rationalize spectroscopic data. This thesis reports on further steps taken into this direction, addressing questions concerning the termination of the nanoribbons, the dependence of the electronic band gap on GNR length and the determination of their electronic band structure through Fourier-transformed scanning tunneling spectroscopy.

From the computational point of view, the field is both fascinating and very challenging. On the one hand, low-temperature scanning tunneling and atomic force microscopy in ultrahigh vacuum provides such a clear and detailed view into the nanoworld that the complete determination of the atomic structure becomes possible experimentally. In principle, this is all that is needed for an exact prediction of the corresponding electronic structure by *ab initio* methods. But on the other hand, while quantum chemistry provides well-established methods for molecules and theoretical solid state physics provides well-established methods for bulk crystals, the interface between molecules and crystal surfaces remains computationally challenging. Nevertheless, significant progress is being made, be it in the incorporation of dispersion forces into standard density functional theory approximations or algorithmic progress in many-body approaches that allow for the *ab initio* description of dielectric

which may introduce sources of scattering for charge carriers.

[9] A band gap of 2.3 eV was determined for the 7-AGNR on Au(111).

screening.[10]

Concerning the prospect of applications of the bottom-up approach, the precisely controlled conditions involving ultrahigh vacuum and single-crystal surfaces – while forming the basis for accurate scientific investigations – are not suitable for industrial processes. Efforts are underway to relax vacuum conditions [23], to devise methods for transfer to insulating substrates [24] or direct growth on insulators [25] as well as to tune the gap by fabricating atomically precise GNRs with larger widths [26, 27]. Still, a lot of work remains to be done and whether atomically precise graphene nanoribbons will ever make it into the market is unclear at this stage. In the domain of digital electronics, other two-dimensional materials with intrinsic band gaps, such as the transition metal dichalcogenides, may take over if sufficiently high charge carrier mobilities can be realized [12]. However, the new concepts of two-dimensional materials and on-surface synthesis of functional nanomaterials are here to stay. In both of these rapidly evolving fields many directions remain unexplored and promise to provide exciting challenges in both experimental and theoretical research for many years to come.

[10] See chapters 2.2 and 2.3.

CHAPTER 2

Methods

2.1 *Ab initio* electronic structure calculations

The meaning of the attribute *ab initio* in the context of electronic structure calculations is not universally agreed upon. While quantum chemistry tends to reserve the term for wave-function-based approaches with an underlying variational principle, in theoretical solid state physics and computational materials science it is used more broadly to describe an approach that does not rely on empirical parameters. This latter definition is the one referred to here.

All *ab initio* approaches have in common that they are ultimately rooted in the quantum mechanical Schrödinger equation

$$\hat{\mathcal{H}}\,\Psi(\mathbf{r}_1,\ldots,\mathbf{r}_N,\mathbf{R}_1,\ldots,\mathbf{R}_M) = i\hbar\frac{\partial}{\partial t}\,\Psi(\mathbf{r}_1,\ldots,\mathbf{r}_N,\mathbf{R}_1,\ldots,\mathbf{R}_M)\;. \qquad (2.1)$$

The Schrödinger equation describes the time-evolution of a system of N electrons and M nuclei in terms of the wave function Ψ, whose absolute square $|\Psi(\{\mathbf{r}_j\},\{\mathbf{R}_k\},t)|^2$ equals the probability to find the system in the configuration specified by the electronic coordinates $\{\mathbf{r}_j\}$ and nuclear coordinates $\{\mathbf{R}_k\}$ at time t. Further coordinates, such as the spin of electrons or nuclei, are suppressed here for clarity and can be thought of as being included in $\mathbf{r}_j$ and $\mathbf{R}_k$.

The Hamiltonian operator $\hat{\mathcal{H}}$ contains the physical model appropriate for the particular system and the quantities of interest. In this thesis the systems of interest are graphene nanostructures and the quantities of interest are their atomic and π-electronic structure. This information may be used to justify simplifications of the most general form of $\hat{\mathcal{H}}$, three of which are outlined in the following.

First, the graphene nanostructures investigated in this work are made up of light elements. The electrons in these materials move at velocities far below the speed of light, leading to low relativistic mass corrections[1] and weak spin-orbit coupling.[2] It is therefore safe to consider the non-relativistic limit, at least for the valence electrons.

Second, the adiabatic Born-Oppenheimer approximation is employed [30, 31]: Since the masses of electrons and protons are related by $m_p/m_e \approx 1836$, an electron generally moves much faster than a nucleus of mass $M \geq m_p$. To second order in $\kappa = \sqrt[4]{m_e/M}$, the electrons follow the nuclear motion *adiabatically*, i.e. always remaining in their instantaneous ground state [31]. This approximation allows to write the wave function as a product

$$\Psi(\{\mathbf{r}_j\},\{\mathbf{R}_k\},t) = \Psi_{\{\mathbf{R}_k\}}(\{\mathbf{r}_j\},t)\,\chi(\{\mathbf{R}_k\},t)$$

[1] The binding energy of the carbon $2s$ electron is $E_b \approx 18\,\mathrm{eV}$ [28]. Linking the total energy E to the kinetic energy T through the virial theorem $\langle E\rangle = -\langle T\rangle$, one finds that the $2s$ electron moves at $\sqrt{1-(E_b/(m_ec^2)+1)^{-2}} \approx 1\%$ of the speed of light, corresponding to a mass increase of $1/\sqrt{1-E_b/(m_ec^2)} - 1 \approx 0.002\%$.

[2] Spin-orbit coupling in flat graphene is of the order of $1\,\mu\mathrm{eV}$ [29].

of an electronic wave function $\Psi_{\{\mathbf{R}_k\}}$ and a nuclear wave function χ, where the equation for $\Psi_{\{\mathbf{R}_k\}}$ involves only the instantaneous *positions* of the nuclei, not their momenta [31]. In the following, the subscript $\{\mathbf{R}_k\}$ is dropped for convenience.

In graphene, the vanishing electronic gap enables electronic excitations at energies corresponding to nuclear vibrations and the adiabatic approximation has been shown to be problematic [32]. In contrast to graphene, the graphene nanoribbons investigated here do have substantial electronic gaps. Furthermore, the attention in this work is directed mainly towards the electronic structure at zero temperature, and nuclear vibrations are not considered. Still, in materials made up of light elements, such as carbon, even the quantum-mechanical zero-point motion of the nuclei can give rise to an appreciable renormalization of the electronic gap [33]. While this effect can be captured within the adiabatic approximation, it requires the computation of the electron-phonon coupling, which has not been attempted here. For an overview of the recent work in this direction with focus on diamond, see reference [34].

And third, since there are no time-dependent external potentials to be considered here, the Hamiltonian $\hat{\mathcal{H}}$ does not explicitly depend on time. Without loss of generality, the search for solutions to the Schrödinger equation can thus be restricted to stationary states, whose trivial time-dependence can be factored out:

$$\Psi(\{\mathbf{r}_j\}, t) = \exp\left(-iEt/\hbar\right) \Psi(\{\mathbf{r}_j\})$$

One obtains the time-independent Schödinger equation for non-relativistic electrons in the Born-Oppenheimer approximation

$$\hat{\mathcal{H}}\, \Psi(\mathbf{r}_1, \ldots, \mathbf{r}_N) = E\, \Psi(\mathbf{r}_1, \ldots, \mathbf{r}_N) \tag{2.2}$$

where the Hamiltonian is now given explicitly by

$$\hat{\mathcal{H}} = -\sum_j \frac{\hbar^2}{2m_e} \nabla^2_{\mathbf{r}_j} + \frac{1}{2} \sum_{j \neq k} \frac{1}{4\pi\varepsilon_0} \frac{e^2}{|\mathbf{r}_j - \mathbf{r}_k|^2} \tag{2.3}$$

$$- \sum_{jJ} \frac{1}{4\pi\varepsilon_0} \frac{Z_J e}{|\mathbf{r}_j - \mathbf{R}_J|} + \sum_{JK} \frac{1}{4\pi\varepsilon_0} \frac{(Z_J e)(Z_K e)}{|\mathbf{R}_J - \mathbf{R}_K|} \quad . \tag{2.4}$$

It contains the kinetic energy of electrons, the Coulomb repulsion between electrons, the Coulomb attraction between electrons and nuclei as well as the Coulomb repulsion between nuclei. Since the motion of electrons and nuclei has been decoupled, the only term involving more than one spatial coordinate of the wave function is the Coulomb interaction between electrons. The

Hamiltonian can therefore be written as

$$\hat{\mathcal{H}} := \sum_j \hat{h}(\mathbf{r}_j) + \frac{1}{2}\sum_{j\neq k} \frac{1}{4\pi\varepsilon_0}\frac{e^2}{|\mathbf{r}_j - \mathbf{r}_k|^2} \tag{2.5}$$

where $\hat{h}(\mathbf{r}_j)$ is a one-particle operator. In the following, Hartree atomic units will be used, i.e. $\hbar = m_e = e = \frac{1}{4\pi\varepsilon_0} = 1$.

Equation (2.2) is still not solvable analytically, and even numerically exact solutions can not be obtained for most systems of interest. Finding accurate and efficient approximations to this equation is a formidable task that has kept generations of theoretical chemists and physicist busy and continues to do so today. It is often pointed out that the domain of the wave function $\Psi(\{\mathbf{r}_j\})$ grows exponentially with the number of electrons and that therefore the exact Ψ cannot be computed or even stored for systems with many electrons. Luckily, such a detailed knowledge about each particle in the system is seldom required. In order to compute the expectation values of many experimental observables, it is enough to know the *average* behavior of one or two particles.

One highly sought-after quantity is the ground state total energy $E = E_N(\mathbf{R}_k)$ as a function of the positions $\mathbf{R}_k$ of the nuclei and the number of electrons N in the system. From $E_N(\{\mathbf{R}_k\})$ the equilibrium atomic structure may be determined by varying the atomic positions such as to minimize E_N. The cohesive energy of crystals and the atomization energy of molecules may be calculated from the difference of E_N evaluated at the equilibrium crystal structure and E_N for the isolated atoms. Forces on the nuclei are computed as $-\nabla_{\mathbf{R}_l} E_N(\{\mathbf{R}_k\})$, allowing to obtain nuclear vibrations in the adiabatic approximation. And for finite systems, the vertical ionization potential may be calculated as $I_N = E_{N-1} - E_N$.[3] The ground state energy functional is therefore well-suited for lining up different exact theoretical frameworks [35].

In density functional theory (DFT), the variable is the electron density

$$\rho(\mathbf{r}) = N \int \Psi^*(\mathbf{r}, \mathbf{r}_2, \ldots, \mathbf{r}_N)\, \Psi(\mathbf{r}, \mathbf{r}_2, \ldots, \mathbf{r}_N)\, d^3r_2 \ldots d^3r_N \quad ,$$

which describes the probability of finding an electron at a particular point $\mathbf{r}$ in space. Hohenberg and Kohn proved in 1964 that there is a one-to-one correspondence between a system's ground state wave function and its ground state electron density [36]. In particular, the ground state energy of a system can be determined, in principle exactly, from its ground state electron density alone. The fact that ρ depends only on three real numbers $\mathbf{r} = (x, y, z)$ simplifies the computational treatment enormously and is one of the reasons why DFT has evolved to become the workhorse of computational materials science. It is the main method used in this thesis and introduced in more detail in section 2.2. Besides its great success, however, the exact energy functional postulated by Hohenberg and Kohn has remained elusive and finding

[3] Analogously, the electron affinity is obtained as $A_N = E_N - E_{N+1}$.

systematic improvements to existing approximations has been proven to be difficult, despite decades of intensive research. In summary, the simplicity of the variable ρ comes at the price of a very complicated dependence of the total energy functional on ρ.

Reduced density matrix functional theory (RDMFT) is formulated around the one-body reduced density matrix[4]

$$\rho_1(\mathbf{r};\mathbf{r}') = N \int \Psi^*(\mathbf{r}', \mathbf{r}_2, \ldots, \mathbf{r}_N)\, \Psi(\mathbf{r}, \mathbf{r}_2, \ldots, \mathbf{r}_N)\, d^3r_2 \ldots d^3r_N$$

The electron density is recovered as $\rho(\mathbf{r}) = \rho_1(\mathbf{r};\mathbf{r})$ and, in analogy to DFT, there is a one-to-one correspondence between a system's ground state wave function and its ground state reduced density matrix [37]. The knowledge of $\rho_1(\mathbf{r};\mathbf{r}')$, a function of six real numbers, allows to calculate the expectation value of any one-body operator $\hat{\mathcal{O}}(\mathbf{r})$ as

$$\langle\Psi|\hat{\mathcal{O}}|\Psi\rangle = \int \lim_{\mathbf{r}'\to\mathbf{r}} \hat{\mathcal{O}}(\mathbf{r})\rho_1(\mathbf{r};\mathbf{r}')\, d^3r \tag{2.6}$$

The one-body term $\hat{h}(\mathbf{r}_j)$ of the Hamiltonian, which includes the kinetic energy as well as the Coulomb interaction with the nuclei, is therefore obtained in a straight-forward manner. In analogy with equation 2.6, the two-body Coulomb interaction between electrons, however, would require the two-body reduced density matrix $\rho_{12}(\mathbf{r}_1, \mathbf{r}_2; \mathbf{r}_1', \mathbf{r}_2')$ – a function of 12 real numbers.[5]

In summary, by introducing a more complex variable ρ_1, RDMFT goes some way towards simplifying the total energy functional, but the Coulomb term still requires approximation. RDMFT is not used in this thesis.

In many-body perturbation theory (MBPT) the central quantity is the one-particle Green function

$$G(\mathbf{r}, \mathbf{r}', t - t') = (-i)\langle\Psi|\hat{\psi}(\mathbf{r}, t)\hat{\psi}^\dagger(\mathbf{r}', t')|\Psi\rangle \tag{2.7}$$

where $\hat{\psi}^\dagger(\mathbf{r}', t')$ and $\hat{\psi}(\mathbf{r}, t)$ are field operators creating an electron in $\mathbf{r}'$ at time t' and removing an electron from $\mathbf{r}$ at time[6] $t > t'$. $|G(\mathbf{r}, \mathbf{r}', t - t')|^2$ describes the probability for an additional electron to propagate from point $\mathbf{r}'$ to $\mathbf{r}$ in time $t - t'$. From this "dynamical density matrix" the one-body density matrix is recovered as $\rho_1(\mathbf{r}, \mathbf{r}') = (-i)G(\mathbf{r}, \mathbf{r}', 0^-)$. In MBPT the total energy functional does not require approximation. The formula

[4] An intuitive physical interpretation of the 1-RDM is less straight-forward. Note that the probability of finding one electron at $\mathbf{r}$, given that there is another electron at $\mathbf{r}'$, is determined by the pair correlation function $g(\mathbf{r}, \mathbf{r}') = \frac{\rho_{12}(\mathbf{r},\mathbf{r}';\mathbf{r},\mathbf{r}')}{\rho(\mathbf{r})\rho(\mathbf{r}')}$, which involves the 2-RDM ρ_{12}.

[5] Since the Coulomb interaction is a local operator, only $\rho_{12}(\mathbf{r}_1, \mathbf{r}_2; \mathbf{r}_1, \mathbf{r}_2)$ (or, equivalently, $\rho(\mathbf{r}_1)$ and $g(\mathbf{r}_1, \mathbf{r}_2)$) is actually needed. In the minimization of the total energy with respect to ρ_{12}, however, one encounters the problem of N-representability [38].

[6] Details of time-ordering for general t, t' are deferred to section 2.3.

$$E[G] = -i \int \lim_{\mathbf{r}' \to \mathbf{r}} \lim_{t' \downarrow t} \left[i \frac{\partial}{\partial t} + \hat{h}(\mathbf{r}) \right] G(\mathbf{r}, \mathbf{r}', t - t') \, d^3 r \, dt \tag{2.8}$$

given by Galitskii and Migdal in 1958 [39] describes how to compute the exact total energy E from the one-particle Green function. I.e. the ground state energy $E_N(\{\mathbf{R}_k\})$ of a system can be calculated directly from its ground state Green function $G(\mathbf{r}, \mathbf{r}', t - t')$, a function of seven real numbers.

The Green function is clearly much more manageable than the wave function. Nonetheless, it is still complex enough that formula (2.8) and its variants[7] are not routinely used to find the ground state Green function of a system in the same way as, for example, density functionals are used to find the ground state density. While formulas like (2.8) are starting to be applied to obtain total energies of atoms [42] and atomic dimers [43, 44], the Green functions plugged into these equations are determined approximatively. One popular approximative approach is the *GW* approximation, which is introduced in section 2.3. It has been used in this thesis not with the goal of computing total energies, but in its more traditional domain of computing one-particle excitation energies.

At the end of this brief introduction, please note that the methods used in this thesis represent just a small fraction of the vast arsenal of *ab initio* electronic structure theory. For further reading on the post-Hartree-Fock methods of configuration interaction [45], Møller-Plesset perturbation theory [46] and the coupled cluster expansion [47], or the different Quantum Monte Carlo approaches [48] the interested reader is referred to the corresponding references.

[7] Such as the Luttinger-Ward functional [40] and the Klein functional [41].

2.2 Density functional theory

During the last two decades, density functional theory has evolved to become the most frequently used electronic structure method in the study of condensed matter systems. The vast amount of literature relating to DFT is reflected, for example, by the fact that two papers that are typically cited in relation with one particular density functional approximation (B3LYP [49, 50]) already rank among the top ten most cited scientific papers of all time.[8] Great reference works [52] as well as introductory texts [53] are readily available, which is why this section is restricted to the very minimum of the general theory, going into more detail where appropriate for the particular use cases in this thesis.

The seminal paper by Hohenberg and Kohn not only delivered a straightforward proof of the formal equivalence between the ground state density of a system and its ground state wave function. It also proved the existence of a universal total energy functional $E[\rho]$, which – for any given arrangement of nuclei[9] $\{\mathbf{R}_j\}$ and number of electrons N – adopts its global minimum at the ground state density [36].[10] Following Levy [54] and Lieb [55], it may be formally written down as

$$E[\rho] = \min_{\Psi\to\rho}\langle\Psi|\mathcal{H}|\Psi\rangle \tag{2.9}$$

$$= \min_{\Psi\to\rho}\Big[\langle\Psi|\hat{T}|\Psi\rangle + \langle\Psi|U|\Psi\rangle\Big] + \int \rho(\mathbf{r})V_{ext}(\mathbf{r})\,d^3r \tag{2.10}$$

$$\text{where}\quad \hat{T} = -\sum_j \frac{1}{2}\nabla^2_{\mathbf{r}_j}\ , \quad U = \frac{1}{2}\sum_{j\neq k}\frac{1}{|\mathbf{r}_j-\mathbf{r}_k|^2} \tag{2.11}$$

$$\text{and}\quad V_{ext} = -\sum_{jJ}\frac{Z_J}{|\mathbf{r}_j-\mathbf{R}_j|}\quad . \tag{2.12}$$

The minimization goes over all wave functions Ψ that yield the density $\rho(\mathbf{r})$. In equation (2.10) the term describing the interaction between the nuclei has been dropped, since it depends only on the coordinates of the nuclei. The *ground state* density may then be obtained in a second step by minimizing the functional $E[\rho]$ over all possible densities ρ that are compatible with the number of electrons N.[11]

2.2.1 The Kohn-Sham Ansatz

Early approximative energy functionals by Thomas [56], Fermi [57] and Dirac [58] were indeed formulated directly in terms of the density. They failed,

[8] As of 2014, according to Thomson Reuters' Web of Science [51].

[9] Or, in more general terms, for any local external potential $V_{ext}(\mathbf{r})$.

[10] For simplicity, systems with degenerate ground states shall not be considered here.

[11] As indicated in 2.10, the trial densities must be N-representable, i.e. need to result from *some* antisymmetric N-electron wave function Ψ.

however, to describe the shell structure of atoms and the bonding of atoms in molecules [59]. Today, the statement that the variable of DFT is the electron density does not quite correspond to the computational practice.

In order to address the problem of finding adequate approximations for the kinetic energy, Kohn and Sham proposed to construct an auxiliary system of non-interacting electrons whose kinetic energy may be calculated in a straightforward manner [60]. Let's assume that the exact ground state density of a system can be represented not only as resulting from the many-body wave function Ψ, but also from some non-interacting wave function Ψ_0, i.e. from a single Slater determinant of orbitals $\{\varphi_i,\, 1 \leq i \leq N\}$ with density $\rho(\mathbf{r}) = \sum_i |\varphi_i(\mathbf{r})|^2$.[12] If this is the case, the functional (2.10) can be reformulated as

$$E_{KS}[\rho] = \min_{\Psi_0 \to \rho} \left[-\frac{1}{2} \sum_j \int \varphi_j^*(\mathbf{r}) \nabla_{\mathbf{r}}^2 \varphi_j(\mathbf{r})\, d^3r + \langle \Psi_0 | U_{xc} | \Psi_0 \rangle \right] \tag{2.13}$$

$$+ \frac{1}{2} \int \frac{\rho(\mathbf{r})\rho(\mathbf{r}')}{|\mathbf{r} - \mathbf{r}'|}\, d^3r\, d^3r' + \int \rho(\mathbf{r}) V_{ext}(\mathbf{r})\, d^3r \tag{2.14}$$

Here, the *exchange-correlation* energy

$$\underbrace{\langle \Psi_0 | U_{xc} | \Psi_0 \rangle}_{E_{xc}[\Psi_0]} = \langle \Psi | \hat{T} | \Psi \rangle - \underbrace{\langle \Psi_0 | \hat{T} | \Psi_0 \rangle}_{T_s[\Psi_0]} + \langle \Psi | U | \Psi \rangle - \underbrace{\frac{1}{2} \int \frac{\rho(\mathbf{r})\rho(\mathbf{r}')}{|\mathbf{r} - \mathbf{r}'|}\, d^3r'\, d^3r}_{E_H[\rho]}$$

contains the difference between the kinetic energy of the interacting system and of the auxiliary non-interacting system as well as the difference between the quantum mechanical Coulomb energy of the interacting system and its classical counterpart, also known as the *Hartree* energy.[13] It acts as a container for the terms that are not straightforwardly computed and thus need to be approximated.

What has been gained? The functional (2.14) still involves a minimization

$$\min_{\Psi_0 \to \rho} [T_s[\Psi_0] + E_{xc}[\Psi_0]] =: T_s[\rho] + E_{xc}[\rho]$$

with respect to Ψ_0. But if now an approximate formula for $E_{xc}[\rho]$ in terms of

[12] For convenience, the electron spin is not introduced as an explicit variable here and can be considered part of the index i. For spin-unpolarized systems, $\{\varphi_i\}$ contains pairs of identical orbitals.

[13] Separating out the classical electrostatic energy is motivated by its long-ranged nature, hoping that the remainder will be more short-ranged.

ρ is provided, this minimization is achieved by requiring

$$0 = \frac{\delta E_{KS}}{\delta \varphi_i^*(\mathbf{r})} = \frac{\delta T_s}{\delta \varphi_i^*(\mathbf{r})} + \left(\frac{\delta E_{xc}}{\delta \rho(\mathbf{r})} + \frac{\delta E_H}{\delta \rho(\mathbf{r})} + V_{ext}(\mathbf{r}) \right) \frac{\delta \rho(\mathbf{r})}{\delta \varphi_i^*(\mathbf{r})} \tag{2.15}$$

$$= -\frac{1}{2} \nabla_{\mathbf{r}}^2 \varphi_i(\mathbf{r}) + \underbrace{\left(V_{xc}(\mathbf{r}) + \int \frac{\rho(\mathbf{r}')}{|\mathbf{r} - \mathbf{r}'|} \, d^3 r' + V_{ext}(\mathbf{r}) \right)}_{V_{KS}(\mathbf{r})} \varphi_i(\mathbf{r}) \tag{2.16}$$

for all i under the constraint $\langle \varphi_i | \varphi_j \rangle = \delta_{ij}$.

These *Kohn-Sham equations* have the form of a Schrödinger equation for independent particles in a potential $V_{KS}(\mathbf{r})$. In a finite basis, their solution is achieved by diagonalizing the corresponding Kohn-Sham matrix. Complications arise from the fact that the exchange-correlation and Hartree potentials depend on the orbitals $\{\varphi_i\}$ through the density ρ. This is addressed by adopting an iterative procedure:

1. Start with initial guess for $\rho(\mathbf{r})$
2. Calculate Kohn-Sham potential $V_{KS}(\mathbf{r})$
3. Solve Kohn-Sham equations (2.16)
4. Calculate new density $\rho(\mathbf{r}) = \sum_i |\varphi_i(\mathbf{r})|^2$
5. If new density deviates significantly from the previous one, return to 2. Otherwise stop.

At the end of this procedure, the set of orbitals $\{\varphi_i\}$ and the Kohn-Sham potential $V_{KS}(\mathbf{r})$ are consistent and the energy $E_{KS}[\rho]$ corresponds to the ground state energy of the interacting system.

2.2.2 Approximations to the exchange-correlation functional

Decades of intensive research efforts to find and improve approximations of the exchange-correlation functional $E_{xc}[\rho]$ have produced a zoo of functionals that is difficult to keep track of. In the physics community, functional approximations have been derived starting from the homogeneous electron gas.

A homogeneous gas of electrons is defined exclusively by its density $\rho(\mathbf{r}) \equiv N/V =: 1/(\frac{4\pi}{3} r_s^3)$, where V is the volume of the simulation cell and r_s the Wigner-Seitz radius of the sphere occupied by each electron. The corresponding exchange-correlation functional is therefore a *function* of r_s, which has been fitted to results from numerical Quantum Monte Carlo calculations as [61, 62]

$$\varepsilon_{xc}(r_s) \approx \begin{cases} -0.4582/r_s - 0.1423/(1 + 1.0529\sqrt{r_s} + 0.3334 r_s) & r_s \geq 1 \\ -0.4582/r_s - 0.0480 + 0.0311 \ln r_s - 0.0116 r_s + 0.0020 r_s \ln r_s & r_s \leq 1 \end{cases}$$

A straight-forward extension to non-homogeneous systems is achieved by the local-density approximation (LDA)

$$E_{xc}[\rho] = \int V_{xc}(\rho(\mathbf{r}))\rho(\mathbf{r})\, d^3r \tag{2.17}$$

$$\text{where} \quad V_{xc}(\rho(\mathbf{r})) = \left.\frac{d\varepsilon_{xc}(r_s)}{d\rho}\right|_{r_s=r_s(\rho(\mathbf{r}))} \tag{2.18}$$

$$= \varepsilon_{xc}(r_s) - \left.\frac{r_s}{3}\frac{d\varepsilon_{xc}(r_s)}{dr_s}\right|_{r_s=r_s(\rho(\mathbf{r}))} \tag{2.19}$$

and $r_s(\rho(\mathbf{r})) = 1/\sqrt[3]{\frac{4\pi}{3}\rho(\mathbf{r})}$. Here, the exchange-correlation potential at position $\mathbf{r}$ depends only on the *local* value $\rho(\mathbf{r})$ of the electron density and assumes the same value as for the homogeneous electron gas with density $\rho(\mathbf{r})$. The approximation becomes exact in the limit of slowly varying densities[14] as well as in the high-density limit[15] [60]. In spin-polarized systems, where the orbitals of spin-up and spin-down electrons differ, the functional is generalized to the local spin-density approximation (LSDA) $\varepsilon_{xc}(\rho_\uparrow(\mathbf{r}), \rho_\downarrow(\mathbf{r}))$ with spin-densities $\rho_\uparrow(\mathbf{r}), \rho_\downarrow(\mathbf{r})$. For spin-unpolarized systems with $\rho_\uparrow(\mathbf{r}) = \rho_\downarrow(\mathbf{r}) = \frac{1}{2}\rho(\mathbf{r})$, the LDA is recovered.

In order to go beyond the LDA for inhomogeneous systems, the next logical step is to also include information about the magnitude of the local *gradient* $|\nabla_\mathbf{r}\rho(\mathbf{r})|$ of the density, often referred to as a *semi-local* approximation. Unfortunately, low-order expansions of the exchange-correlation energy in terms of the gradient do not lead to consistent improvements over the LDA, since gradients in real materials are too large [53]. This has led to the introduction of *generalized* gradient approximations with significant freedom in the functional form. Even for the PBE functional, entitled "Generalized Gradient Approximation Made Simple" [63], the analytical expression in terms of the Wigner-Seitz radius and the density gradient is still significantly more complex than for the LDA. It is therefore not reproduced here.

The LDA and PBE approximations are highly successful in describing structural and vibrational properties of dense matter and covalently bound molecules and belong to the standard repertoire of exchange-correlation functionals in solid state physics. Nevertheless, their (semi-)local nature also leads to some unavoidable problems, two of which are briefly discussed in the following.

One problem is related to exchange: the Hartree energy $E_H[\rho]$ describes the classical electrostatic energy of the charge density and thus includes a spurious interaction of each electron with itself. In Hartree-Fock theory, this self-interaction is canceled exactly by Fock's non-local exchange operator. The

[14] Slowly varying in comparison to electronic length scales, such as r_s or the Fermi wave length.

[15] Characterized by $r_s \ll a_0$.

(semi-)local approximations to exchange, however, fail to accomplish this for many systems of interest.This self-repulsion of electrons leads to a tendency of the LDA to over-delocalize electrons, giving rise to an overestimation of bond strengths and a corresponding underestimation of bond lengths.

Since the orbitals $\{\varphi_j\}$ of the non-interacting system of electrons are anyhow available in Kohn-Sham DFT, it seems logical[16] to use this information in order to construct an "exact" exchange energy

$$E_x[\Psi_0] = -\frac{1}{2}\sum_{ij}\delta_{\sigma_i\sigma_j}\int\frac{\varphi_i^*(\mathbf{r})\varphi_j^*(\mathbf{r'})\varphi_j(\mathbf{r})\varphi_i(\mathbf{r'})}{|\mathbf{r}-\mathbf{r'}|}\,d^3r\,d^3r' \tag{2.20}$$

The mixing of exact exchange and (semi-)local correlation, however, is delicate and functionals in this category typically rely on a *hybrid* between exact exchange and (semi-)local approximations to exchange [64, 49].[17] While the incorporation of exact exchange allows to significantly improve atomization energies [65], the corresponding Kohn-Sham equations $0 = \frac{\delta E_{KS}}{\delta\varphi_i^*(\mathbf{r})}$ contain a nonlocal exchange-correlation operator $\hat{V}_{xc}$. In analogy with the Hartree-Fock method, each step of the self-consistent procedure now requires the evaluation of exchange-integrals for all *pairs* of occupied orbitals, making hybrid functionals significantly more computationally demanding than (semi-)local approximations.

Another problem is related to correlation. Dispersion forces arise from fluctuations in the dipole moments of molecules that occur on the time scale of orbital frequencies and again induce dipole fluctuations in neighboring molecules. These forces can easily dominate the interaction between molecules and surfaces, in particular when no covalent chemical bonds are formed. (Semi-)local approximations to correlation are unable to capture these highly non-local effects, since they lead to an exponential decay of the interaction for large atomic separations by construction [66]. They need to be corrected for a practically useful description of molecular adsorption.

One class of dispersion corrections, often summarized under the name "DFT-D" [67], is formulated in terms of an interatomic potential

$$E_c^{disp} = -\sum_{\langle J,K\rangle}\sum_{n=6,8,\ldots} s_n\frac{C_n^{JK}}{(R_{JK})^n}f_{damp}(R_{JK}) \tag{2.21}$$

where the first sum runs over all pairs of atoms, $R_{JK} = |\mathbf{R}_K - \mathbf{R}_J|$ and C_n^{JK} is the isotropic nth-order dispersion coefficient, depending only on the atomic *kinds* of atoms J and K. The dispersion energy E_c^{disp} is simply added to the total energy, thus ensuring the correct asymptotic form of the dispersion

[16] And was proposed by Kohn and Sham already in their original work [60].

[17] The B3LYP functional mentioned in the beginning of this section is such a *hybrid* functional.

interaction $\propto 1/(R_{JK})^6$. In order to avoid double-counting of correlation, the correction needs to be damped at short distances, where the scaling factors s_n and the form of the damping function $f_{damp}(R_{JK})$ are used to adapt to particular (semi-)local exchange-correlation functionals. Extensions of the scheme (2.21) include the treatment of three-body interactions [68] as well as the effects of the hybridization state on the dispersion coefficients, based on fractional occupation numbers [68] or atomic volumes [69].

Since dispersion coefficients for many elements are readily available,[18] this conceptually simple and computationally cheap way of adding dispersion forces to various (semi-)local exchange-correlation functionals has found widespread adoption. The dispersion coefficients are determined either computationally or experimentally on one or several reference systems. These reference systems have traditionally been chosen to be either the bare elements or small molecules containing the elements in question [68], which is suitable for applications in molecules, but provides an electronic environment that can be very different from bulk materials. For the particular application of molecules on coinage metal surfaces, a scheme has been proposed to include screening and polarization effects at the level of atomic pairwise interactions [70]. A rather worrying finding is that molecular binding energies in many cases seem to depend more sensitively on the empirical parametrization of the damping function than on the physically sound dispersion coefficients [71].

Another approach that has gained popularity in recent years is a density-based treatment of the non-local correlation energy, which takes the form

$$E_c^{nl}[\rho] = \int \rho(\mathbf{r})\phi[\rho](\mathbf{r},\mathbf{r}')\rho(\mathbf{r}')\, d^3r\, d^3r' \tag{2.22}$$

The kernel ϕ is derived from first principles using a plasmon pole approximation to the local dielectric function and is a function of $|\mathbf{r}-\mathbf{r}'|$, the electron density n and its gradient at positions $\mathbf{r}, \mathbf{r}'$ [72, 73]. Treated self-consistently, the variational derivative $V_c^{nl}(\mathbf{r}) = \frac{\delta E_c^{nl}}{\delta\rho(\mathbf{r})}$ modifies the exchange-correlation potential $V_{xc} = V_{xc} + V_c^{nl}$ and thus acts directly on the Kohn-Sham wave orbitals. One significant advantage over DFT-D methods is therefore that the effect of the electronic environment, including the possibility of charge-transfer, is captured in a general and physically sound manner [67]. In contrast to the DFT-D methods, the non-local correlation term is not damped at short distances, thus handing the task of avoiding double-counting of correlation over to the exchange-correlation functional. Besides existing functionals, such as PW86 [73], some have thus been designed specifically for this purpose [74]. Regarding computational cost, linear scaling algorithms are available [75] that render the overhead of these so-called "van der Waals density functionals" negligible in standard semi-local calculations.

[18] For the first 94 elements in the case of DFT-D3 [68].

2.3 Many-body perturbation theory in the *GW* approximation

The following short review is largely based on references [76] and [77].

2.3.1 The one-particle Green function

The central object in the many-body theory of one-particle excitations[19] is the time-ordered one-particle Green function. Following the notation by Hedin [78], it is defined as

$$G(1,2) = (-i)\langle\, \hat{\mathcal{T}}[\hat{\psi}(1)\hat{\psi}^\dagger(2)]\,\rangle \tag{2.23}$$

where 1 and 2 each stand for the spatial, spin and time coordinates of a particle: $(1) = (\mathbf{r}_1, \sigma_1, t_1) = (\mathbf{x}_1, t_1)$. $\hat{\psi}^\dagger(2)$ and $\hat{\psi}(1)$ are field operators creating an electron with spin σ_2 in $\mathbf{r}_2$ at time t_2 and removing an electron with spin σ_1 in $\mathbf{r}_1$ at time t_1. The operator $\mathcal{T}$ orders the products of field operators in such a way that time decreases from left to right:

$$\mathcal{T}\left[\hat{\psi}(1)\hat{\psi}^\dagger(2)\right] = \begin{cases} \hat{\psi}(1)\hat{\psi}^\dagger(2), & t_1 > t_2 \\ -\hat{\psi}^\dagger(2)\hat{\psi}(1), & t_1 < t_2 \end{cases} \tag{2.24}$$

Finally, the brackets $\langle\cdot\rangle$ denote the expectation value in the exact many-body ground state.

The Schrödinger equation (2.1) with Hamiltonian (2.4) yields the following equation of motion for the annihilation field operator

$$\begin{aligned} i\frac{\partial}{\partial t_1}\hat{\psi}(\mathbf{r}_1,\sigma_1,t_1) &= \left[\hat{\psi}(\mathbf{r}_1,\sigma_1,t_1), \hat{\mathcal{H}}\right] \\ &= \left(\hat{h}(\mathbf{r}_1) + \sum_{\sigma_2}\int \frac{1}{|\mathbf{r}_1-\mathbf{r}_2|}\hat{\psi}^\dagger(\mathbf{r}_2,\sigma_2,t_1)\hat{\psi}(\mathbf{r}_2,\sigma_2,t_1)\,d^3r_2\right)\hat{\psi}(\mathbf{r}_1,\sigma_1,t_1) \\ &= \left(\hat{h}(\mathbf{r}_1) + \int v(1,2)\hat{\psi}^\dagger(2)\hat{\psi}(2)\,d2\right)\hat{\psi}(1) \end{aligned}$$

where $\int d2 = \int d^3r_2 \sum_{\sigma_2}\int dt_2$ and $v(1,2) = \frac{1}{|\mathbf{r}_1-\mathbf{r}_2|}\delta(t_1-t_2)$ is the Coulomb interaction. Using

$$\left(\frac{\partial}{\partial t_1}\hat{\mathcal{T}}\right)\hat{\psi}(1)\hat{\psi}^\dagger(2) = \delta(\mathbf{r}_1-\mathbf{r}_2)\delta_{\sigma_1\sigma_2}\delta(t_1-t_2) = \delta(1,2) \tag{2.25}$$

the time derivative of the Green function is obtained as

$$i\frac{\partial}{\partial t_1}G(1,2) = \delta(1,2) + \hat{h}(\mathbf{r}_1)G(1,2) \tag{2.26}$$

$$+ \int v(1,3)\langle\, \hat{\mathcal{T}}[\hat{\psi}^\dagger(3^+)\hat{\psi}(3)\hat{\psi}(1)\hat{\psi}^\dagger(2)]\,\rangle\, d3 \tag{2.27}$$

[19] Meaning *charged* excitations that involve the addition or removal of an electron.

Equation (2.27) is the first of a set of integro-differential equations that relate the N-particle Green function to the (N+1)-particle Green function – here, the one-particle Green function is related to the two-particle Green function

$$G(1,2,3,4) = (-i)^2 \langle \hat{\mathcal{T}}[\hat{\psi}(1)\hat{\psi}(2)\hat{\psi}^\dagger(3)\hat{\psi}^\dagger(4)]\rangle \tag{2.28}$$

In practice, however, the two-particle Green function is not known and needs to be approximated. For this purpose, equation (2.27) is rewritten as

$$\left[i\frac{\partial}{\partial t_1} - \hat{h}(\mathbf{r}_1)\right] G(1,2) - \int \Sigma(1,3)G(3,2)\, d3 = \delta(1,2) \tag{2.29}$$

where the non-local, non-hermitian *self-energy* operator Σ has been introduced as a placeholder.

Due to the long-range nature of the classical electrostatic interaction, it is common practice to move the Hartree potential

$$V_H(1) = (-i)\int v(1,2)G(2,2^+)\, d2 = \int \frac{\rho(\mathbf{r}_2)}{|\mathbf{r}_1 - \mathbf{r}_2|} d^3r_2 \tag{2.30}$$

from the self-energy operator into the one-body Hamiltonian via

$$\Sigma(1,3) \to \Sigma(1,3) - \delta(1,3)V_H(1) \tag{2.31}$$

$$\hat{h}(1) \to \hat{h}(1) + V_H(1) \tag{2.32}$$

in the hope that the resulting self-energy may be more short-ranged.

The self-energy $\Sigma(1,2)$ can be regarded as a non-local, non-hermitian analogue of the exchange-correlation potential $V_{xc}(1)$ in density functional theory. But while DFT exchange-correlation functionals tend to be geared[20] towards specific physical systems, such as the homogeneous electron gas or molecular test sets, in section 2.3.3 the self-energy will be approximated by a general perturbation expansion in the screened interaction.

The equation of motion (2.29) can be formally integrated by introducing the *non-interacting* Green function $G_0(1,2)$ as the solution to

$$\left[i\frac{\partial}{\partial t_1} - \hat{h}(\mathbf{r}_1)\right] G_0(1,2) = \delta(1,2) \tag{2.33}$$

This is the common mathematical definition of the Green function corresponding to the linear differential operator $\hat{\mathcal{L}}(1) = \left[i\frac{\partial}{\partial t_1} - \hat{h}(\mathbf{r}_1)\right]$. As will be shown in section 2.3.2, G_0 can readily be obtained by solving the non-interacting problem. By regarding the equation of motion (2.29) as an inhomogeneous differential equation for G, it can now be integrated to obtain the Dyson equation

$$G(1,2) = \int G_0(1,4)\left[\delta(4,2) + \int \Sigma(4,3)G(3,2)\, d3\right] d4 \tag{2.34}$$

$$= G_0(1,2) + \iint G_0(1,4)\Sigma(4,3)G(3,2)\, d3\, d4 \tag{2.35}$$

[20] At least to some degree.

2.3.2 Lehmann representation

One-particle excitations involve the addition or removal of an electron. Starting from the N-electron ground state $|\Psi_0^N\rangle$, they leave the system in a, possibly excited, $(N \pm 1)$-electron state $|\Psi_{j\sigma}^{N\pm1}\rangle$. Following reference [77], one defines the excitation energies[21]

$$\epsilon_j^{N+1} = E_j^{N+1} - E_0^N, \quad \epsilon_j^{N-1} = E_0^N - E_j^{N-1} \tag{2.36}$$

and the corresponding electron addition and removal amplitudes

$$\psi_j^{N+1}(\mathbf{r}_1, t_1) = \langle \Psi_j^{N+1} | \hat{\psi}^\dagger(1) | \Psi_0^N \rangle = e^{-i(E_j^{N+1} - E_0^N)t_1} \langle \Psi_j^{N+1} | \hat{\psi}^\dagger(\mathbf{x}_1) | \Psi_0^N \rangle \tag{2.37}$$

$$\psi_j^{N-1}(\mathbf{r}_1, t_1) = \langle \Psi_j^{N-1} | \hat{\psi}(1) | \Psi_0^N \rangle = e^{-i(E_0^N - E_j^{N-1})t_1} \langle \Psi_0^N | \hat{\psi}(\mathbf{x}_1) | \Psi_j^{N-1} \rangle \tag{2.38}$$

In the last step, the field operators were moved from the Heisenberg picture to the Schrödinger picture using

$$\hat{O}_H(t) = e^{i\hat{\mathcal{H}}t}\, \hat{O}_S\, e^{-i\hat{\mathcal{H}}t} \quad . \tag{2.39}$$

Introducing the closure relations $\sum_j |\Psi_j^{N\pm1}\rangle\langle\Psi_j^{N\pm1}| = 1$ into the definition of the time-ordered one-particle Green function (2.23) yields

$$\begin{aligned} G(1,2) = & -i \sum_j \psi_j^{N+1}(\mathbf{r}_1) \psi_j^{N+1^*}(\mathbf{r}_2) e^{-i\epsilon_j^{N+1}(t_1 - t_2)} \theta(t_1 - t_2) \\ & + i \sum_j \psi_j^{N-1}(\mathbf{r}_1) \psi_j^{N-1^*}(\mathbf{r}_2) e^{-i\epsilon_j^{N-1}(t_1 - t_2)} \theta(t_2 - t_1) \end{aligned} \tag{2.40}$$

where $\theta(t)$ denotes the Heaviside step function

$$\theta(t) = \begin{cases} -1 & t < 0 \\ \frac{1}{2} & t = 0 \\ 1 & t > 0 \end{cases} \quad . \tag{2.41}$$

As made explicit by equation (2.40), the Green function corresponding to a time-independent Hamiltonian $\hat{\mathcal{H}}$ only depends on the time *difference* $t_1 - t_2$. Using the Fourier transform of $\theta(t)$,

$$\theta(\omega) = \frac{1}{2\pi} \int_{-\infty}^{\infty} \theta(t) e^{i\omega\tau - \delta|t|}\, dt = \frac{1}{2\pi} \frac{i}{\omega + i\delta} \quad , \tag{2.42}$$

one obtains the Fourier transform of G in the Lehmann representation

$$G(\mathbf{x}_1, \mathbf{x}_2, \omega) = \sum_j \frac{\psi_j^{N+1}(\mathbf{r}_1) \psi_j^{N+1^*}(\mathbf{r}_2)}{\omega - \epsilon_j^{N+1} + i\delta} + \sum_j \frac{\psi_j^{N-1}(\mathbf{r}_1) \psi_j^{N-1^*}(\mathbf{r}_2)}{\omega - \epsilon_j^{N-1} - i\delta} \tag{2.43}$$

[21] Which are, for simplicity, assumed to be independent of the spin of the electron involved in the excitation. For spin-polarized systems, replace the index j by $j\sigma$.

For a non-interacting (or mean-field) Hamiltonian with a set of orbitals and eigenenergies $\{(\varphi_j, \varepsilon_j)\}$, the electron addition amplitudes ψ_j^{N+1} simply correspond to the empty orbitals and the electron removal amplitudes ψ_j^{N-1} to the occupied orbitals, while the excitation energies $\epsilon_j^{N\pm1}$ are the corresponding orbital energies. Given the full set $\{(\varphi_j, \varepsilon_j)\}$, formula (2.43) thus allows to calculate the corresponding Green function G_0.

2.3.3 The GW approximation

A key concept in many-body perturbation theory is to develop perturbation expansions in terms of the interaction between particles. If the interaction is weak, the expansions may be truncated after some order. If the interaction is strong, progress can still be made by summing certain classes of terms to infinite order in the interaction.

When the self-energy is expanded in terms of the Coulomb interaction v, the convergence rate deteriorates with increasing polarizability of the system and the expansion diverges for metals [78]. In this sense, the Coulomb interaction between electrons is a strong interaction.

In a polarizable medium, however, test charges are screened by the surrounding electrons. It therefore makes sense to move from the picture of electrons interacting via the Coulomb interaction to the picture of *quasiparticles* interacting via the *screened* interaction

$$W(1,2) = \int v(1,3)\varepsilon^{-1}(3,2)\, d3 \tag{2.44}$$

$$= \int \frac{\varepsilon^{-1}(\mathbf{r}_3, \mathbf{r}_2, t_1 - t_2)}{|\mathbf{r}_1 - \mathbf{r}_3|} d^3 r_3 \tag{2.45}$$

where ε^{-1} is the time-ordered inverse dielectric function.

In 1965, Hedin developed the following perturbative series of the self energy in terms of the screened interaction [78]

$$\Sigma(1,2) = iG(1,2)W(1^+,2) - \iint G(1,3)G(3,4)G(4,2)W(1,4)W(3,2)\, d3\, d4 + O(W^3) \tag{2.46}$$

When screening is sufficiently strong, meaning the screened interaction W is sufficiently weak, the expansion may be truncated after the first term, yielding

$$\Sigma(1,2) \approx iG(1,2)W(1^+,2) \tag{2.47}$$

or $\Sigma \approx iGW$ for short, which gives the approximation its name.

One may note here that if Σ would instead be expanded in terms of the Coulomb interaction v, the first term of the expansion is $\Sigma = iGv$ and yields the Hartree-Fock approximation. In some sense, the GW approximation is therefore nothing but the Hartree-Fock approximation for quasiparticles. While

the validity of the GW approximation deteriorates with increasing interaction between quasiparticles, it has been demonstrated that it yields significant improvement over Hartree-Fock even in the case of isolated atoms [42], where screening is comparatively weak.

After plugging the approximation (2.47) into the equation of motion (2.29), one is still left with two unknowns: G and W. These may, however, be determined by iteration until self-consistency.

Starting with an initial guess for the Green function G, the screened interaction W is obtained via the polarization function[22] P:

$$P(1,2) = (-i)G(1,2)G(2,1) \tag{2.48}$$

$$\varepsilon(1,2) = \delta(1,2) - \int v(1,3)P(3,2)\,d3 \tag{2.49}$$

$$W(1,2) = \int v(1,3)\varepsilon^{-1}(3,2)\,d3 \tag{2.50}$$

This allows to calculate a first guess for the self-energy

$$\Sigma(1,2) = iG(1,2)W(1^+,2) \tag{2.51}$$

which in turn provides a new guess for G by evaluating the right-hand side of the Dyson equation

$$G(1,2) = G_0(1,2) + \iint G_0(1,4)\Sigma(4,3)G(3,2)\,d3\,d4 \tag{2.52}$$

The five equations (2.48–2.52) may then be integrated until convergence in G is reached.

2.3.4 Numerical approach

In practice, the most common application of the GW approximation lies in the calculation of the quasiparticle excitation energies ϵ_j or, in periodic systems, the quasiparticle band structure. Even within the GW approximation, however, the required self-consistent solution of equations (2.48–2.52) is quite challenging and has gained momentum only rather recently.[23] This thesis relies on the less computationally intensive, non-selfconsistent G_0W_0 approach,[24] which stops the iterative procedure directly after the first evaluation of the self-energy. It is briefly outlined in the following.

The starting point is given by a set of orbitals and eigenenergies $\{(\varphi_j, \varepsilon_j)\}$ from a mean-field description of the system, typically DFT or Hartree-Fock. The following discussion is restricted to the case of DFT, which corresponds

[22] Also denoted as *irreducible polarizability*. Equation (2.48) holds only in the GW approximation and is also known as *random phase approximation* for P.

[23] See reference [79] for a review.

[24] Due to the large size of the GNRs under study, ranging up to more than 100 atoms.

to starting with $\Sigma_0(1,2) = V_{xc}(\mathbf{r}_1)\delta(1,2)$. The natural first guess for G is then obtained by the corresponding Lehmann representation for G_0.[25]

By plugging the Lehmann representation (2.43) into equation (2.48), the polarization function is obtained directly as [77]

$$P(\mathbf{x}_1, \mathbf{x}_2, \omega) = \sum_j^{'} \sum_k^{''} \varphi_j(\mathbf{r}_1)\varphi_k^*(\mathbf{r}_1)\varphi_j(\mathbf{r}_2)^*\varphi_k(\mathbf{r}_2) \times \left(\frac{1}{\omega + \varepsilon_j - \varepsilon_k + i\delta} - \frac{1}{\omega - \varepsilon_j + \varepsilon_k - i\delta} \right) \tag{2.53}$$

where $\sum'$ sums over occupied states and $\sum''$ over empty states. The sum is evaluated in some finite basis set, for example, plane waves with a given cutoff for the kinetic energy.

Using linear algebra operations (matrix multiplication, inversion), the dielectric function is first determined through equation (2.49), then inverted and finally plugged into (2.50) in order to obtain the screened interaction W. Since W has been obtained directly from G_0, it is labeled W_0 in the following.

At this point, the G_0W_0 self-energy in the frequency domain could be evaluated as

$$\Sigma(\mathbf{x}_1, \mathbf{x}_2, \omega) = \frac{i}{2\pi} \int_{-\infty}^{\infty} G_0(\mathbf{x}_1, \mathbf{x}_2, \omega + \omega')W_0(\mathbf{x}_1, \mathbf{x}_2, \omega')e^{i\omega'\delta}\, d\omega' \tag{2.54}$$

In practice, the peaked structure of G_0 and W_0 on the real frequency axis makes it advantageous to deform the integration contour onto the imaginary axis [80], where the analytic continuations of G_0 and W_0 are smoother.

But even after contour deformation, W_0 needs to be evaluated on a suitable grid of (imaginary) frequencies. Unfortunately, the calculation of P is made expensive by a very slow convergence of the sum (2.53) as a function of the number of empty states[26] that are included. Since Σ is obtained from an integration over all frequencies, the fine details of its dependence on ω are often not important. This has lead to the development of *plasmon pole* models for the frequency dependence of P that allow for an analytic integration over the frequency domain and require the numerical evaluation of P only for one [81] or two [82] frequencies.

In order to evaluate the quasiparticle excitation energies ϵ_j, the expectation value of Σ would have to be computed with respect to the quasiparticle wave functions ψ_j. Yet, it has been found both for a set of small molecules [83] and for bulk *sp* semiconductors and metals [81] that $\psi_j(\mathbf{r}) \approx \varphi_j(\mathbf{r})$. This

[25] Note that this makes G_0 the Green function of the mean-field Hamiltonian, not of $\hat{h}(\mathbf{r}_1)$. This inconsistency is justified by the dramatic improvement of the corresponding orbitals and electron densities, when compared with the Hartree approximation $\Sigma = 0$ [79].

[26] Which is, in principle, limited only by the finite size of the basis set.

approximation is adopted in the G_0W_0 approach. To first order in $\Sigma - V_{xc}$, the excitation energies are therefore given by

$$\epsilon_j = \varepsilon_j + \langle\varphi_j|\Sigma(\epsilon_j) - V_{xc}|\varphi_j\rangle \tag{2.55}$$

An iterative solution of this equation for ϵ_j would require the evaluation of Σ for several frequencies. This is avoided by locally linearizing $\Sigma(\omega) \approx \Sigma(\varepsilon_j) + \partial_\omega\Sigma(\varepsilon_j)(\omega-\varepsilon_j)$, where $\partial_\omega\Sigma(\varepsilon_j)$ is obtained by evaluating Σ at a second, nearby frequency. Equation (2.55) is then solved directly as

$$\epsilon_j \approx \varepsilon_j + Z_j\langle\varphi_j|\Sigma(\varepsilon_j) - V_{xc}|\varphi_j\rangle \quad , \tag{2.56}$$

$$\text{where} \quad Z_j = 1/\left(1 - \langle\varphi_j|\partial_\omega\Sigma(\varepsilon_j)|\varphi_j\rangle\right) \approx \int |\psi_i(\mathbf{r})|^2\, d^3r < 1 \tag{2.57}$$

is an approximation of the quasiparticle weight [77].

2.4 Empirical models

The fact that *ab initio* methods try to incorporate all intricacies of the quantum mechanical Schrödinger equation, can make these calculations computationally expensive and the results difficult to interpret. In this respect, empirical models can help by providing an intuitive picture that allows to rationalize the findings in terms of model parameters as well as to perform extrapolations to similar systems in a computationally efficient manner.

Unlike the *ab initio* approaches that usually aim for the highest generality possible, empirical models may be closely adapted to the particular systems under study – here, graphene nanoribbons.

2.4.1 Clar's theory of the aromatic sextet

Clar's theory of the aromatic sextet provides a simple formalism to predict the distribution of π-electrons in polycyclic aromatic hydrocarbons (PAHs) [84]. It is based on the insight that π-electrons in PAHs tend to *delocalize*. The π-electron distribution in PAHs is therefore not properly represented by one particular Kekulé structure consisting of single and double bonds. A more appropriate representation is provided by the superposition or *resonance* of *all* possible Kekulé structures.

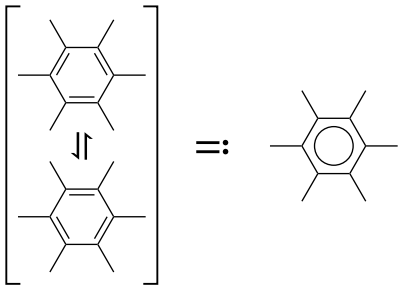

Figure 2.1: The Clar sextet, representing the superposition of two complementary Kekulé structures.

The Clar sextet shown in Figure 2.1 provides an intuitive visual representation of the delocalized nature of the six π-electrons in an aromatic cycle – two possible configurations of single and double bonds are replaced by one ring. This notation allows to cover the different possible Kekulé structures of a given molecule with significantly less effort, simply because a structure containing n Clar sextets represents 2^n Kekulé structures. It also introduces a natural hierarchy: the more Clar sextets a structure contains, the more Kekulé structures it represents and thus the higher its weight in the superposition.

The structure with the maximum number of Clar sextets is termed the *Clar formula*. It is shown in Figure 2.2 for three different cases. Triphenylene has a unique Clar formula containing three Clar sextets. Anthracene can host

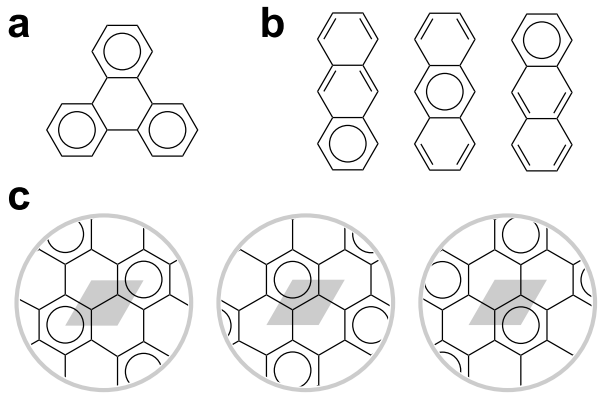

Figure 2.2: Clar formulas for (a) triphenylene, (b) anthracene and (c) graphene. The unit cell of graphene is shown in gray.

only one Clar sextet at a time, but has three equivalent Clar formulas that again should be considered *resonating* between each other.[27] And graphene hosts a maximally dense network of Clar sextets that form a $(\sqrt{3} \times \sqrt{3})\mathrm{R}30^\circ$ superstructure with respect to its unit cell. In infinite graphene, this network of Clar sextets can be shifted between three equivalent positions.

So far, the introduction of Clar sextets has merely improved our *visualization* of the π-electron distribution. The understanding gained in this process, however, allows to make qualitative predictions about actual physical observables. By distinguishing between single bonds, aromatic bonds and double bonds,[28] bond lengths can be predicted on a qualitative level. The relative thermodynamic stability of different molecules can be judged by analyzing the degree of π-electron delocalization via counting of Clar sextets. And finally, the π-electron distribution *itself* is an observable that is accessible, for example, in scanning tunneling microscopy.

Clar's theory has been applied extensively to nanographenes [85]. In the case of graphene nanoribbons, it has been demonstrated that the predictions of Clar's theory concerning bond lengths and π-electron distribution as a function of edge geometry and passivation are in agreement with density functional theory calculations [86]. In particular, Clar's theory provides a simple explanation for the localized states found at monohydrogenated graphene zigzag edges.

As shown in Figure 2.3 (a), based on the ordinary Kekulé structures only a single Clar sextet can be placed directly at a monohydrogenated zigzag edge. In comparison to infinite graphene, the π-electrons thus have significant less

[27] When considering the superposition of Clar structures, care must be taken in order to avoid counting certain Kekulé structures multiple times. In the case of anthracene, the Kekulé structures represented by the central Clar formula in Figure 2.2 (b) are already covered by the two other Clar formulas.

[28] With corresponding bond orders of $1, 1.5$ and 2.

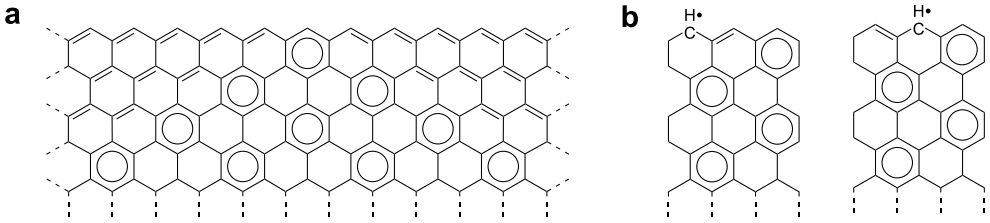

Figure 2.3: (a) Aperiodic Clar formula for infinite zigzag edge. (b) Periodic Clar formulas for infinite zigzag edge, enabled by introducing one unpaired electron every three 'zags'.

opportunity to delocalize, resulting in a low thermodynamic stability. If, however, a double bond is broken in order to introduce an unpaired electron at every third "zag", the dense network of Clar sextets of graphene can be recovered (see Figure 2.3 (b)).

The breaking of double bonds constitutes a relaxation of the usual requirement that Kekulé structures form the basis for determining the π-electron distribution. The stabilization gained by the delocalization can, however, outweigh the cost of the bond breaking. When this is the case, Clar's theory predicts zigzag edges to be characterized by highly reactive electronic states that are localized near the edge and host one electron every three "zags" – just as predicted by higher-level theories such as tight binding [87] or density functional theory [88].

2.4.2 Tight binding

In the tight binding approach, the problem of determining the electronic wave function in all of space is reduced to finding its optimal representation in a basis of pre-determined orbitals that are localized at atomic *sites*. These orbitals may be (linear combinations of) atomic orbitals, Wannier functions that are adapted specifically to the system under investigation or any set of localized functions that can act as an appropriate basis for the electronic wave function. The electronic structure problem is usually further simplified by neglecting the Coulomb interaction between electrons, but the tight-binding method can be extended in numerous ways, providing a smooth transition towards more sophisticated and even *ab initio* electronic structure methods on localized basis sets.[29]

For the case of graphene, the tight-binding representation can be made particularly simple [90, 91]. Since the main interest concerns the delocalized π-electrons, which are less strongly bound than the electrons in the σ-bonds, one can start by representing each carbon atom by a single $2p_z$ orbital. Fur-

[29] See, for example, the self-consistent-charge density-functional tight-binding binding approach [89].

thermore, all carbon atoms are electronically equivalent and have three nearest neighbors, while the next-nearest neighbor distance is larger by a factor of $\sqrt{3} \approx 1.7$. As a first approximation, interaction between carbon sites can therefore be restricted to nearest neighbors.

The corresponding tight-binding Hamiltonian is written as

$$\hat{\mathcal{H}} = -t \sum_{\langle ij \rangle} \hat{c}_j^\dagger \hat{c}_i + \hat{c}_i^\dagger \hat{c}_j \tag{2.58}$$

where the sum extends over pairs of nearest neighbors, $\hat{c}_i^\dagger, \hat{c}_j$ are the electron creation and annihilation operators at site i and j (with orbitals ϕ_i, ϕ_j) and t is the nearest-neighbor hopping[30] integral.

Conceptually, hopping integrals arise from the interatomic matrix elements $t_{ij} = -\langle \phi_j | \sum_{j \neq i} V(\mathbf{r} - \mathbf{r}_i - \mathbf{r}_j) | \phi_i \rangle$ where $V(\mathbf{r})$ is the potential associated with an isolated site. In practice, however, t is usually treated as a parameter that is used to fit the resulting electronic band structure against experiment [92] or *ab initio* calculations [91], yielding values in the range between 2.5 and 3 eV [93]. Furthermore, since the direct overlap $s_{ij} = \langle \phi_j | \phi_i \rangle$ between neighboring orbitals is found to be below 0.1 in graphene [93] it may be neglected, leaving t as the sole parameter of the model. Note that this makes the model equivalent to the Hückel molecular orbital theory [94] with resonance integral $\beta = t$ and the Coulomb integral α set to zero.

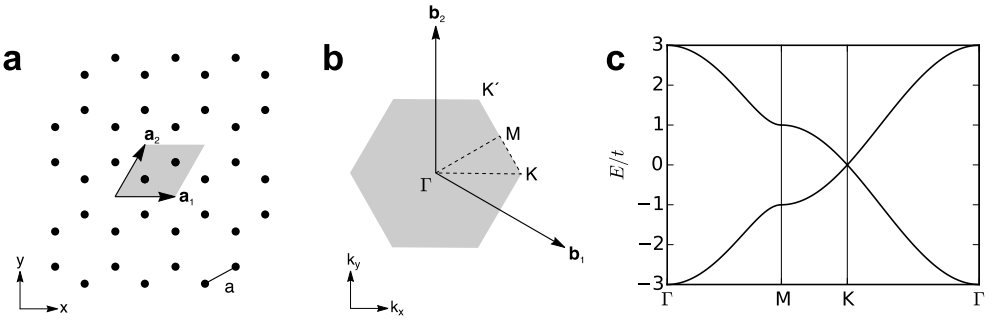

Figure 2.4: (a) Real space representation of graphene with lattice vectors $\mathbf{a}_1, \mathbf{a}_2$ of primitive cell and nearest-neighbor distance a. (b) Reciprocal lattice vectors $\mathbf{b}_1, \mathbf{b}_2$ and first Brillouin zone. Setting $a = 1$, $\Gamma = (k_x, k_y) = (0, 0)$, M $= (\frac{\pi}{\sqrt{3}}, \frac{\pi}{3})$, K $= (\frac{4}{3}\frac{\pi}{\sqrt{3}}, 0)$. (c) Band structure corresponding to (2.59), following the path indicated in (b).

For the two-dimensional bipartite hexagonal lattice of graphene, this model yields the dispersion

$$E(\mathbf{k}) = \pm t \sqrt{3 + 2\cos(\sqrt{3}k_x) + 4\cos(\sqrt{3}k_x/2)\cos(3k_y/2)} \tag{2.59}$$

[30] Also known as *transfer* integral.

where $\mathbf{k} = (k_x, k_y)$ is given in units of $1/a$, $a = 0.142\,\mathrm{nm}$ being the carbon-carbon bond length in graphene [95]. As shown in Figure 2.4 (c), this formula already predicts the semimetallic nature of graphene, including the linear dispersion at the K and K' points.

Furthermore, it allows to study the local electronic structure near graphene edges [87, 96]. When the edge carbon atoms are assumed to be passivated by one hydrogen atom each, they are sp^2-hybridized and thus each contribute one π-electron, just like the carbon sites in the interior. In nearest-neighbor tight binding, the edge boundary condition simply requires the wave function to vanish on the nearest neighbor sites *outside* the edge. Figure 2.5 shows the lowest π-electronic state of a graphene nanoribbon with armchair edges (b) and a graphene nanoribbon with zigzag edges (c).

For the case of the AGNR, the periodic repetition[31] of the eigenstate constitutes a standing wave on the graphene lattice. This standing wave is nothing but the superposition of two graphene eigenstates with $\mathbf{k} = (\pm r\frac{2\pi}{2w}, k_y)$, where the width of the AGNR is given by $w = \frac{\sqrt{3}}{2}(M+1)$ and $r \in \{1, \ldots, M\}$. The electronic dispersion of AGNRs is therefore obtained directly from equation (2.59) by inserting $\mathbf{k}$, which corresponds to cutting the dispersion of graphene along N straight lines of constant k_x (see Figure 2.6).

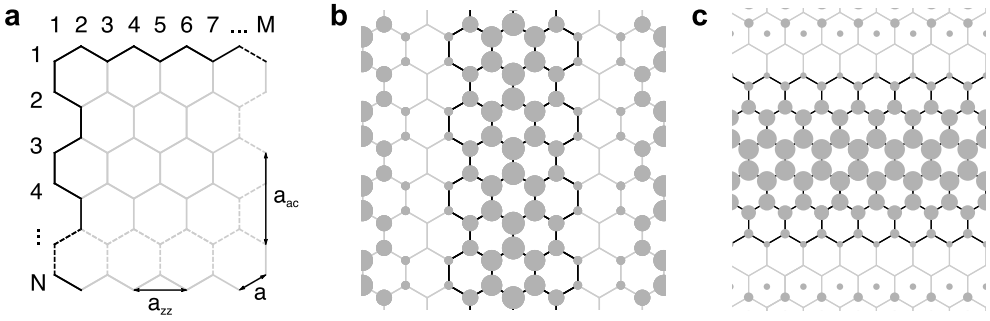

Figure 2.5: (a) Numbering scheme for widths of ribbons with armchair and zigzag edges. The lattice constants are related by $a_{ac} = \sqrt{3}a_{zz} = 3a$. (b) Lowest π-electronic state of $M = 7$ AGNR, repeated periodically. (b) Lowest π-electronic state of $N = 6$ ZGNR, repeated periodically. The wave function at site j is represented by a circle with area $\propto |\psi(\mathbf{r}_j)|$.

For ribbons with zigzag edges, Figure 2.5 illustrates that the periodic repetition of their eigenstates does not fall on the graphene lattice. The eigenstates can not be represented as a linear combination of two graphene eigenstates. They can, however, still be obtained analytically and their dispersion[32] can

[31] With alternating signs.

[32] Except the localized edge states, which are indicated as dotted lines in Figure 2.6 (a) and (c).

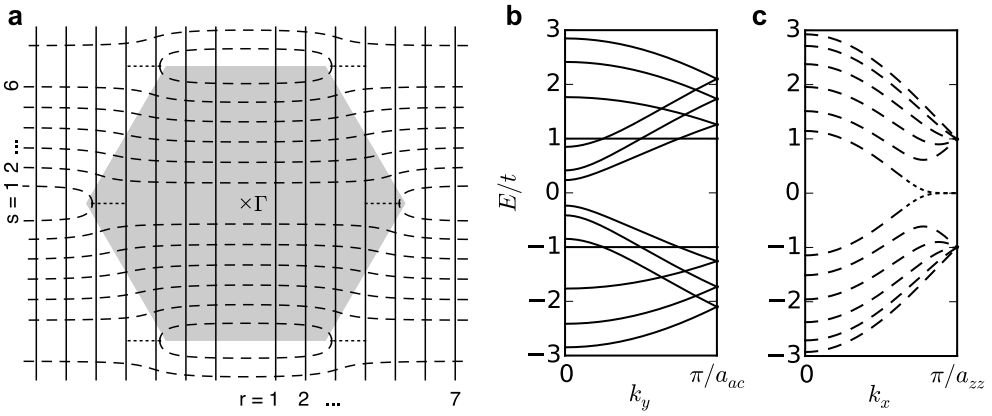

Figure 2.6: (a) Brillouin zone of graphene with cutting lines for $M = 7$ AGNR (continuous) and $N = 6$ ZGNR (dashed). Band structures of $M = 7$ AGNR (b) and $N = 6$ ZGNR (c), plotted in their respective first Brillouin zones.

still be represented as N cuts of the graphene dispersion, albeit not along straight lines [97] (see Figure 2.6).

In agreement with Clar's theory, the model predicts the existence of non-bonding electronic states that are localized near the zigzag edge. The corresponding energy band, shown in Figure 2.6 for the $N = 6$ ZGNR, is metallic for ZGNRs of all width.

The band gap of AGNRs is given by[33]

$$\triangle = \begin{cases} 0 & M = 3m-1, \quad r = 2m \\ -2t\left[1 + 2\cos\left(\frac{2m+1}{3m+1}\pi\right)\right] & M = 3m, \qquad r = 2m+1 \\ -2t\left[1 + 2\cos\left(\frac{2m+1}{3m+2}\pi\right)\right] & M = 3m+1, \quad r = 2m+1 \end{cases} \tag{2.60}$$

where m is an integer and r denotes the index of the band closest to the Fermi level. Only for AGNRs of width $M = 3m - 1$ do the cutting lines cross the K point, resulting in a vanishing gap. AGNRs of other widths are predicted to be semiconducting with band gaps $\Delta \propto 1/M$ for $M \to \infty$.

The formal equivalence with the Hückel molecular orbital theory allows to transfer the graph theoretical results obtained in this field to the tight binding description. A graphene nanostructure may be regarded as a hexagonal[34] graph, the carbon atoms being its *vertices* $\{v_i\}$ and the bonds between carbon atoms its *edges*. The nearest-neighbor tight-binding Hamiltonian (2.58) is then given simply by $(-t)$ times the *adjacency matrix* [98, 99]

$$A_{ij} = \begin{cases} 1 & v_i, v_j \text{ adjacent} \\ 0 & \text{otherwise} \end{cases}$$

[33]Please note that the formulas for the band gap of AGNRs given in equation (24) of reference [97] seem to be incorrect.

[34]Also called *benzenoid* graph.

Since the trace of A vanishes, so does the sum of its eigenvalues, i.e. $\sum_i \varepsilon_i = 0$, where $\{\varepsilon_i\}$ are the energies associated with both occupied and empty orbitals.

For hexagonal graphs, the number of negative and positive eigenvalues, corresponding to the number of bonding and antibonding orbitals, are equal [100]. Furthermore, their number can be found by counting the maximum number of pairwise nonadjacent edges β, i.e. the maximum number of double bonds in the corresponding Kekulé structure [100]. Since the total number of orbitals is given by the total number of vertices N_v, the number of zero-energy *non-bonding* orbitals is obtained as $\eta = N_v - 2\beta$. These considerations can be used to classify the electronic structure of nanographenes based on topological arguments only [101]. Note, however, that η is *not* equal to the number of edge-localized states, since their energies may differ from zero.

The nearest-neighbor single-orbital tight-binding model can be extended in numerous ways. Respecting the non-zero overlap integrals results in breaking particle-hole symmetry [91]. Site-dependent potentials may be introduced in order to model symmetry breaking due to a supporting substrate or to capture the different chemical environment at the edges [88]. The range of hopping may be extended. Allowing hopping between 2nd-nearest neighbors has been shown to affect the electronic structure near the Fermi level only by a rigid shift[35] [102]. Hopping between between 3rd-nearest neighbors, on the other hand, plays a significant role [103]. Increased flexibility may also be obtained by enlarging the basis set, e.g. to three orbitals per carbon site [104]. The additional complexity introduced by these extensions, however, comes at the cost of additional parameters, which are typically fitted to band structures calculated by *ab initio* methods.

The extensions described above have in common that the electrons are still treated as non-interacting Fermions. In GNRs with widths in the low nm regime dielectric screening is reduced significantly, giving rise to enhanced Coulomb interactions between quasiparticles. It is therefore unlikely that any of these models can be fitted to accurately describe the quasiparticle band structure of graphene nanoribbons over the whole range of widths from narrow GNRs up to graphene [104].

2.4.3 The Hubbard model

One extension of the tight-binding model that *does* introduce explicit Coulomb interactions is the Hubbard model [105]

$$\hat{\mathcal{H}} = -t \sum_{\langle ij \rangle, \sigma} \left(\hat{c}^\dagger_{j\sigma} \hat{c}_{i\sigma} + \hat{c}^\dagger_{i\sigma} \hat{c}_{j\sigma} \right) + U \sum_i \hat{n}_{i\uparrow} \hat{n}_{i\downarrow} \tag{2.61}$$

where the electron spin $\sigma \in \{\uparrow, \downarrow\}$ is now made explicit, $\hat{n}_{i\sigma} = \hat{c}^\dagger_{i\sigma} \hat{c}_{i\sigma}$ is the spin-resolved electron density at site i and $U > 0$ describes the energy penalty

[35] To first order in the hopping integrals.

associated with the on-site Coulomb repulsion between two electrons of different spin.[36]

The physics described by the Hubbard model is that of a competition between the kinetic energy of electrons, which is minimized by *delocalization*, and the Coulomb energy, which favors complete *localization* of each electron on one lattice site. The apparent simplicity of this lattice model for a short-range Coulomb interaction is deceptive. The Hubbard term is diagonal in real space, but non-diagonal in momentum space, while exactly the opposite is true for the tight-binding term. Today, more than half a century after Hubbard's original description of the model, exact solutions for ground state energy, excitation spectrum, etc. are available only for one-dimensional chains, where two electrons passing each other must actually hop directly 'through' each other [106].[37]

Some properties of the exact Hubbard model are known that are relevant to graphene. Lieb proved for bipartite lattices at half-filling[38] that the ground state is non-degenerate and its total spin S is given by $S = \frac{1}{2}|N_A - N_B|$, where N_A and N_B are the number of atoms of the two sublattices [107]. The theorem holds equally for periodic and finite structures [107]. In particular, the total spin of structures with balanced sublattices, such as zigzag graphene nanoribbons, is always equal to zero. Furthermore, Sorella and Tosatti performed quantum Monte Carlo calculations for the honeycomb lattice at zero temperature [108], showing that a transition from the semi-metallic to an insulating state occurs at $U/t = 4.5 \pm 0.5$.

Usually, however, the computation of spectral properties and electron distributions for specific graphene nanostructures makes it necessary to introduce approximations. In this context it is helpful to know the relative magnitude of the two model parameters t and U. Like t, U is not a physical observable and is obtained by fitting models to experiment. Following a recent review [109], the data concerning U seems to be relatively scarce. From studying the localized spin distribution associated with solitons in polyacetylene,[39], an effective $U \approx 3\,\mathrm{eV}$ was extracted [111]. Assuming that the value of U in graphene is similar, one obtains $U/t \approx 1$. This means that graphene is neither in the extreme of $U \ll t$, where Gutzwiller's variational approach would yield a semimetal with a renormalized hopping integral [112, 113], nor in the extreme $U \gg t$ of the Mott insulator, which can be described in terms of a Heisenberg model with antiferromagnetic coupling depending on t. A different route for approximation is therefore required.

In the mean field approximation, $\hat{n}_{i\sigma}$ is replaced by $\langle \hat{n}_{i\sigma} \rangle + \delta \hat{n}_{i\sigma}$ and terms

[36] In a single-orbital model, two electrons of the *same* spin can never occupy the same lattice site due to the Pauli exclusion principle.

[37] Note that, in this sense, GNRs are not one-dimensional.

[38] And for a repulsive value of U.

[39] More precisely, in thin films of polyacetylene of several nm thickness [110].

of $O(\delta\hat{n}_{i\sigma}^2)$ are neglected, resulting in

$$\hat{\mathcal{H}} = -t \sum_{\langle ij\rangle,\sigma} \left(\hat{c}_{j\sigma}^\dagger \hat{c}_{i\sigma} + \hat{c}_{i\sigma}^\dagger \hat{c}_{j\sigma} \right) + U \sum_i \langle \hat{n}_{i\uparrow}\rangle \hat{n}_{i\downarrow} + \langle \hat{n}_{i\downarrow}\rangle \hat{n}_{i\uparrow} - \langle \hat{n}_{i\uparrow}\rangle \langle \hat{n}_{i\downarrow}\rangle \quad (2.62)$$

The Hubbard term now involves only one-particle operators and the model (2.62) can be solved by determining the optimal distribution of spins in a self-consistent manner. Another way to arrive at the same approximation is to make the Ansatz of a single Slater determinant of spin-orbitals. In this sense, the mean-field approximation of the Hubbard model is nothing but the unrestricted Hartree Fock method on a lattice.

The mean-field approximation replaces a many-body problem by a one-body problem with an averaged *effective* interaction. In general, one may therefore expect this neglect of correlation to be less severe, when more interactions are involved in the average – the mean-field approximation of the Hubbard model should be more accurate in systems with higher coordination number Z of each lattice site.[40] A priori, the two-dimensional honeycomb lattice does not seem like a particularly good candidate in this respect. For example, the neglect of quantum fluctuations has been shown to lower the Mott-Hubbard transition from $U/t \approx 4.5$ to $U/t \approx 2.23$ on the honeycomb lattice [108]. Still, the ratio of $U/t \approx 1$ in graphene is relatively far below the transition and it has been observed that the mean-field description of graphene agrees reasonably well with exact diagonalization and Quantum Monte Carlo simulations [115]. This makes the mean-field Hubbard model a computationally inexpensive alternative to *ab initio* methods when studying the spin-distribution in nanographenes and its effect on the π-electronic structure [109].

[40] Note, however, that in the limit of $Z \to \infty$ the mean-field approximation of the Hubbard model does *not* converge to the exact solution, when the hopping integral is rescaled with $1/\sqrt{Z}$ [114].

2.5 Simulation of scanning tunneling microscopy

Scanning tunneling microscopy involves the tunneling of electrons between a sharp tip and a sample across a vacuum gap. Predicting the tunneling current as a function of the bias voltage and the relative position of tip and sample thus represents a special case of the general quantum transport problem.

Ab initio approaches to quantum transport typically divide the system into three parts, which are illustrated in Figure 2.7 (a): a left lead, a central region containing the contact geometry of interest – which may also be a vacuum gap – and a right lead. The metallic leads can be made semi-infinite using the concept of non-equilibrium Green functions (NEGF), allowing to focus all attention to the central region. Given an adequate description of the electronic structure of the central region, which may include explicit electron-electron interactions, the current-voltage characteristic can then be computed using the formulas given by Meir and Wingreen [116]. In the quantum transport setting, the approximation of treating the central region within (semi)local DFT and equating the Kohn-Sham energies with quasiparticle energies is particularly severe and can lead to overestimations of conductance of up to two orders of magnitude [117]. While it is possible to describe the central region in the *GW* approximation [118, 119], this approach is computationally expensive and strongly restricts the size of the central region that can be treated.

To make matters worse, in STM the atomic geometry of the tip is typically[41] unknown. Calculating the absolute value of the tunneling current is therefore usually not attempted in STM simulations, also because it is not necessary in order to obtain *qualitative* information about the relative variations in current when scanning the tip across the surface.

Note that, if desired, an order-of-magnitude assessment of the tunneling current is easily obtained by considering tunneling of free electrons through a barrier in one dimension. For a rectangular barrier of height $\bar{\phi}$ and width s, the current density at voltage $V \ll \bar{\phi}/e$ is given by [122]

$$j = \frac{e^2}{\hbar} \frac{\kappa}{4\pi^2 s} \exp(-2\kappa s)\ V \tag{2.63}$$

where $\kappa = \sqrt{2m_e\bar{\phi}}/\hbar$. In STM, the barrier height $\bar{\phi}$ may be approximated as the average work function of tip and sample. The length s is the effective distance over which tunneling occurs, which is slightly less than the distance between the nuclei [123]. In order to obtain a value for the current J, equation (2.63) is multiplied by an effective cross-sectional area $S(R)$ of the tip, as determined by the (estimated) tip radius R [123]. Similarly, given an experimental value for $J = jS(R)$, a rough estimate of the tip-sample distance may be obtained by inverting equation (2.63) for s.

[41] Recent progress in this respect includes the controlled functionalization of tips with Xe, Kr, NO, or CO [120, 121].

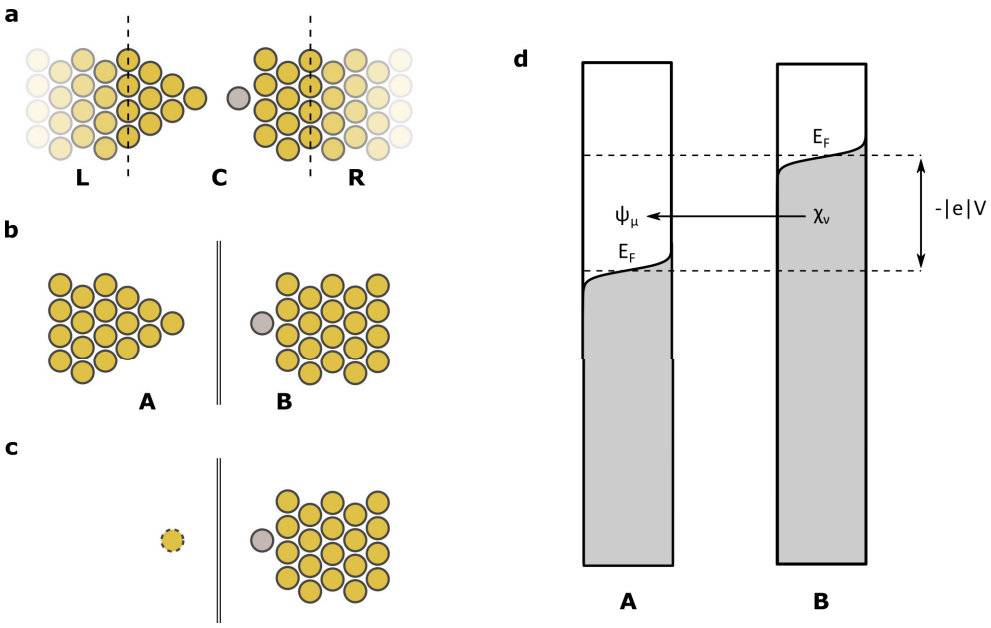

Figure 2.7: Modelling STM. (a) NEGF approach with semi-infinite left (L) and right (R) leads, connected via a central (C) region. (b) Bardeen approach for two well-separated electrodes A and B. (c) Tersoff-Hamann approximation, replacing the tip by an s-orbital. (d) Sketch of level occupancy in Bardeen approach in presence of negative sample bias V.

2.5.1 Bardeen's theory of tunneling

Most STM simulations are rooted in an approximation to the tunneling of interacting electrons due to Bardeen [124], who considered the tunneling between two well-separated electrodes A and B (see the sketch in Figure 2.7 (b)).[42] The Hamiltonian of the combined system may be written in second quantization as [126]

$$\hat{\mathcal{H}} = \hat{\mathcal{H}}_A + \hat{\mathcal{H}}_B + \hat{\mathcal{H}}_t, \tag{2.64}$$

$$\text{where} \quad \hat{\mathcal{H}}_A = \sum_{\mu} \hat{a}_\mu^\dagger \hat{a}_\nu \ , \tag{2.65}$$

$$\hat{\mathcal{H}}_B = \sum_{\nu} \hat{b}_\nu^\dagger \hat{b}_\nu \tag{2.66}$$

$$\text{and} \quad \hat{\mathcal{H}}_t = \sum_{\mu\nu} \delta(E_\mu - E_\nu) \left[M_{\mu\nu} \hat{a}_\mu^\dagger \hat{b}_\nu + M_{\mu\nu}^* \hat{b}_\nu^\dagger \hat{a}_\mu \right] \tag{2.67}$$

Here, $\hat{a}_\mu^\dagger, \hat{a}_\mu$ and $\hat{b}_\nu^\dagger, \hat{b}_\nu$ denote the quasiparticle creation and annihilation operators for the unperturbed states ψ_μ of electrode A and χ_ν of electrode B.

[42] Although formulated independently, Bardeen's approach can be obtained as an approximation of the NEGF approach [125].

E_μ, E_ν are the corresponding quasiparticle energies,[43], given with respect to the vacuum level of the respective electrode. Since A and B are separated by a vacuum barrier, into which both ψ_μ and χ_ν decay exponentially, their overlap $S_{\mu\nu} = \langle\psi_\mu|\chi_\nu\rangle$ becomes small when the separation between electrodes A and B is large. Neglecting terms of $O(S_{\mu\nu}^2)$ [126], Bardeen showed that the matrix elements $M_{\mu\nu}$ of the *transfer* Hamiltonian $\hat{\mathcal{H}}_t$ can be expressed as

$$M_{\mu\nu} = \frac{\hbar^2}{2m}\int_\Sigma (\psi_\mu^* \nabla\chi_\nu - \chi_\nu \nabla\psi_\mu^*)\cdot d\mathbf{S} = M_{\nu\mu}^* \tag{2.68}$$

This surface integral of the current operator is to be performed on a separation surface Σ between electrode A and B [124]. Σ may, in principle, be chosen freely within the barrier. In numerical calculations, it should be advantageous to follow regions, where the magnitudes of ψ_μ and χ_ν are similar.

A finite bias voltage V between electrodes A and B gives rise to an electric field in the junction, which, in principle, modifies the states ψ_μ, χ_ν. As long as V remains small compared to the barrier height, however, this modification may be neglected. The tunneling current is then determined merely by the voltage, the tunneling matrix elements $M_{\mu\nu}$ and the occupancy of the states involved in the tunneling process. Figure 2.7 (d) illustrates the case of keeping electrode A grounded and applying a negative voltage V to electrode B. One obtains [126]

$$\begin{aligned} I(V,T) = \frac{2\pi e}{\hbar}\sum_{\mu\nu}\delta(E_\mu - E_\nu + eV)|M_{\mu\nu}|^2\rho_A(E_\mu)\rho_B(E_\nu) \\ \underbrace{[f(E_\mu)(1-f(E_\nu)) - (1-f(E_\mu))f(E_\nu)]}_{f(E_\mu)-f(E_\nu)} \end{aligned} \tag{2.69}$$

where $f(E,T) = 1/\left(1+\exp\left[\frac{E-E_F}{k_BT}\right]\right)$ is the Fermi-Dirac distribution, E_F is the Fermi energy *of the respective electrode* and ρ_A, ρ_B are the densities of states[44] of the electrodes A, B. Note that the convention $e = |e|$ is adopted here.

When the temperature is low enough that k_BT is smaller than the experimental energy resolution, the formula simplifies to

$$I(V,0) = \frac{2\pi e}{\hbar}\sum_{\mu\nu}\delta(E_\mu - E_\nu + eV)|M_{\mu\nu}|^2\rho_A(E_\mu)\rho_B(E_\nu) \tag{2.70}$$

where the sum is now limited to the states within the bias window, corresponding to the range between E_F and $E_F - eV$ for electrode A and the range between E_F and $E_F + eV$ for electrode B.

[43] Note that the delta function signifies *elastic* tunneling. For inelastic tunneling, e.g. by excitation of phonons, please see [126, 127].

[44] Summed over both spins.

2.5.2 The Tersoff-Hamann approximation

The ingredients of formula (2.69) can, in principle, all be obtained from separate *ab initio* electronic structure calculations of the electrodes A and B, representing the tip and the sample. In order to simulate an STM image, however, this approach still requires the tunneling matrix elements $M_{\mu\nu}$ to be recomputed for every position of the tip. Given the lack of knowledge about the exact atomic structure of the tip, it seems reasonable to replace the atomistic description of the tip by a suitable analytical model in order to simplify the evaluation of the matrix elements. While this means that tip and sample are no longer treated on equal footing, it also reflects the fact that STM is usually performed in order to study the sample, not to study the tip.

In the popular Tersoff-Hamann approximation [128], the tip electrode A is assumed to have a constant density of states and is represented by a single s-orbital

$$\psi_\mu \propto \frac{1}{\kappa|\mathbf{r}-\mathbf{r}_0|} e^{-\kappa|\mathbf{r}-\mathbf{r}_0|} \tag{2.71}$$

centered at position $\mathbf{r}_0$ and inverse decay length κ. Given the exponential decay of the tip wave functions with distance, it seems reasonable to assume that for sharp tips, such as the one sketched in Figure 2.7, the majority of the tunneling current flows through the atom of the tip that is closest to the sample. But even for blunt tips, the wave functions ψ_μ will approach the general form (2.71) with increasing distance from the tip [128].

Using approximation (2.71) for ψ_μ, the tunneling matrix element $M_{\mu\nu} \propto \chi_\nu(\mathbf{r}_0)$ becomes directly proportional to the sample wave function χ_ν evaluated at $\mathbf{r}_0$ [128]. Accordingly, the tunneling current is obtained as

$$I(V,0) \propto \sum_\nu |\chi_\nu(\mathbf{r}_0)|^2 \rho_B(E_\nu - eV) \tag{2.72}$$

where the sum extends over all states χ_ν of electrode B with energy E_ν in between E_F and $E_F + eV$. The product in equation (2.72) is nothing but the local density of states (LDOS) evaluated at $\mathbf{r}_0$. Constant-current STM images thus are contours of constant local density of states, integrated in the bias window. Not only does this provide a very intuitive interpretation of STM images, it also makes calculating an STM image essentially as simple as calculating the local density of states of the sample.

When little is known about the tip shape, the Tersoff-Hamann approximation is typically the best guess. In particular at short tip-sample distances, however, higher angular momentum components of the tip wave functions can play a significant role [129]. If the tip wave function is known, for example because the tip is a CO molecule [120], the Tersoff-Hamann approximation can be extended to include higher angular momenta by expanding the tip wave function in terms of spherical modified Bessel functions [129]. The corresponding matrix elements are then found to be proportional to a combination

of the sample wave functions χ_ν and their spatial derivatives at the center at the tip, and the contributions from different angular momentum channels can simply be summed together.

2.5.3 Extrapolation of numerical wave functions

From a numerical point of view, care still needs to be taken, when STM simulations are to be performed at realistic tip-sample distances of several Å. As pointed out by Tersoff [130], neither localized basis sets, such as Gaussian-type orbitals, nor propagating plane waves are well-suited to describe exponential decay over many orders of magnitude. In order to obtain an accurate local density of states at sufficiently large distances from the sample, it is therefore convenient to extrapolate the electronic wave functions, starting from a plane S parallel to the surface of the sample. The plane is chosen close enough to the sample to ensure accurate numerical values of the wave functions χ_ν, but far enough from the sample in order for the (Kohn-Sham) potential V to be essentially constant within the plane [130].

Let z be the direction of the surface normal, then the wave functions χ_ν of a periodic sample take the form of Bloch states

$$\chi_{\nu\mathbf{k}}(\mathbf{r}) = u_{\nu\mathbf{k}}(\mathbf{r}) e^{ik_x x + ik_y y} \tag{2.73}$$

with $\mathbf{r} = (x, y, z)$, in-plane crystal wave vector $\mathbf{k} = (k_x, k_y)$ and lattice-periodic function $u_{\nu\mathbf{k}}(\mathbf{r})$. Both $u_{\nu\mathbf{k}}(\mathbf{r})$ and the potential $V(\mathbf{r})$ can be developed into two-dimensional Fourier series

$$u_{\nu\mathbf{k}}(\mathbf{r}) = \sum_{\mathbf{G}} u_{\nu\mathbf{k}}(\mathbf{G}; z) e^{iG_x x + iG_y y} \tag{2.74}$$

$$\text{with} \quad u_{\nu\mathbf{k}}(\mathbf{g}; z) = \frac{1}{(2\pi)^2} \int u_{\nu\mathbf{k}}(\mathbf{r}) e^{-iG_x x - iG_y y}\, dx\, dy \quad , \tag{2.75}$$

$$\text{and} \quad V(\mathbf{r}) = \sum_{\mathbf{G}} V(\mathbf{G}; z) e^{iG_x x + iG_y y} \approx V(\mathbf{0}; z), \quad z > z_0 \tag{2.76}$$

$$\text{with} \quad V(\mathbf{G}; z) = \frac{1}{(2\pi)^2} \int V(\mathbf{r}) e^{-iG_x x - iG_y y}\, dx\, dy \quad . \tag{2.77}$$

Here, the fact has been used that $V(\mathbf{r})$ is essentially constant within the plane at $z = z_0$ and beyond.

Plugging (2.74) and (2.76) into the Schrödinger equation

$$\left(-\frac{\hbar^2}{2m} \triangle + V(\mathbf{r}) \right) \chi_{\nu\mathbf{k}}(\mathbf{r}) = E_{\nu\mathbf{k}} \chi_{\nu\mathbf{k}}(\mathbf{r}) \tag{2.78}$$

yields a differential equation for $u_{\nu\mathbf{k}}(\mathbf{r})$

$$\partial_z^2 u_{\nu\mathbf{k}}(\mathbf{G}; z) = \left((\mathbf{k} + \mathbf{G})^2 - \frac{2m}{\hbar^2} (E_{\nu\mathbf{k}} - V(\mathbf{0}; z)) \right) u_{\nu\mathbf{k}}(\mathbf{G}; z) \tag{2.79}$$

which may be integrated, starting from the plane $z = z_0$.

If the plane can be chosen far enough from the surface that $V(\mathbf{0}; z_0)$ has already reached the *vacuum* potential $V(\mathbf{0}; \infty) =: V_0$, then the exponentially decaying solution of (2.79) is obtained analytically as [131]

$$u_{\nu\mathbf{k}}(\mathbf{G}; z) = u_{\nu\mathbf{k}}(\mathbf{G}; z_0) e^{-\kappa(z-z_0)} \tag{2.80}$$

$$\text{with} \quad \kappa = \sqrt{(\mathbf{k}+\mathbf{G})^2 - \frac{2m}{\hbar^2}(E_{\nu\mathbf{k}} - V_0)} \tag{2.81}$$

where $\frac{2m}{\hbar^2}(E_{\nu\mathbf{k}} - V_0) > 0$ for any bound state $\psi_{\nu\mathbf{k}}$. Once a Fourier series (2.74) has been computed on a suitable plane $z = z_0$, equation (2.81) provides the analytical extrapolation for $z > z_0$.

Note that it is not always possible to choose a plane $z = z_0$ according to the conditions mentioned above, in particular when the surface of the sample is significantly corrugated. In this case, the wave function $\chi_{\nu\mathbf{k}}$ can be matched on a non-planar surface adapted to the corrugation of the sample, such as an isosurface of the potential $V(\mathbf{r})$.

CHAPTER 3

Termini of the $M = 7$ armchair graphene nanoribbon

3.1 Plausible candidates for the atomic structure

As outlined in the introduction, the bottom-up approach solves a major problem concerning the application of graphene nanoribbons in field effect transistors: to open a significant band gap without introducing sources of scattering. This is achieved by synthesizing GNRs with widths below 10 nm and atomically precise edges.

Besides indications from Raman spectroscopy [16], the quality of the GNRs was judged by high-resolution scanning tunneling microscopy. Figure 3.1 shows an STM image of the 7-AGNR, where the sequence of anthene units is clearly discernible and the armchair edge is evidently free of carbon defects.

Figure 3.1: Constant-current STM image of 7-AGNR on Au(111) at sample bias $U = -0.11\,\mathrm{V}$ and set point $I = 210\,\mathrm{pA}$. Data recorded by Jinming Cai.

As for the *passivation* of the armchair edge, in principle, three basic possibilities can be considered: the edge carbon atoms may be passivated by two hydrogen atoms, by single hydrogen atoms or they may be bare carbon atoms.[1] Previous theoretical work, however, strongly suggested monohydrogenated armchair edges. First, the experimental electronic structure agrees with many-body perturbation theory calculations of (infinite) monohydrogenated 7-AGNRs, which account for the screening of the metal [21]. This excludes the possibility of dihydrogenated edges, which would essentially constrict the aromatic system to the one of a 5-AGNR that belongs to the quasi-metallic $M = 3m - 1$ family [96]. Second, a detailed theoretical study of the cyclodehydrogenation process for the 7-AGNR indicates that the edges are left in the monohydrogenated state [22]. And third, DFT calculations show that monohydrogenated armchair edges are the most stable configuration at the low partial hydrogen pressures corresponding to UHV conditions [133]. Besides these theoretical considerations, the possibility of completely unpassivated edges would imply a significant increase in the interaction with the substrate, which was not compatible with the observation that isolated GNRs were mobile on the Au(111) surface down to temperatures of 77 K.

While the atomic structure of the armchair edges could be considered as clarified, the question of the atomic structure at the termini of the GNRs remained open. There are several factors that make this question particularly

[1] Hydrogen is produced during the cyclodehydrogenation reaction and is the most prevalent residual gas in ultra-high vacuum systems.

interesting. First, the termini are where one would imagine to make contacts in an electronic transport experiment. For example, in a very recent work, Koch and coworkers picked up a 7-AGNR at one terminus with an STM tip and measured the current as a function of tip height and bias [134]. Second, the termini are the point where the polymerization reaction terminated. While 7-AGNRs of 100 nm length and more have been observed, the average length of the synthesized 7-AGNRs in the bottom-up approach is around 30 nm^2 [16] and the limiting factors were not identified. Pinning down the atomic structure of the termini may provide insight into this matter, e.g. by clarifying whether defective molecules are responsible for the termination of polymerization. And finally, in the case of the 7-AGNR, the termini are very short zigzag edges and give rise to a very peculiar local density of states near the Fermi level indicating the presence of a localized electronic state.

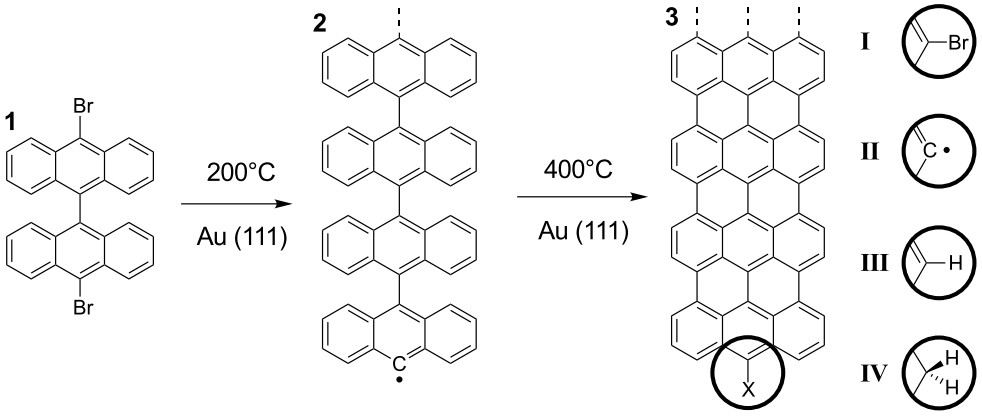

Figure 3.2: On-surface synthesis of 7-AGNRs with plausible terminations I-IV.

Figure 3.2 shows a scheme of the bottom-up synthesis of the 7-AGNR together with plausible candidates for the termination. In case I, the bromine atom has failed to detach from the precursor molecule at the terminus of the ribbon[3]. In case II, debromination has occurred as intended, leaving a radical behind that is stabilized by the metal surface. Cases III and IV consider the hydrogen passivation of the radical and the addition of a second hydrogen atom at the same site.

In the following, STM simulations for these candidates are performed within the framework of density functional theory and compared to STM experiments in order to determine the correct atomic structure at the termini. The discussion focuses on GNRs adsorbed on Au(111), but simulations and experiments have also been performed on the Ag(111) substrate (see Figure 3.5) and the conclusions drawn apply to both substrates.

[2]Corresponding to $\approx$ 100 precursor molecules.

[3]Or has reattached after dissociation.

3.2 Computational approach

Even though the driving question concerns the atomic structure of the adsorbed GNR, the substrate cannot be neglected. In scanning tunneling microscopy simulations, the substrate plays a twofold role, influencing both the atomic structure of the adsorbate and its electronic structure.

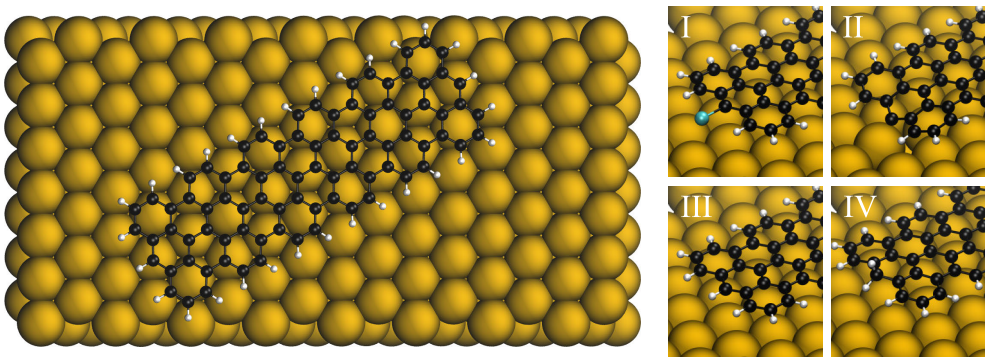

Figure 3.3: Slab and adsorption geometry. Left: Optimized atomic structure of 7-AGNR adsorbed on unreconstructed Au(111), following the <110> direction on the surface. Right: Close-ups of 7-AGNR termini for cases I-IV.

As illustrated in Figure 3.3, the substrate was modeled by four Au(111) layers in the repeated slab geometry, the two lower layers being kept fixed at the equilibrium lattice parameter of bulk Au. A cell of $20.8 \times 41.2\,\text{Å}^2$ hosted one 7-AGNR consisting of three fused precursor molecules. The substrate was saturated by hydrogen on the opposing side in order to remove the surface state and to speed up convergence of the electronic structure with respect to the number of atomic layers [135]. In total, the simulation cell therefore contained ≈ 700 atoms. 30 Å of vacuum were included perpendicular to the surface to avoid interaction between the periodic replicas of the system. Similar parameters were used for the Ag(111) surface. During geometry optimization, the atomic positions were relaxed until all forces were below $3 \cdot 10^{-4}$ Hartree atomic units.

Electronic structure calculations were performed within the framework of density functional theory using the PBE exchange-correlation functional [63] with the DFT-D3 dispersion correction [68]. The CP2K code [136] was used together with Goedecker-Teter-Hutter pseudopotentials [137] and DZVP (TZV2P) contracted Gaussian basis sets [138] for Ag, Au, Br (C, H). The charge density was expanded on a plane-wave basis set with kinetic energy cutoff 320 Ry.

Scanning tunneling microscopy simulations were performed in the Tersoff-Hamann approximation, based on the Kohn-Sham orbitals and eigenenergies. Since CP2K expands the Kohn-Sham orbitals on atom-centered Gaussian basis

sets (as described above), the orbitals are not properly represented in the vacuum region far from the sample. For the STM simulations, the orbitals have therefore been extrapolated into the vacuum region as described in section 2.5.3, matching the wave functions on an isosurface of the Hartree potential. A version[4] of the computer code written to perform this task has been made publicly available [139].

While an absolute determination of the tunneling current was not attempted, Simmons' formula was used to provide a rough estimate of the tip-sample distance corresponding to experimental tunneling parameters. The work function $\phi = 5.31\,\text{eV}$ of Au(111) [140] is assumed to be identical for tip and the sample and, following Tersoff and Hamann [128], a tip radius $R \approx 9\text{Å}$ is assumed. Using equation (11) of reference [123], the tunneling parameters in Figure 3.4 (b) are estimated to correspond to a distance of $\approx 6\,\text{Å}$ between the nuclei of the tip and the sample. This value could then be used as a guide when selecting the isovalues of the integrated local density of states in the STM simulation.

Concerning the adsorption configuration of the 7-AGNR, the (lack of) electronic interaction between the Au(111) surface and the bulk region of the 7-AGNR has been discussed in previous work [21]. For the finite 7-AGNR shown in Figure 3.3, different orientations were tested, but the total energy differences between the different relaxed configurations were found to be below 100 meV and no qualitative differences in the STM simulations were observed.[5] This is also in agreement with the experimental finding that stable imaging of isolated GNRs is impossible even at temperatures as low as 77 K. The potential energy landscape seen by the GNRs on Au(111) is therefore relatively flat and unlikely to significantly influence the electronic structure of the adsorbed GNRs.

Total energy differences for bromine removal and hydrogen addition were calculated with respect to the isolated *atomic* species adsorbed on the surface. For example, the total energy difference for hydrogen addition going from case III to case IV is calculated as

$$\Delta E = \frac{1}{2}(E_{IV} - E_{III} - (E_{slab+2H} - E_{slab}))$$

where E_{slab} is the total energy of the clean slab, $E_{slab+2H}$ refers to the slab plus two isolated adsorbed hydrogen atoms and $E_I \ldots E_{IV}$ denote the total energy of the slab plus adsorbed ribbon with the corresponding termination at *both* ends.

For the reaction of transforming case IV into case III by removing one hydrogen atom from the central carbon site, the minimum energy path was

[4] At the time of writing, the public Python implementation includes only extrapolation on a plane $z = z_0$.

[5] This statement is limited to the cases of saturated termini. In case II of the radical terminus, the strong interaction between terminus and substrate can induce larger energy differences between different configurations (up to 0.5 eV). These are however not related to registry matching in the usual sense.

determined through a nudged elastic band calculation. The starting guess was obtained from a linear interpolation between the initial and final states shown in Figure 3.7. Taking the C-H bond distance as the reaction coordinate, the climbing image method [141] was employed with a total of 20 images and a maximum distance of 0.6 Å between adjacent images.

3.3 Results and comparison with experiment

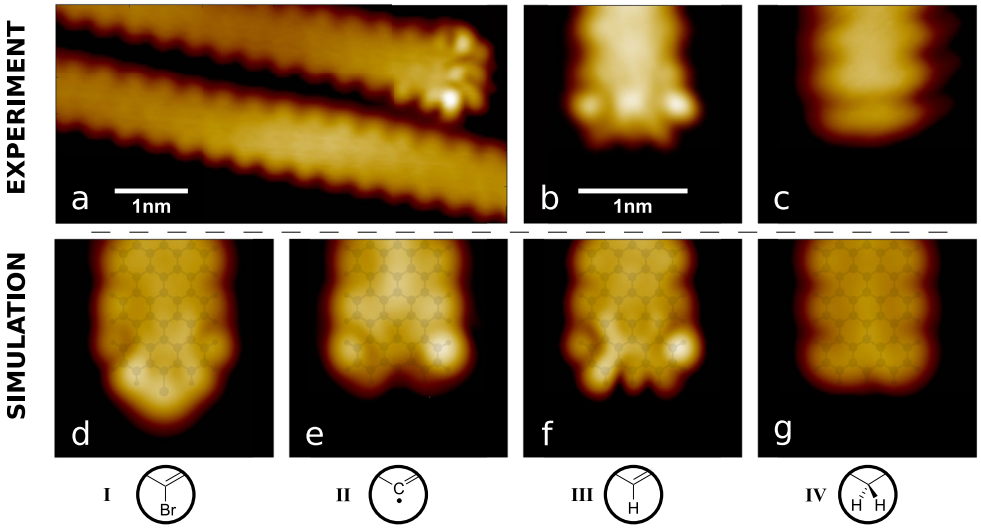

Figure 3.4: STM images of 7-AGNR termini on Au(111). (a) Characteristic appearance of the terminus (-0.11 V, 210 pA). (b) Close-up (-0.14 V, 50 pA). (c) Featureless terminus (0.10 V, 10 pA). (d-g) STM simulations for the four termini under consideration (-0.3 V, $\rho = 10^{-7}\text{Å}^{-3}$), overlaid with relaxed atomic structure. Experimental data recorded by Jinming Cai (a) and Hajo Söde (b-c).

Figure 3.4 (d-g) shows the resulting STM simulations for cases I-IV, in comparison with experimental images (b-c). The simulation of case I shows significant electron density on the Br atom, which is incompatible with the experimental images and thus rules out this candidate. The simulation of the radical II predicts the bare carbon atom to move down by about 1 Å towards the metal surface, leading to a buckling of the ribbon. Both comparison of the corresponding STM image with experiment and the high mobility of the GNRs exclude this possibility.

The question arises, whether the termini have somehow been passivated. Since the samples do not leave UHV conditions, bromine and hydrogen are the only plausible candidates for the passivating chemical species. Atomic hydrogen is generated on the surface during the cyclodehydrogenation step, when

eight hydrogens are lost per precursor monomer **1** in total [22]. While recombinative desorption of hydrogen from Au and Ag surfaces occurs already at room temperature [142], diffusing atomic hydrogen may as well passivate the radical termini.[6] Table 3.1 lists the total energy differences between different terminations, indicating that hydrogen passivation of case II lowers the energy by $1.6 - 2.1\,\mathrm{eV}$, where the variation arises from different possible chemisorption geometries of the radical on the surface. The corresponding reaction is expected to be almost barrierless.

Case	I	II	III	IV
ΔE [eV]	+1.8	+1.6...+2.1	0	-0.8

Table 3.1: Relative stability of different terminations according to the total energy difference ΔE, as defined in section 3.2. Case III is taken as the reference.

The terminus resulting from such a scenario constitutes a monohydrogenated zigzag edge (III). As discussed in chapter 2.4.2, single-orbital nearest-neighbor tight-binding predicts the existence of nonbonding electronic states near a monohydrogenated zigzag edge. The terminus of the 7-AGNR has three zigzag cusps, for which the model predicts the existence of exactly one localized edge state (also termed 'Tamm state' [134]), whose corresponding Kohn-Sham DFT orbital is shown in Figure 3.6 (a). The STM simulation of case III fits

[6] It may also be conceivable that, after cyclodehyodrogenation, some hydrogen 'diffuses' towards the terminus directly on top of the GNR.

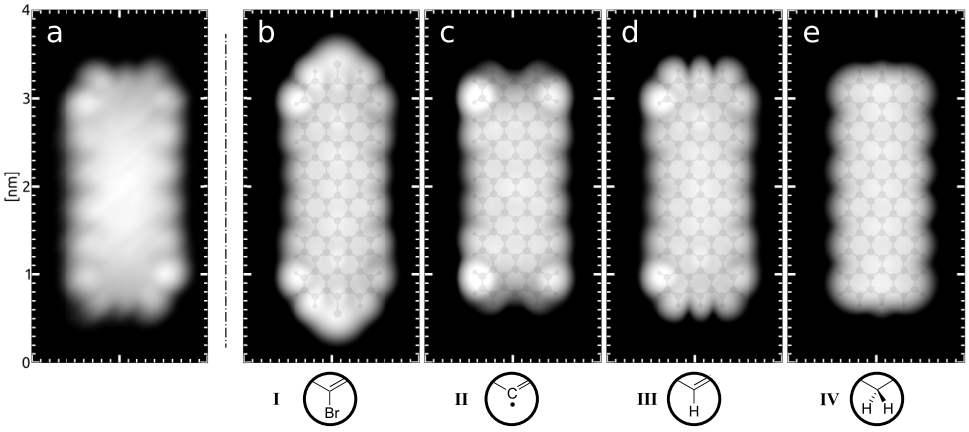

Figure 3.5: STM images of short 7-AGNR on Ag(111). (a) STM experiment (-1.89 V, 100 pA, 5 K). (b-e) STM simulations of terminations I-IV (-0.0 V, $\rho = 10^{-6}\text{Å}^3$), overlaid with relaxed atomic structure. Experimental data recorded by Rached Jaafar.

the experiment very well, reproducing the enlargement of the apparent width toward the terminus as well as the two 'eyes' and the three 'antennae'. In particular, both simulation and experiment reveal an accumulation of electron density on *one*[7] of the two carbon sublattices.

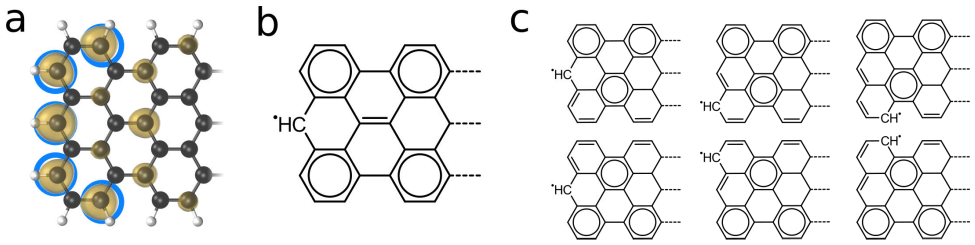

Figure 3.6: Tamm state at GNR terminus III and corresponding Clar formulas. (a) Constant-density isosurface based on a DFT calculation of the 7-AGNR in vacuum. The five carbon atoms with the highest weight of the Tamm state are highlighted in blue. (b-c) Clar formulas with maximum (b) and next-highest (c) number of Clar sextets.

Finally, case IV considers the addition of a second hydrogen at the same site, resulting in a H_2 termination of the central carbon atom. As indicated in Table 3.1, this further lowers the total energy by 0.8 eV, which can be rationalized in an intuitive way by employing Clar's theory. As discussed in chapter 2.4.1, for infinite monohydrogenated zigzag ribbons the aromaticity of Clar formulas is maximized by introducing one unpaired electron every three zigzag cusps. Figure 3.6 applies this reasoning to the monohydrogenated 7-AGNR (III). Considering only the Clar formulas with the maximum and next-highest number of Clar sextets, the unpaired electron may be introduced at five different carbon sites near the terminus. The comparison with the DFT calculation of the finite 7-AGNR in vacuum reveals that these are exactly the carbon sites with the highest weight of the Tamm state. Adding the second hydrogen (IV) pairs the electron and lowers its energy by forming a σ-bond, thereby removing it from the energetic window studied here via STM.

This is clearly not the case in the typical experimental STM images featuring the Tamm state shown in Figure 3.4 (a) and (b). However, about 15% of the GNR termini in the experiments appear featureless (Figure 3.4 (c)) as does the STM simulation of case IV. Featureless termini have also been reported in reference [134], where they are explained by carbon defects that would remove the Tamm state as well.

Atomic structure determination through STM is not always straightforward, in particular when the electronic states close to the Fermi level do not have significant weight on the atoms under investigation – here: the hydrogens at the terminus. Yet, in the particular case considered here, there is a way of

[7]The one including the outermost carbon atoms at the zigzag edge.

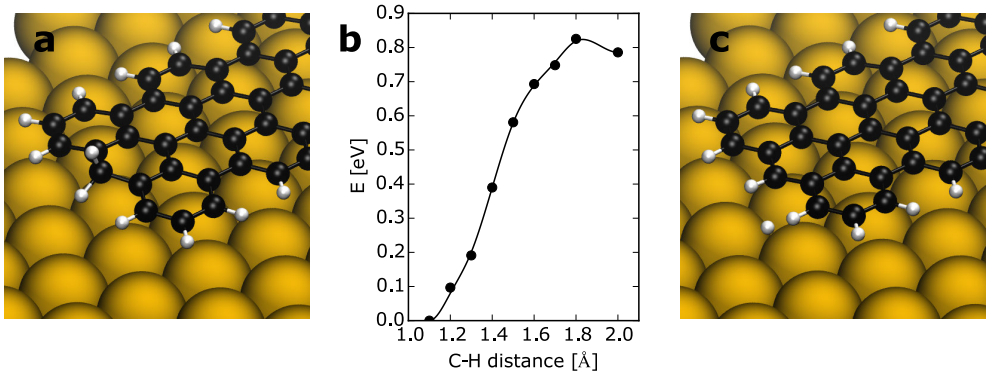

Figure 3.7: Nudged elastic band calculation for transforming case IV into case III by transfer of a hydrogen atom to the Au substrate. Shown are initial (a) and final (c) states together with the energy profile (b) along the reaction coordinate.

proving that the featureless termini indeed correspond to case IV by studying the effect of the electronic states on the carbon skeleton: If a terminus corresponds to case IV, then removing a hydrogen atom by a voltage pulse from the STM tip would transform it into case III and the Tamm state should appear in STM.

In order to evaluate the feasibility of such an experiment, the minimum energy path for the reaction was determined by a nudged elastic band calculation. As shown in Figure 3.7, the path does not involve significant barriers and the required energy is predicted to be less than 1 eV. This is less than the initial barrier of ≈ 1.35 eV predicted for the cyclodehydrogenation reaction of the 7-AGNR, which can also be induced by a voltage pulse of the STM tip [22]. Motivated by this finding, the tip-induced dehydrogenation experiment was indeed performed, confirming the prediction and thus identifying the featureless termini as case IV.

3.4 Conclusion and outlook

Soon after publication of this study, the atomic structure deduced from STM was confirmed by non-contact atomic force microscopy experiments, in which the atomic structure becomes more directly apparent [143]. Tip-induced dehydrogenation was also reproduced and extended to case II by removing also the last hydrogen atom from the central carbon atom [143].

The identification of hydrogen passivation of the ribbon termini has important implications for the understanding of the polymerization process, respectively its interruption. STM images taken after the polymerization step at $200°C$ sporadically show bianthryl monomers that already have undergone cyclodehydrogenation [132]. This premature cyclodehydrogenation produces

atomic hydrogen on the surface, which can directly compete with the polymerization reaction by forming a C-H bond at the radical termini of the growing polymer chain, thus inhibiting further radical addition. These findings suggest that for achieving longer GNRs the choice of the monomer and substrate should be optimized in order to suppress dehydrogenation during polymer growth. While preliminary studies of the polymerization under increased hydrogen partial pressure seem to confirm this picture [144], the role of molecular and atomic hydrogen deserves further investigation.

CHAPTER 4

Dependence of the band gap on ribbon length and termination

4.1 Quantum confinement due to finite length

Most experimental studies of the electronic structure of atomically precise graphene nanoribbons have so far focussed on the effect of quantum confinement due to the narrow *width* of the GNRs [145, 21, 146, 147]. It is therefore implicitly assumed that the GNRs under investigation are long enough that their finite *length* does not play a role. Particularly in the context of experimental techniques that average over the properties of many individual nanoribbons, such as photoemission spectroscopy, this raises the question: *How long is long enough?* More specifically, how does the electronic structure evolve from a molecule to the nanoribbon? This problem is not only of academic interest, since the finite length of GNRs may well become relevant in possible future applications in nanoscale devices.

The answer to these questions naturally depends on the physical quantities that are investigated and the accuracy that is desired. Hod and coworkers have analyzed the density of states (DOS) of finite $M = 9, 11$ and 13 AGNRs [148] using the HSE06 hybrid density functional [149, 150]. From a comparison of the DOS for GNRs of different lengths, they conclude that the main qualitative features of the bulk electronic structure are recovered only at lengths $\gtrsim 40\,\mathrm{nm}$. This conclusion, however, depends on the assumed level broadening for the finite structures, which was chosen to be of Lorentzian form with $\Gamma = 10\,\mathrm{meV}$ width.

The experiments discussed in this chapter probe the electronic structure of short bottom-up fabricated 7-AGNRs adsorbed on Au(111) via scanning tunneling spectroscopy. Using this technique, the level broadening is found to be about one order of magnitude larger than the one assumed by Hod and coworkers.[1] In order to focus on a simple and technologically relevant figure of merit, the discussion is restricted to the band gap Δ instead of the DOS. Since the GNRs are synthesized with atomic precision, the experimental findings reflect intrinsic properties of the class of GNRs under study and enable direct comparison with tight binding and density functional theory calculations. In this context, particular attention is given to the role played by the two possible terminations of the GNR, as discussed in chapter 3.

4.2 Experimental background

Figure 4.1 shows a 7-AGNR imaged by non-contact atomic force microscopy and scanning tunneling microscopy. While the long edges of the 7-AGNR are monohydrogenated, the GNRs may be terminated by one hydrogen at the central carbon atom (CH, left terminus) or by two hydrogen atoms (CH_2, right terminus), depending on the temperature T_c chosen for the dehydrogenation step [22, 132, 143]. By varying T_c from 300° to 400°, the relative probability

[1] See reference [151] and chapter 5.

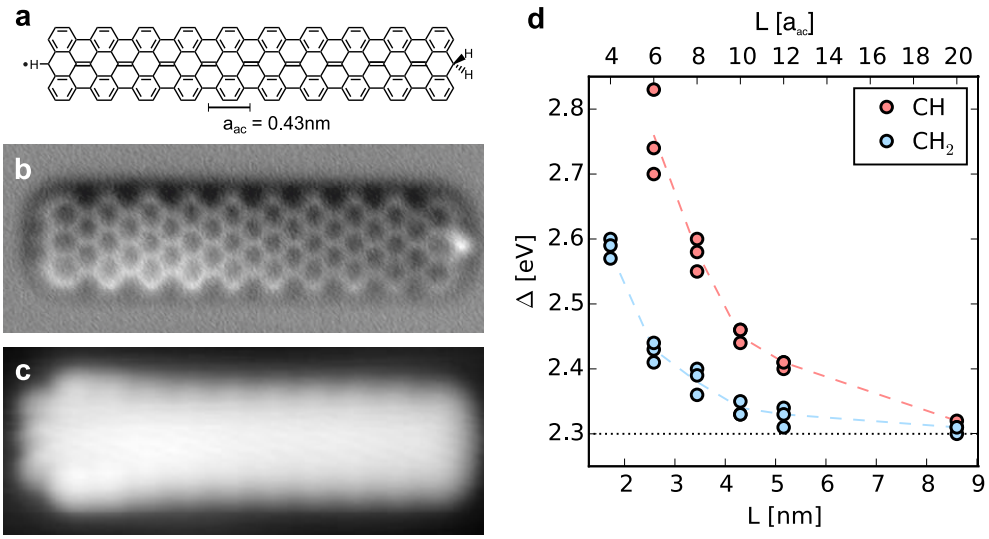

Figure 4.1: Short 7-AGNRs on Au(111). (a) Scheme of 7-AGNR consisting of 10 anthene units with length $L \approx 10a_{ac} = 4.3\,\text{nm}$. (b) Non-contact AFM image ($A = 43\,\text{pm}, f = 23\,\text{kHz}$). (c) Constant-current STM image ($U = 0.2\,\text{V}, I = 10\,\text{pA}$). (d) Band gap of 7-AGNRs with CH and CH_2 termination (at both ends), determined by STS as a function of GNR length. The dashed lines follow the averaged values for each length. The dotted line marks the bulk value. Data sets (b-c) were recorded by Shigeki Kawai, (d) by Hajo Söde.

of CH and CH_2-termination can be tuned from a majority of CH_2 to almost exclusively CH. Unless otherwise stated, in the following only GNRs with the same termination at both ends are considered. Length and termination of the GNRs can be identified not only by AFM, but also by high-resolution STM [132, 143]. As illustrated by Figure 4.1 (c), the CH terminus is associated with an in-gap edge-localized state, which is absent at the CH_2 terminus (see chapter 3 for details).

The band gap of finite 7-AGNRs on Au(111) was determined using scanning tunneling spectroscopy (STS). The STM tip was positioned in the center between the two termini and, following reference [21], the band gap was extracted using the half-maximum of the valence and conduction band onsets.

As shown in Figure 4.1 (d), the additional confinement due to decreasing length gives rise to an increase of the band gap, as expected. In the length range of $2 - 9\,\text{nm}$ investigated here, however, also the termination of the GNR plays an important role – a fact that was discovered only after comparison with tight binding and DFT calculations. For a GNR with length $L = 10\,a_{ac} \approx 4\,\text{nm}$, as shown in Figure 4.1 (a)-(c), adding a second hydrogen atom to the central carbon atom at the termini lowers the band gap by more than 0.1 eV. This might seem counterintuitive at first, since the hydrogen ad-

dition completely removes the carbon atom from participation in the π system, i.e. the size of the π system actually *decreases*. As discussed below, the experimental finding is, however, in agreement with tight binding and density functional theory calculations.

The following discussion requires a precise definition of the term *band gap*. In solid state physics, the band gap Δ of a periodic crystal is commonly defined as the energy difference between the top of the valence band and the bottom of the conduction band. For a finite crystal, the continuous energy bands become sets of discrete energy levels and the concept of the band gap is naturally carried over to denote the energy difference between the highest such energy emerging from the valence band and the lowest such energy emerging from the conduction band.

While the corresponding states remain delocalized over the crystal, the inevitable creation of surfaces can give rise to new, qualitatively different states that are localized exclusively near the surface[2] and whose energies may fall into the band gap Δ between delocalized states. As discussed below, this occurs in 7-AGNRs with CH termination, which exhibit Tamm states localized at the zigzag termini. In this particular system, both the highest occupied molecular orbital (HOMO) and the lowest unoccupied molecular orbital (LUMO) are surface states of the finite one-dimensional crystal. Their energetics are discussed in detail in chapter 6, but will not be considered further in the present chapter, which is concerned with the band gap Δ between *delocalized* states only.

Note that the definition of the band gap given above is appropriate in view of electronic transport applications, where states that are localized near the termini of the GNRs do not contribute to the current. It is also the quantity that is measured in scanning tunneling spectroscopy, when positioning the tip in the center between the two termini, as has been done in this study.

4.3 Clar's theory

In order to rationalize the experimental observations, it is helpful to start with some basic insights into the electronic structure of graphene nanoribbons provided by Clar's theory of the aromatic sextet.[3] Clar's rule states that the Clar structure of a hydrocarbon that has the highest number of aromatic sextets, termed Clar *formula*, is most representative of its π-electron distribution. Figure 4.2 (a) shows the Clar formula for the CH_2-terminated 7-AGNR. The Clar formula is unique and it contains two aromatic sextets per unit cell of the GNR. The case of CH-terminated 7-AGNRs is more complicated, as shown in

[2]When going to smaller and smaller crystal sizes, at some point the differentiation between surface states and delocalized states inevitably loses its meaning. As discussed below, however, this point is not reached in the GNR length range investigated here.

[3]See chapter 2.4.1 for an introduction to Clar's theory and its application to nanographenes.

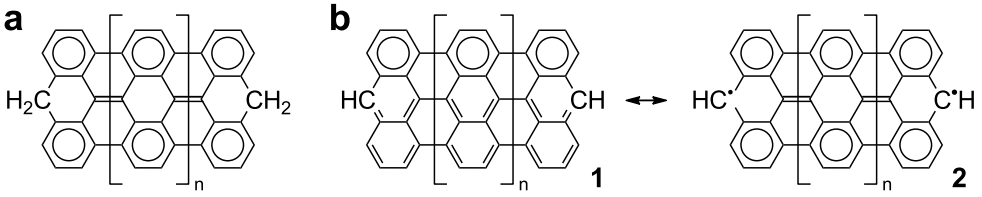

Figure 4.2: Clar formulas of finite 7-AGNRs. (a) Clar formula for CH_2 termination. (b) Clar formulas for CH termination. Adapted from original schemes by Akimitsu Narita (private communication).

Figure 4.2 (b). Multiple Clar formulae exist, but they have only one aromatic sextet per repeat unit, leading to a considerable reduction in aromatic stabilization compared to the CH_2 case. At the cost of introducing one unpaired electron near each terminus of the GNR, however, a unique Clar formula with two Clar sextets per repeat unit is obtained also in this case.

The electronic structure of CH-terminated 7-AGNRs is therefore characterized by a competition between the cost of breaking a π-bond at the terminus, favoring structure **1**, and the energetic stabilization due to increased aromaticity, favoring structure **2**. Since the aromatic stabilization increases linearly with GNR length, the question arises from which length onwards structure **2** will dominate. Konishi et al. have studied CH-terminated 7-AGNRs of lengths $L = 2a_{ac}, 3a_{ac}$ and $4a_{ac}$ using the complete active space self-consistent field (CASSCF) method, finding a biradical character of $7, 54$ and 91% [152]. This indicates that for the length range of $L \geq 4a_{ac}$ considered here, the biradical Clar formula **2** is dominant and the Tamm states near the CH termini have already developed.[4]

4.4 Tight binding

While this confirms that the CH-termination is associated with edge-localized states, it does not yet explain the influence of the termination on the band gap. A simple model that captures the effect on a qualitative level, is tight-binding using one π-orbital per carbon atom and considering hopping only between nearest neighbors.[5]

Figure 4.3 (a) shows the electronic band structure of the infinite 7-AGNR. For a hopping integral of $t = 3\,\mathrm{eV}$, a band gap of $\Delta \approx 1.41\,\mathrm{eV}$ is obtained. This may now be compared to the band gap of 7-AGNR with finite length L, which is defined in 4.3 (b). Figure 4.3 (c) demonstrates that tight binding

[4]Note that this also indicates that the application of single-determinantal methods, such as (approximative) unrestricted Kohn-Sham DFT, is justified here.

[5]See chapter 2.4.2 for an introduction to tight binding and its application to nanographenes.

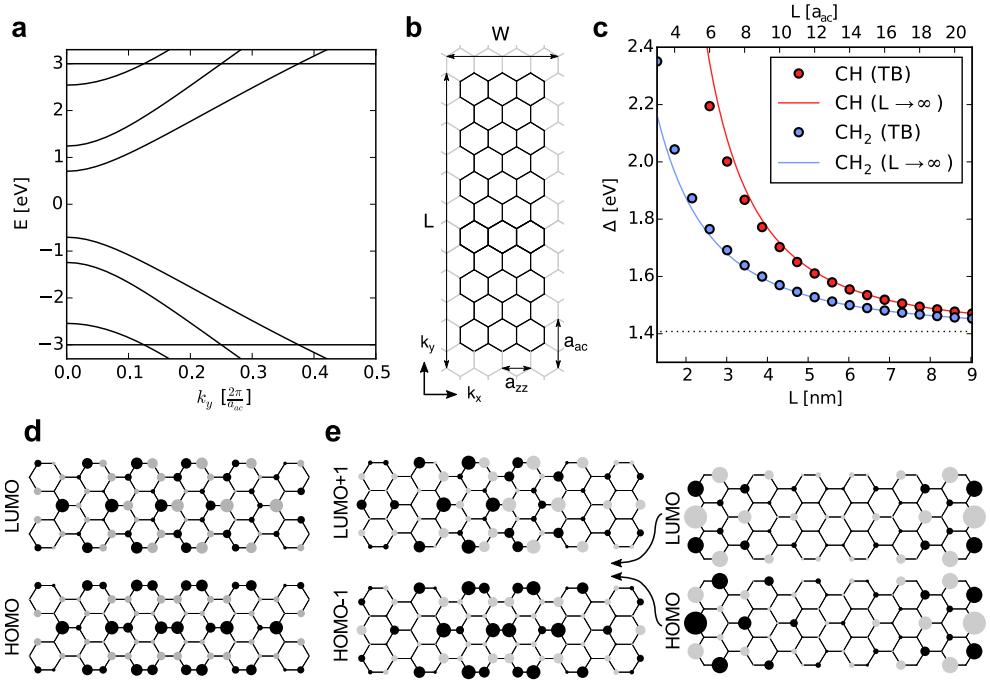

Figure 4.3: Tight binding description of 7-AGNRs. (a) Energy bands of 7-AGNR for hopping integral $t = 3\,\text{eV}$. (b) Definition of directions k_x and k_y as well as length L and width W. (c) Band gap as function of L and termination. The continuous lines are obtained from the asymptotic form for $L \to \infty$ according to equation (4.4). The dotted line indicates the bulk value of 1.41 eV. (d-e) Orbitals for 7-AGNR with length $L = 6a_{ac}$ with CH_2 (d) and CH (e) termination. The circle area is proportional to the electron density, gray/black indicates the sign of the wave function.

indeed reproduces the experimental finding: the band gaps of CH-terminated GNRs are found to be larger than those of CH_2-terminated GNRs of the same length. As will be discussed in section 4.5, the slower convergence of $\Delta(L)$ compared to experiment is related to the stronger dispersion of the frontier bands in tight binding.

Figure 4.3 (d) and (e) show the corresponding orbitals for a 7-AGNR of length $L = 6a_{ac}$. In case of the CH_2 termination, the central carbon atom at the terminus does not contribute an electron to the π-system. Within the tight binding description, the CH_2 termination is therefore equivalent to a so-called *cove defect*, where the central carbon atom is simply removed [153]. For the CH_2 termination, there are no edge states and the band gap equals the HOMO-LUMO gap. In case of the CH termination, one finds exactly one occupied and one empty Tamm state inside the band gap, as expected from the

fact that the short zigzag edge consists of exactly three zags.[6] Here, the band gap is given by the energy difference between the HOMO-1 and the LUMO+1.

Comparing the states at the band onsets for the CH_2 and CH-termination in detail, it appears that the CH states are slightly pushed away from the termini compared to their CH_2 counterparts. Stronger confinement would naturally lead to a larger band gap. In the following, this observation is put on a quantitative footing using the analytic expression for the energy levels of monohydrogenated armchair and zigzag GNRs derived by Wakabayashi [97].

As discussed in more detail in chapter 2.4.2, the delocalized states of finite armchair graphene nanoribbons with monohydrogenated edges can be related to the dispersion of graphene $E(\mathbf{k})$ (2.59), by finding a corresponding wave vector $\mathbf{k} = (k_x, k_y)$ with components k_x along the zigzag and k_y along the armchair direction. While confinement by the armchair edges gives rise to a simple discretization

$$k_x = r\frac{\pi}{W} = r\frac{2\pi}{(M+1)a_{zz}} \quad \text{with } r \in \{1, \ldots, M\} \quad , \tag{4.1}$$

confinement in between zigzag edges results in a transcendental equation for $k_y = k_y(k_x)$ [97]. In appendix A, this equation is expanded for large N and small k_y. For the valence and conduction bands of armchair GNRs in the semiconducting $M = 3m + 1$ family, it takes the simple form

$$k_y \approx s\frac{\pi}{L+\delta'} = s\frac{\pi}{(N+\delta)\frac{a_{ac}}{2}} \quad \text{with } s \in \{1, \ldots, N\},\ s \ll N, \tag{4.2}$$

$$\text{and} \quad \delta = \left[1 + 1/\left(2\cos\left[\frac{2m+1}{3m+2}\pi\right]\right)\right]^{-1} \leq 0 \tag{4.3}$$

Note that in the limit of large N considered here, δ is independent of the GNR length and depends only on the width of the GNR. The boundary conditions at the terminus may therefore be viewed as giving rise to an "effective electronic length" $L+\delta'$ that is *reduced* with respect to the geometric length L. Within tight binding, the ratio δ'/L can thus serve as another way of quantifying the deviation of the electronic structure of finite GNRs from the simplified picture of particles in a box.[7]

As shown in appendix A, the band gap is then given by

$$\Delta(L) = a + \frac{b}{(L+\delta')^2} + O\left(\frac{1}{(L+\delta')^4}\right) \quad \text{for } L \to \infty. \tag{4.4}$$

For 7-AGNRs ($m = 2$), one obtains $\delta' = \delta\frac{a_{ac}}{2} \approx -0.7\,\text{nm}$. Using a hopping integral $t = 3\,\text{eV}$, one further finds $a \approx 1.41\,\text{eV}$ and $b \approx 4.46\,\text{eVnm}^2$.

[6] See chapter 2.4.1.

[7] See also appendix B.

For the CH_2-terminated 7-AGNRs, where the analytic expressions of reference [97] do not apply, fitting equation (4.4) to numerical tight binding gaps of sufficiently long GNRs yields $\delta' \approx +0.9\,\mathrm{nm}$.

In comparison, the effective electronic length of CH_2-terminated 7-AGNRs is therefore $0.9+0.7 = 1.6\,\mathrm{nm}$ longer than the one of CH-terminated consisting of the same number of monomers.[8] Figure 4.3 (c) compares the exact tight binding gaps (markers) to those obtained using the "effective length" approximation (lines).

The above analysis is easily generalized to GNRs of other widths. As shown in appendix A, for (monohydrogenated) AGNRs of the semiconducting families $M = 3m$ and $M = 3m + 1$, the discrepancy between geometric and effective electronic length grows linearly with increasing GNR width, while it takes a generally different form for metallic AGNRs.

4.5 Density functional theory

While single-orbital nearest-neighbor tight binding lends itself to qualitative investigations, neglecting the variation of on-site energies, hopping between more than nearest neighbors and the Coulomb repulsion between electrons constitutes a serious simplification. In this respect, an *ab initio* scheme, such as density functional theory, presents a significant step forward. For the case of 7-AGNRs, it has been found that the effective single-particle description of spin-unrestricted Kohn-Sham DFT with a semi-local functional is able to capture the essential features when compared to a solution of the many-body Hubbard model [154].

Spin-unrestricted DFT calculations have been performed with the PBE generalized gradient approximation to the exchange-correlation functional [63]. The Quantum ESPRESSO package [155] was used, together with projector augmented-wave ultrasoft pseudopotentials from the `pslibrary.1.0.0` [156] and an energy cutoff of 46 Ry for the wave functions and 326 Ry for the charge density. Atomic positions were relaxed until the forces were below 10^{-4} Hartree atomic units. The band structure of the periodic 7-AGNR was calculated using 64 k-points in the first Brillouin zone. The band gaps of finite 7-AGNRs consisting of $4, 6, \ldots, 20$ anthene units were computed, both for CH and CH_2 termination.

The resulting Kohn-Sham gaps are shown in Figure 4.4 (b). The continuous lines are obtained from fitting $\Delta(L)$ against equation (4.4), while fixing $a = 1.57\,\mathrm{eV}$ to the value of the bulk band gap.[9] Similar to tight binding, one

[8] These statements refer to the valence and conduction band. See appendix A for how to compute δ' for other bands.

[9] The least-squares fit was performed in the range of $L \in [12a_{ac}, 20a_{ac}]$. The values with standard errors are $\delta' = -0.67 \pm 0.14\,\mathrm{nm}$, $b = 1.81 \pm 0.12\,\mathrm{nm}$ (CH) and $\delta' = +0.47 \pm 0.08\,\mathrm{nm}$, $b = 1.66 \pm 0.05\,\mathrm{nm}$ (CH_2).

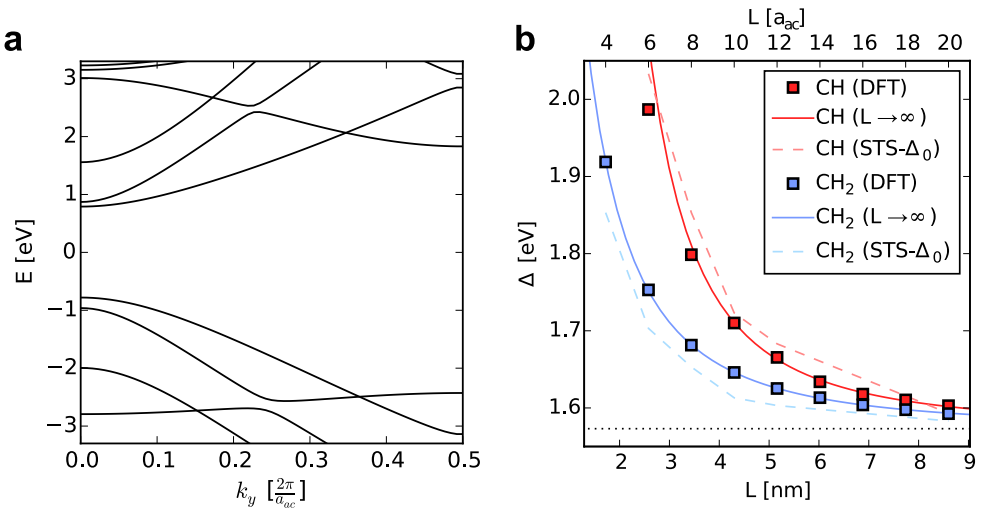

Figure 4.4: Electronic structure within DFT. (a) Band structure of the 7-AGNR. The center of the gap has been shifted to zero energy. (b) DFT band gap as function of length and termination. Continuous lines indicate fits to equation (4.4). Dashed lines indicate the experimental gaps shown in Figure 4.1 (d), reduced by a constant $\Delta_0 = 0.73\,\text{eV}$. The dotted line indicates the bulk value of 1.57 eV.

finds $\delta' \approx -0.7\,\text{nm}$ for the CH termination and $\delta' \approx +0.5\,\text{nm}$ for the CH_2 termination, while the values for b are significantly reduced due to the lower dispersion of the DFT band structure 4.4 (a) compared to tight binding.

Figure 4.4 (b) also shows the experimental band gaps obtained from STS (dashed lines). To aid the comparison, the experimental data have been reduced by a constant shift of

$$\Delta_0 = \Delta 2.3\,\text{eV} - 1.57\,\text{eV} = 0.73\,\text{eV} \quad , \tag{4.5}$$

letting both gaps agree in the limit of $L \to \infty$.

Kohn-Sham DFT with approximate semi-local exchange-correlation functionals is well-known to underestimate band gaps of molecules and bulk semiconductors. The size of this error will, in general, depend on the atomic structure of the system under investigation. Yet, Figure 4.4 (b) suggests that a constant shift by Δ_0 brings the Kohn-Sham gap of finite 7-AGNRs with different lengths and terminations into good agreement with experiment.

While there may be no general justification for applying such a constant shift, note that for the 7-AGNR the *dispersion* of the frontier electronic bands in DFT fits the experimentally determined dispersion rather well (see chapter 5). If the opening of the band gap in finite 7-AGNRs arises mainly through the corresponding discretization of the bulk frontier bands,[10] it then follows that

[10]Note that, on the experimental side, this may depend significantly on the screening

the difference Δ_0 between experimental and Kohn-Sham gap is independent of length.

Finally, a caveat concerning the Tamm states at CH termini, whose description is relevant here only as far as their influence on the *delocalized* states is concerned. As will be discussed in chapter 6, spin-unrestricted DFT predicts the empty and filled Tamm states of the 7-AGNR to be split in energy by $\Delta_{zz} \approx 0.5\,\text{eV}$, which is not observed in STS experiments of 7-AGNRs on Au(111) (see Figure 6.1). This finding has been explained by a transfer of electrons from the GNR to the Au substrate, noting that the splitting of the Tamm states is strongly reduced in DFT calculations of charged 7-AGNRs in vacuum [143, 154]. Emptying the Tamm states at both ends[11] would indeed affect the band gap between *delocalized* states as well (not shown). Yet, on the Au(111) substrate, any charge residing permanently on the 7-AGNRs is going to be screened by the nearby metal, thus casting doubt on the relevance of DFT calculations for charged, free-standing 7-AGNRs. We note, for example, that these calculations also predict the energy of the empty Tamm states to move down relative to the delocalized states, merging with the valence band onset for $L \to \infty$ (not shown). This is clearly not the case in experiment, where the onset of the valence band is found at $-0.8\,\text{eV}$ (conduction band onset at $+1.5\,\text{eV}$) [151]. Since the Fermi energy is, however, found *below the center* of the band gap, an intermediate scenario with a substrate-induced dipole may be at play.

4.6 Conclusions

The band gap of finite 7-AGNRs has been analyzed as a function of length and termination through a combination of scanning tunneling spectroscopy of atomically precise 7-AGNRs on Au(111) with tight binding and density functional theory investigations.

The band gap is found to be well described by the formula

$$\Delta(L) = a + \frac{b}{(L + \delta')^2} \tag{4.6}$$

where L denotes the geometric length defined by the carbon skeleton of the GNR and δ' is a shift that depends on the boundary condition at the terminus. In agreement between tight binding, DFT and experiment, δ' is found to be *negative*, when the central carbon atom at the terminus is passivated by a single hydrogen atom (CH termination), and *positive* when it is passivated by two hydrogen atoms (CH_2 termination).

from the underlying Au surface. For GNRs on insulators and, even more so, for free-standing GNRs, an appropriate treatment of many-body effects should become necessary – for example, within the *GW* approximation.

[11] Corresponding to a charge of $+2|e|$ for the finite 7-AGNR.

This gives rise to a larger band gap of short CH-terminated 7-AGNRs, when compared to CH_2-terminated 7-AGNRs of the same geometric length, illustrating the sensitivity of the π-electronic structure of GNRs even to single atomic defects.

CHAPTER 5

Band dispersion of graphene nanoribbons from scanning tunneling spectroscopy

5.1 Band dispersion and effective masses

The driving motivation for the fabrication of graphene nanoribbons is to open a band gap in graphene by quantum confinement in order to reduce off-currents in transistor applications. In this process, the high charge carrier mobility of graphene needs to be maintained, if high switching speeds are to be achieved. According to the semi-classical picture of electrical conduction, the mobility $\mu = e\tau/m^*$ depends on *two* factors: the relaxation time τ and the effective mass m^* of the charge carriers involved in the transport. Minimizing edge defects by atomically precise bottom-up fabrication aims at maintaining large relaxation times by reducing scattering of charge carriers, which has been shown to be particularly important for GNRs with armchair edges [157, 158]. At the same time, the effective masses should be as low as possible. In order to assess the potential of atomically precise graphene nanoribbons, it is therefore necessary to determine not only the band gap, but also the *dispersion* of their one-dimensional electronic bands near the Fermi energy.

Two early studies on the electronic dispersion of the $M = 7$ AGNR (7-AGNR) relied on angle-resolved photoemission spectroscopy (ARPES), a technique that can only probe occupied states, and averages over all GNRs in the spot of the photon beam. Through growth on the stepped Au(788) surface the GNRs were aligned along step edges, which enabled the determination of the dispersion along the GNR axis. However, the reported effective masses for the valence band of $m^*_{VB} \approx 0.21\, m_e$ [21] and $m^*_{VB} \approx 1.07\, m_e$ [145] differ by a factor of 5. A further study by angle-resolved two-photon photoemission (2PPE) spectroscopy reported $m^*_{VB} \approx 1.37\, m_e$ and $m^*_{CB} \approx 1.35\, m_e$ for the conduction band [146][1]. In view of this discrepancy, obtaining additional data through an independent experimental technique seemed highly desirable.

Scanning tunneling spectroscopy offers two main advantages in this respect: First, it allows to focus on individual GNRs, which can be checked for atomic precision and sufficient length. And second, STS is naturally able to probe both occupied and empty states, which is essential when characterizing GNRs for future electronic transport applications. The peculiarities related to probing the exponential tails of the wave function can be understood and addressed by comparison with *ab initio* simulations, as shown below.

This chapter discusses how to determine the dispersion of frontier bands[2] for the $M = 7$ and $M = 9$ armchair graphene nanoribbons via Fourier-transformed scanning tunneling spectroscopy. The experiments shown were performed by Hajo Söde on atomically precise bottom-up fabricated GNRs on Au(111). Experimental details can be found in references [151, 27].

[1] In this study, however, the connection of the experimental data to the one-dimensional dispersion along the GNR axis is less evident, since the GNRs under study were not aligned.

[2] Referring to occupied and empty bands close to the Fermi energy.

5.2 Predicted band structure

The electronic structure of graphene nanoribbons has already been studied extensively by different levels of theory, both empirical and *ab initio*. These include the tight binding model [96], density functional theory [88] and the *GW* approximation of many-body perturbation theory [159]. In the following, the electronic structure of 7- and 9-AGNRs is computed via these three methods, with particular focus on the dispersion of the two highest valence bands (VB-1, VB) and the two lowest conduction bands (CB, CB+1).

Density functional theory calculations with the PBE exchange-correlation functional [63] were performed using the Quantum ESPRESSO package [155], which expands the Kohn-Sham wave functions on a plane wave basis set with kinetic energy $E_{kin} \leq E_{cut}$. The simulation cell was chosen at least twice as large as the $10^{-5}/a_0^3$ isosurface of the electron density in order to enable the Coulomb-cutoff technique in subsequent *GW* calculations [160]. For geometry optimization, atomic positions were relaxed using norm-conserving pseudopotentials, $E_{cut} = 150\,\mathrm{Ry}$ and 16 k-points in the first Brillouin zone, until the forces acting on the atoms were below $3\,\mathrm{meV/Å}$. The lattice parameter a_{ac} was determined to be 4.285 Å for the 7-AGNR and 4.282 Å for the 9-AGNR. Following reference [161], band structures[3] were calculated using 64 k-points, reducing E_{cut} to 60 Ry in order to keep the computational cost of *GW* calculations manageable[4]. It was verified that the effect of the reduction in cutoff on the band structure was negligible.

Quasiparticle corrections were computed within the framework of many-body perturbation theory, using the G_0W_0 approximation to the self-energy as implemented in the BerkeleyGW package [81, 162]. Sufficient numbers of empty bands were included to cover the energy range up to 2.1 Ry above the highest occupied band. The static dielectric matrix ε was calculated in the random phase approximation with 8 Ry cutoff for the plane-wave basis. ε^{-1} was extended to the real frequency axis using the generalized plasmon-pole model by Hybertsen and Louie [81]. A rectangular Coulomb-cutoff was employed along the aperiodic dimensions as described in reference [160]. In the calculation of the self-energy, the static remainder approach was used to speed up the convergence with respect to the number of empty bands [163].

The resulting band structures are shown in Figures 5.1 and 5.2 and the effective masses of frontier bands have been documented in Tables 5.1 and 5.2.

The hopping integral $t = 3\,\mathrm{eV}$ chosen in tight binding is at the large end of the suggested range $2.5 - 3\,\mathrm{eV}$ (chapter 2.4.2), thus leading to a relatively strong dispersion. From comparison of the effective masses with DFT, however, it is evident that the single-parameter tight binding model is anyhow not

[3] In the DFT band structures shown in Figures 5.1 (b) and 5.2 (b), the vacuum level is close to +3 eV. Note that the bands near +3 eV with $m^* \approx 1$ originate from weakly bound electronic states that are not localized on the GNR.

[4] The computational complexity of inverting the dielectric matrix ε is $O(N_{pw}^3) = O(E_{cut}^{4.5})$.

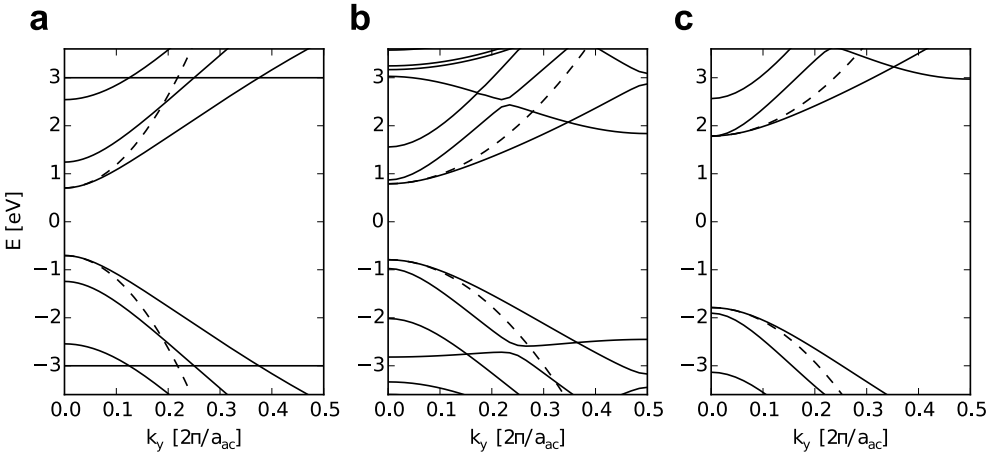

Figure 5.1: Band structure of the $M = 7$ AGNR. (a) Tight binding with $t = 3\,\text{eV}$. (b) DFT with PBE functional. (c) One-shot G_0W_0, starting from the DFT electronic structure. The center of the gap was set to zero energy in all cases. Dashed lines indicate parabolic fits with effective masses reported in Table 5.1.

Method	Δ [eV]	m^*_{VB-1}	m^*_{VB}	m^*_{CB}	m^*_{CB+1}
TB	1.41	0.16	0.17	0.17	0.16
DFT	1.58	0.15	0.34	0.42	0.14
G_0W_0	3.57	0.12	0.29	0.38	0.12

Table 5.1: Band gap and effective masses of frontier bands for $M = 7$ AGNR. For TB, analytical values are given. For DFT and GW, effective masses are obtained from a parabolic fit in the range $0 \leq k \leq \frac{1}{10}\frac{\pi}{a_{ac}}$.

Method	Δ [eV]	m^*_{VB-1}	m^*_{VB}	m^*_{CB}	m^*_{CB+1}
TB	1.05	0.34	0.08	0.08	0.34
DFT	0.8	0.71	0.09	0.09	1.48
G_0W_0	2.1	0.59	0.08	0.08	1.32

Table 5.2: Band gap and effective masses of frontier bands for $M = 9$ AGNR. For TB, analytical values are given. For DFT and GW, effective masses are obtained from a parabolic fit in the range $0 \leq k \leq \frac{1}{10}\frac{\pi}{a_{ac}}$.

flexible enough to fit the DFT band structure, since the latter breaks particle-hole symmetry and predicts higher effective masses for the CB and CB+1, compared to the VB and VB-1.

The same trend is found in the quasiparticle band structures computed withing the G_0W_0 approximation. Besides the substantial opening of the band gap, the dispersion of the quasiparticle band structure is increased by $\approx 10 -$

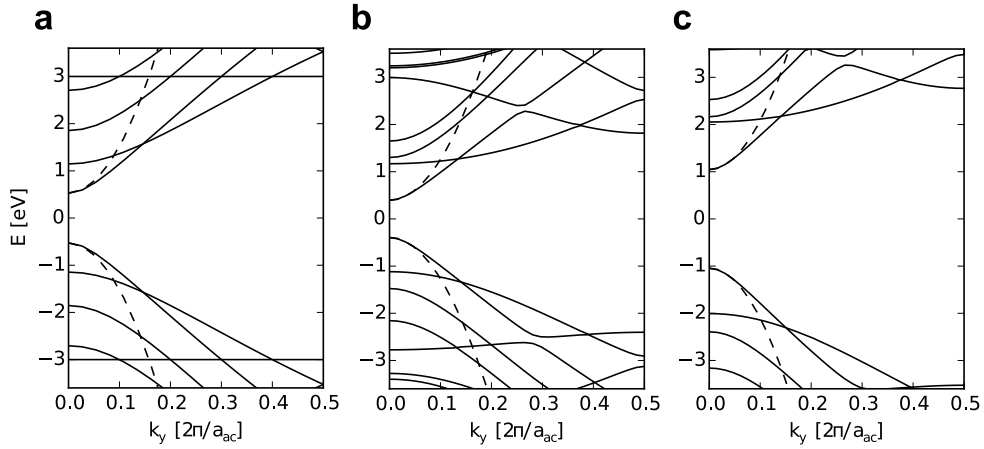

Figure 5.2: Band structure of the $M = 9$ AGNR. (a) Tight binding with $t = 3\,\text{eV}$. (b) DFT with PBE functional.(c) One-shot G_0W_0, starting from the DFT electronic structure. The center of the gap was set to zero energy in all cases. Dashed lines indicate parabolic fits with effective masses reported in Table 5.2.

20% with respect to DFT, similar to the effect of GW corrections in graphene [164]. Note also that for the 7-AGNR the G_0W_0 corrections lead to a close proximity of CB and CB+1 as well as of VB and VB+1 near the Γ point, while for the 9-AGNR, valence and conduction band remain well-separated from other bands.

In comparing the predicted band structures with experiment, it is important to note that the theoretical descriptions presented here describe isolated graphene nanoribbons, while experiments are performed on GNRs that are physisorbed on a metal surface. Up to the DFT level of theory,[5], including the substrate in the calculations has negligible effects on the band structure of the non-interacting[6] system [21]. The GW quasiparticle band structure, however, approximates the energies associated with the charged excitations of the system that occur during an STS experiment. The quasiparticle excitation energies depend on the screening properties of the surrounding medium and including the metal substrate in the calculation would therefore be highly desirable, particularly for obtaining accurate band gaps. Due to the computational complexity involved,[7] GW calculations of molecules adsorbed on surfaces have so far either been limited to small molecules and correspondingly small surface unit cells [165, 166, 167] and/or thin supporting substrates[168] or have

[5]With the generalized gradient approximation to the exchange-correlation functional.

[6]Non-interacting in the case of tight binding and interacting only through a local mean-field potential in the case of Kohn-Sham DFT.

[7]The computational complexity of GW calculations on plane-wave basis sets tends to scale with $O(N^3) - O(N^4)$, where N is the number of atoms in the system [162].

M	Δ [eV]	m^*_{VB-1}	m^*_{VB}	m^*_{CB}	m^*_{CB+1}
7	2.37 ± 0.06		0.41 ± 0.08	0.40 ± 0.18	0.20 ± 0.03
9	1.38 ± 0.02		0.12 ± 0.03	0.11 ± 0.03	

Table 5.3: Band gap and effective masses of frontier bands for 7- and 9-AGNR extracted from Fourier-transformed STS experiments on Au(111).

resorted to classical image charge models [169, 21].

For the 7-AGNR on Au(111), the image charge model has been shown to yield a reduction of the *GW* band gap of the isolated GNR by more than 1 eV to $\Delta = 2.3 - 2.7\,\text{eV}$ [21]. This is important to keep in mind in the following discussion, which will, however, focus mainly on the *dispersion* of the bands. The effect of screening on the dispersion is assumed to be relatively minor and not modeled explicitly here.

5.3 Scanning tunneling spectroscopy experiments

The physical quantity measured in STS is the derivative $\mathrm{d}I/\mathrm{d}V$ of the tunneling current I with respect to the sample bias V. In the Tersoff-Hamann approximation, the $\mathrm{d}I/\mathrm{d}V$ signal is directly proportional to the local density of states (LDOS). More precisely, $\mathrm{d}I/\mathrm{d}V(V, \mathbf{r})$ at sample bias V and tip position $\mathbf{r}$ is proportional to the LDOS $\rho(E, \mathbf{r})$ at energy $E = E_F + |e|V$, where E_F denotes the Fermi energy. By scanning the tip along the GNR and recording the $\mathrm{d}I/\mathrm{d}V$ signal as a function of bias voltage, one therefore obtains maps of the local density of states, as shown in Figure 5.3 (a) for the unoccupied states of the 7-AGNR.

In a perfect crystal, the electronic Bloch wave functions in neighboring unit cells differ only by a phase factor, resulting in a local density of states that shares the periodicity of the underlying lattice.[8] Defects, however, lead to scattering of Bloch waves, which gives rise to interference patterns with characteristic wave vectors. By mapping out these standing waves in the LDOS as a function of position and sample bias, STS can be used to reconstruct the energy-momentum relation for both occupied and empty electronic states [170, 171]. Systems studied so far by this approach include defects in graphene [172], carbon nanotubes [173] and high-T_c superconductors [174], but also the ends of carbon nanotubes [175] as well as short polyphenylene chains [176, 177].

In a first step, standing wave patterns in the LDOS are recorded by scanning along the axis of the GNRs, as shown in Figures 5.3 and 5.4 (a), (c). Then, a discrete Fourier transform $\rho(E, x) \to \hat{\rho}(E, q)$ is performed, where

$$\hat{\rho}\left(|e|V, \frac{2\pi n}{N\delta x}\right) \propto \sum_{m=0}^{N-1} \frac{dI}{dV}(V, m\delta x) \exp\left(i\frac{2\pi n}{N}m\right), \tag{5.1}$$

[8] At least in the absence of symmetry breaking, e.g., due to charge density waves.

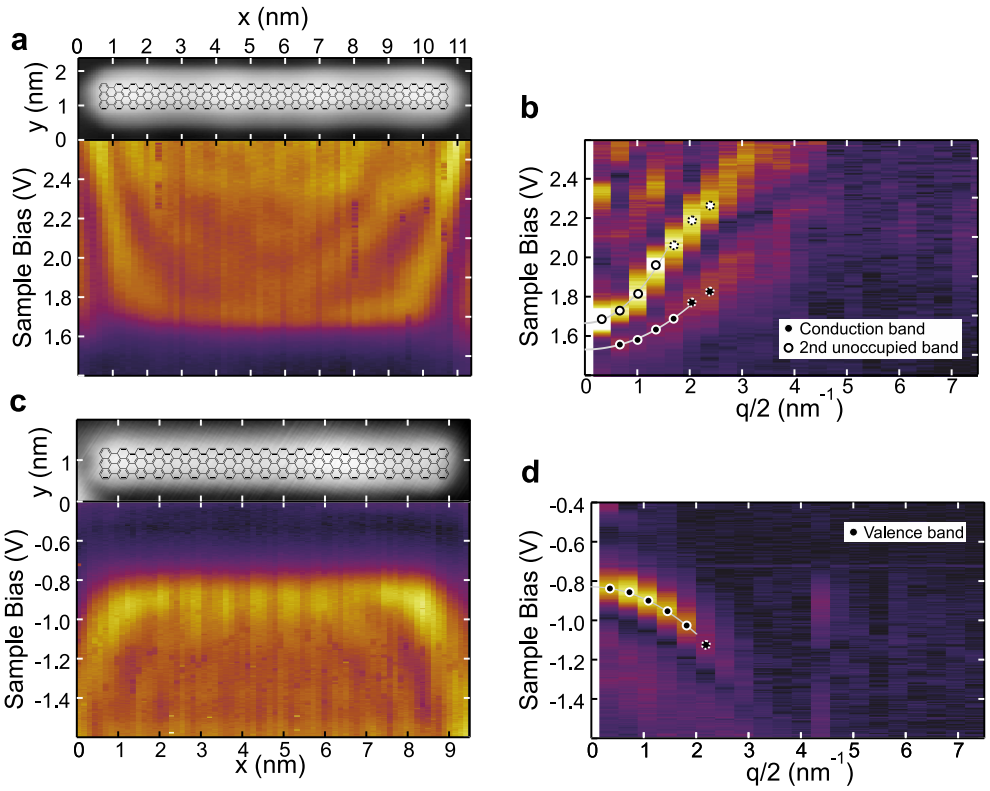

Figure 5.3: STS of 7-AGNRs on Au(111). (a) STM image and equidistant $\mathrm{d}I/\mathrm{d}V(V)$ spectra of unoccupied states, recorded along the edge of a 7-AGNR of length $24a_{ac}$ (set point $V = 2.7$ V, $I = 0.6$ nA, spacing $\delta x = 0.11$ nm). (b) Line-by-line Fourier transform of (a), showing the range $0 \leq \frac{q}{2} \leq \frac{\pi}{a_{ac}}$, including parabolic fit near $q/2 = 0$. (c) Analogous STM and $\mathrm{d}I/\mathrm{d}V(V)$ data for the occupied states, recorded along the edge of a 7-AGNR of length $20a_{ac}$ (set point $V = -1.6$ V, $I = 0.3$ nA, spacing $\delta x = 0.12$ nm). (d) Line-by-line Fourier transform of (c). Data recorded by Hajo Söde.

with the number of spectra N.

From the Fourier-transformed LDOS $|\hat{\rho}(E, q)|$ (FT-LDOS), plotted in Figures 5.3 and 5.4 (b), (d) as a function of $k = q/2$, the band dispersion of occupied and unoccupied states can then be extracted by following the intensity maxima as a function of k. Note that this approach involves the selection of a real-space window of length $L = N\delta x$, defining the spacing $\delta q = \frac{2\pi}{L}$ of the reciprocal grid. The choice of the grid affects the Fourier transform to a certain extent and the resulting uncertainty in the band masses is incorporated into the error bars. A brief discussion of this aspect is given in appendix B.

The direct comparison of the FT-LDOS with the predicted band structure is not straightforward. In the FT-LDOS of the empty states for the 7-AGNR,

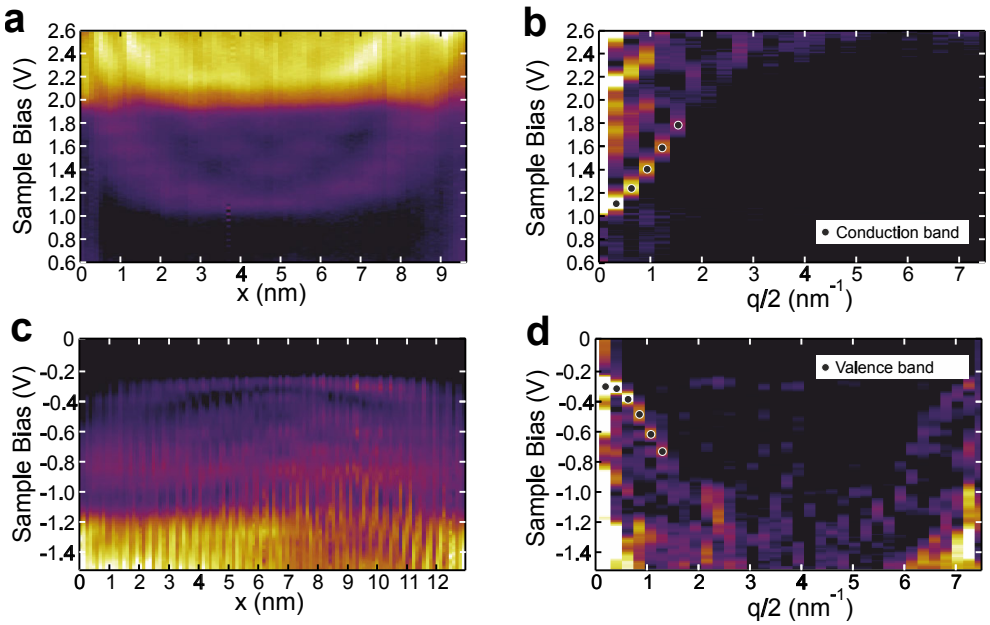

Figure 5.4: STS of 9-AGNRs on Au(111). (a) Equidistant dI/d$V(V)$ spectra of unoccupied states, recorded along a segment of $23a_{ac}$ length between two defects (b) Line-by-line Fourier-transform of (a) in the range $0 \leq q/2 \leq \pi/a_{ac}$. (set point $V = 2.5$ V, $I = 0.8$ nA). (c) Analogous dI/d$V(V)$ spectra of the unoccupied states, recorded along a segment of $30a_{ac}$ length between a terminus and a defect (set point $V = -1.5$ V, $I = 10$ nA). (d) Line-by-line Fourier-transform of (c). Data recorded by Hajo Söde.

shown in Figure 5.3 (b), the CB appears much fainter than the CB+1, and its signal further loses intensity towards $q/2 = 0$. In the FT-LDOS of the occupied states (Figure 5.3 (d)) only one valence band is detected, although theory predicts a second valence band close by. In the following, these observations are rationalized by studying the shape of the corresponding electronic orbitals.

5.4 Local density of states at realistic tip-sample distances

While the exact distance between tip and surface atoms is not directly accessible in STM experiments, in normal operation it is chosen *at least* large enough to avoid the formation of chemical bonds, which gives rise to a lower limit in the range of $2 - 3$ Å.[9] According to the Tersoff-Hamann approximation, it

[9] See references [178, 179] for investigations of the tunneling current and force on the tip as a function of the tip-sample separation.

is therefore the local density of states at significant distance from the sample that determines the $\mathrm{d}I/\mathrm{d}V$ signal in scanning tunneling spectroscopy.

To this aim, we have performed DFT calculations of finite $M = 7$ and $M = 9$ AGNRs in vacuum using the PBE generalized gradient approximation to the exchange-correlation functional [63]. The structures with lengths close to the experimentally investigated ones were relaxed until the forces acting on the atoms were below 3 meV/Å. We have used the CP2K code [136], which expands the wave functions on an atom-centered Gaussian-type basis set. After extrapolating the electronic states into the vacuum region as described in section 2.5.3, STS simulations were performed in the Tersoff-Hamann approximation on a plane parallel to the planar GNR, using a Lorentzian or Gaussian broadening of full-width 150 meV at half-maximum.

Figure 5.5 shows the Kohn-Sham orbitals of a finite 7-AGNR at the respective band onsets. The orbitals have been evaluated once on a plane 0.1 nm above the GNR, corresponding to a very short tip-sample distance (a), and once at a more realistic distance of 0.4 nm (b). As explained in appendix C.1, the effect of increasing tip-sample distance by Δz is approximately that of a Gaussian filter with standard deviation $\sigma = \sqrt{\Delta z/k_\nu}$ that smears out positive and negative regions of the wave function.[10] While the orbitals arising from the CB and the VB-1 oscillate strongly both along and perpendicular to the ribbon axis, the orbitals arising from the VB and CB+1 change sign only in the direction perpendicular to the ribbon axis. This leads to a lack of cancellation for the VB and CB+1 orbitals at the armchair edge. As a consequence, the CB and VB-1 are strongly suppressed with increasing tip-sample distance, while the VB and CB+1 give rise to a significantly larger, edge-localized LDOS.

The concentration of STS intensity near armchair edges has been observed in several previous experimental works [21, 134] and has recently been interpreted as arising from a difference in the local (Kohn-Sham) potential between the edge and the center of the GNR [180]. While variations in the potential certainly exist, we note here that they are not responsible for the edge-concentration of the LDOS with increasing tip-sample distance. This can be deduced from the fact that the features shown in Figure 5.5 (a) and (b) are qualitatively reproduced even by a nearest-neighbor tight-binding model[11] [181], where the potential is constant everywhere. Furthermore, a mechanism governed by the potential would imply a similar effect on all orbitals, which is evidently not the case.

We now follow the same procedure as in experiment, by first calculating the LDOS along the 7-AGNR (c-d) and then taking its Fourier transform (e-f). In Figure 5.5 (e), corresponding to 0.1 nm tip-sample distance, all band

[10] The constant $k_\nu = \sqrt{\frac{2m}{\hbar^2}|E_\nu - V_0|}$ depends only on the energy E_ν of the corresponding orbital with respect to the vacuum level V_0.

[11] The wave function in real space is obtained by placing a $2p_z$ orbital on each carbon site.

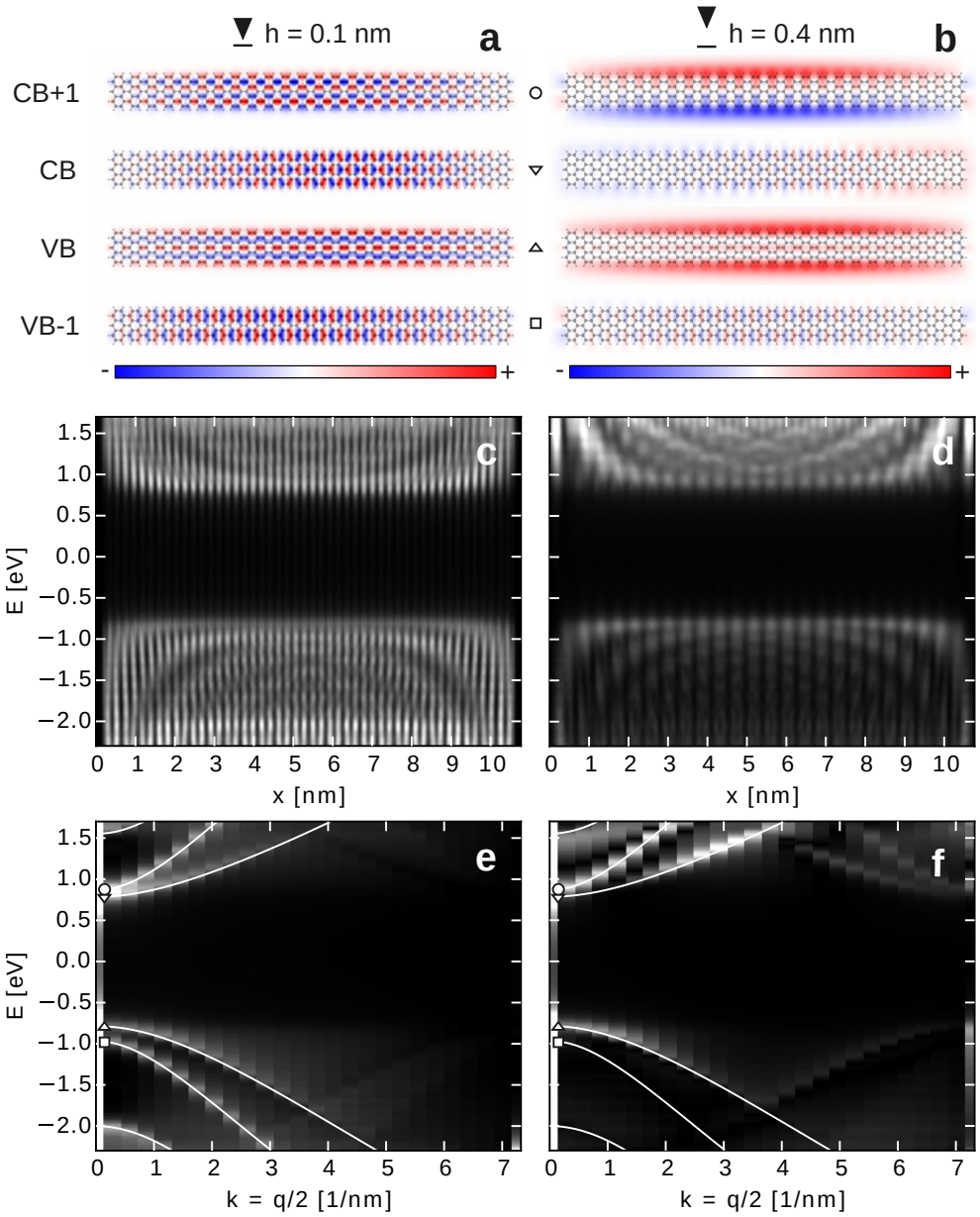

Figure 5.5: Effect of tip-sample distance on probed LDOS. (a, b) Kohn-Sham orbitals at the band onsets for a 7-AGNR of length $24a$ evaluated 0.1 nm (a) and 0.4 nm (b) above the GNR. (c, d) LDOS along the 7-AGNR, integrated across the ribbon (Lorentzian broadening, 150 meV FWHM). (e,f) FT-LDOS for $0 \leq k \leq \frac{\pi}{a_{ac}}$ with bands of infinite 7-AGNR superposed as white lines. The center of the gap is set to $E = 0$ in all cases.

onsets can be clearly determined from the FT-LDOS. In Figure 5.5 (f) at 0.4 nm distance, however, the VB-1 and VB-2 are missing completely and the intensity due to the CB is strongly reduced at low k values. This explains, why the experimental data in Figure 5.3 shows only *one* bright band in the occupied states and the unoccupied states each, despite the fact that two close-by bands are expected from theory. In agreement with the FT-STS simulation in Figure 5.5 (f), a faint signal is detected for the CB that loses intensity towards $k = 0$. By comparison with Fig. 5.5 (d,f) we can therefore confidently label the experimentally resolved bands as the VB, CB and CB+1.

Figure 5.6 shows analogous results for the 9-AGNR. Here, the band onsets of conduction and valence bands are well-isolated from other bands, which simplifies the analysis. Contrary to the 7-AGNR, it is the *valence* band, which loses intensity at elevated tip-sample distance relative to the conduction band. Based on this knowledge, the STS experiments probing the occupied states of the 9-AGNR, shown in Figure 5.4 (c), were performed at strongly reduced tip-sample distance,[12] which enabled the detection of the valence band.

M	VB-1	VB	CB	CB+1
3	+/+	+/−	+/+	+/−
4	+/−	+/+	+/−	+/+
5	+/−	∗	∗	+/+
6	+/+	+/−	+/+	+/−
7	+/−	+/+	+/−	+/+
8	+/−	∗	∗	+/+
9	+/+	+/−	+/+	+/−
10	+/−	+/+	+/−	+/+
11	+/−	∗	∗	+/+
12	+/+	+/−	+/+	+/−
13	+/−	+/+	+/−	+/+
14	+/−	∗	∗	+/+

Table 5.4: Symmetry of frontier bands of armchair GNRs at $k_x = 0$. Bands designated with +/− change sign along the GNR axis, while bands designated with +/+ do not (leading to an enhanced LDOS near their edges for large tip-sample distances). The special case of metallic bands is designated by a ∗.

Insofar as the edge-concentration and strength of the STS signal is determined by the symmetry of the contributing wave function, it can also be predicted by the tight binding model. In appendix C.2, a simple formula is derived to address the question, whether the wave function at the band onset of a given band will change sign along the GNR or not. Table 5.4 lists the results for the two highest occupied bands and the two lowest unoccupied

[12] Corresponding to an increase of the set-point for the tunneling current from 0.8 nA to 10nA.

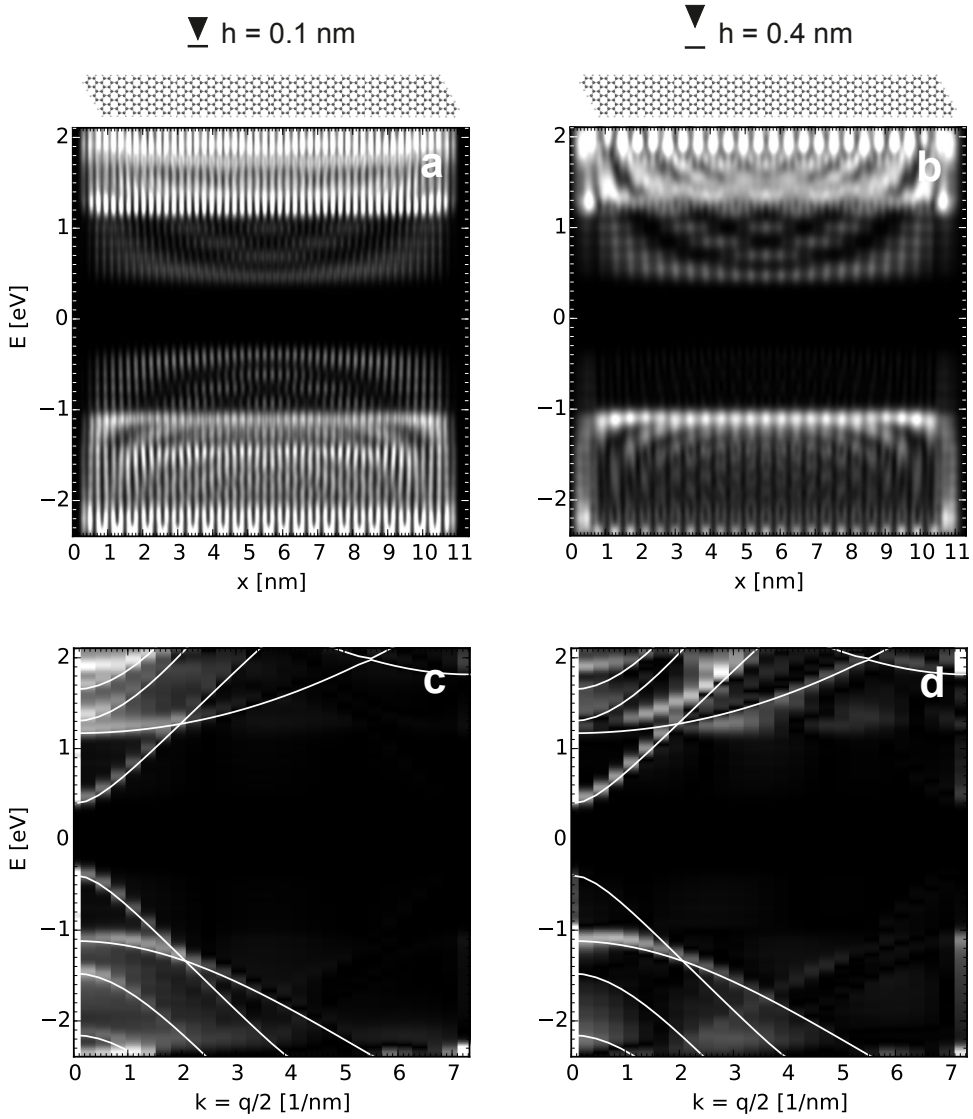

Figure 5.6: Effect of tip-sample distance on probed LDOS. (a, b) LDOS of a 9-AGNR of length $24a_{ac}$, evaluated at 0.1 nm (a) and 0.4 nm (b) above the GNR and integrated across the GNR (Gaussian broadening, 150 meV FWHM). (e, f) FT-LDOS for $0 \leq k \leq \frac{\pi}{a_{ac}}$ with bands of infinite 9-AGNR superposed as white lines. The center of the gap is set to $E = 0$ in all cases.

bands of armchair GNRs with widths ranging from $M = 3$ to $M = 14$. $+/-$ indicates an alternation of sign and $+/+$ indicates no change of sign. Note that the AGNRs in the $M = 3m - 1$ family are metallic in tight binding [97] and semiconducting in DFT [88] and *GW* [161]. The valence and conduction bands of the $M = 3m - 1$ family $(*)$ thus call for a special treatment, which

is not attempted here (see also appendix C.2).

5.5 Determining the band gap

These findings have implications not only for determining the dispersion of bands, but also for the extraction of band gaps from STS. In the $M = 3m$ family of AGNRs, the signal from the valence band is strongly suppressed at the band onset (in the $M = 3m+1$ family, this holds for the conduction band). In standard STS experiments without momentum resolution, these bands can be overshadowed by signal from nearby bands or even missed completely, resulting in an overestimation of the band gap. For example, a band gap of 2.8 eV has been reported for the recently synthesized 5-AGNR on Au(111) [182], despite the fact that *GW* calculations for free-standing, unscreened 5-AGNRs predict a band gap of only $\approx$ 1.7 eV [161]. The above analysis suggests that such issues can be clarified by performing STS at reduced tip-sample distances, if the GNRs are stable enough to support them.

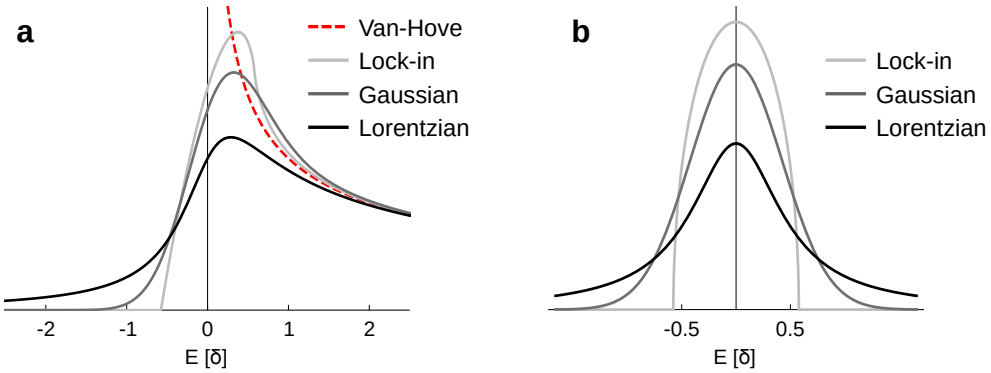

Figure 5.7: Broadening of the density of states. (a) $1/\sqrt{E}$ Van-Hove singularity (red) with Lock-in, Gaussian and Lorentzian broadening. The broadening functions shown in (b) are normalized and have full-width δ at half-maximum.

But even when the signals are sufficiently strong, the momentum resolution provided by FT-STS can be very helpful in pinning down the band onset more accurately. The DOS of a one-dimensional system diverges like $1/\sqrt{E}$ for a band onset at $E = 0$. Figure 5.7 shows such a van-Hove singularity and its convolution with common types of broadening functions (mathematical details in appendix D). Lock-in broadening arises from the finite modulation amplitude of the lock-in amplifier used to detect the derivative dI/dV.[13] Coupling between the adsorbate and the metal substrate introduces a life-time broadening, which can be modeled by a convolution with a Lorentzian function of

[13] With a peak-to-peak modulation of $\approx$ 56 meV, this is not the primary source of broadening in this work.

appropriate width. Contrary to the case of carbon nanotubes, which exhibit a weaker overall coupling with the substrate [183], this broadening can be of the order of 100 meV for GNRs and different recipes have been used in the literature to extract band gaps: For example, concerning the 7-AGNR, Chen et al. [147] report the peak-to-peak distance ($\Delta = 2.5$ eV), while Ruffieux et al. [21] report the distance between half maxima ($\Delta = 2.3$ eV).

As illustrated by Figure 5.7 (a), for purely Lorentzian broadening, the actual band onset lies in between half-maximum and maximum (see appendix D for details). But the exact shape of a spectrum is influenced by other factors, such as the energy-dependence of the spatial extension of the electronic orbitals as well as the energy-dependence of the life-times [184]. FT-STS circumvents the problem of having to extract band onsets from a spectrum of complicated shape: the momentum-resolved DOS at finite wave vectors shows peaks with well-defined maxima, allowing for a straightforward extrapolation towards $k = 0$. Using this method, band gaps of $\Delta = 2.37 \pm 0.06$ eV and $\Delta = 1.38 \pm 0.02$ eV eV are determined for the 7-AGNR and 9-AGNR on Au(111), respectively.

5.6 Conclusions and outlook

Scanning tunneling spectroscopy offers direct access to both occupied and empty electronic states of GNRs adsorbed on metal surfaces. Being a highly local probe, it allows to select individual GNRs with desired characteristics, such as lack of defects, atomic structure at the termini and sufficient length. These qualities make it a powerful tool for the investigation of the electronic structure of GNRs near to the Fermi level.

Yet, STS can only probe the exponential tails of the GNR wave functions and care must be taken when interpreting the recorded spectra. The theoretical analysis performed here explains the edge-concentration of STS intensity observed in previous experimental works and predicts the relative strength of STS signals from different bands based on intuitive symmetry arguments. *Ab initio* STS simulations on finite GNRs based on DFT illustrate the validity of the Fourier-transform approach and provide essential guidance for the proper identification of bands in the experimental spectra.

We are confident that the conclusions drawn in this work will generally be useful in characterizing the electronic structure of armchair GNRs by scanning tunneling spectroscopy, besides the cases of the $M = 7$ and $M = 9$ AGNR that have been discussed here.

CHAPTER 6

Edge state splitting at a short graphene zigzag edge

6.1 Metal-adsorbed graphene zigzag edges

Chapters 4 and 5 have been concerned with the electronic structure of bottom-up fabricated armchair graphene nanoribbons adsorbed on the Au(111) surface, where they are synthesized. While the energies associated with charged excitations of the GNRs are clearly affected by the polarization response of the nearby metal, the GNRs were treated as separate electronic subsystems – in other words, *hybridization* with the substrate was assumed to be negligible. For armchair GNRs, this picture of weak hybridization and a lack of charge transfer is supported both by experimental indications[1] and DFT calculations [21, 185].

Zigzag edges host localized states with energies close to the Fermi level, which have attracted particular attention from physicists, since they are predicted to be spin-polarized by many different levels of theory [88, 159, 109, 186]. Their interaction with a metal substrate requires separate investigation. A recent DFT study suggests that hybridization between monohydrogenated zigzag edges and the Au(111) surface is weak, showing no significant charge transfer and no significant effect on edge magnetization[2] [187]. However, an accurate description of this system within DFT is highly challenging, both due to the well-known problems of local- and semilocal functionals in describing charge transfer [188] and due to the necessity of incorporating dispersion forces in order to obtain accurate adsorption geometries. The widely used dispersion corrections based on interatomic pair potentials[3] [189, 68] need to be damped at short atomic distances. The damping function is typically chosen *ad hoc* and it has been shown that binding geometries can depend sensitively on the details of the (unphysical) damping function [71]. This is particularly problematic in the intermediate regime between physisorption (dominated by dispersion forces) and chemisorption (dominated by chemical bonds) that is of interest here.

So far, the bottom-up synthesis of GNRs with zigzag edges has not been reported. We note, however, that the 7-AGNR terminates in a short monohydrogenated zigzag edge (see Figure 6.1 (b)). Each terminus is predicted to host exactly one occupied and one empty localized state and their *orbital shape* determined by STM experiments is in excellent agreement with theoretical predictions for free-standing 7-AGNRs, as demonstrated in chapter 3. Yet, this agreement does not extend to the *energetics*. As will be detailed below, both DFT and *GW* predict a significant energy splitting Δ_{zz} between an occupied and an empty edge state, while STS experiments for 7-AGNRs on Au(111) find edge states only close to the Fermi level. This is illustrated

[1] Significant charge transfer can be excluded from the fact that the Fermi energy is located far within the gap between valence and conduction bands.

[2] While interaction with Ag(111) and Cu(111) is found to suppress edge magnetism.

[3] Reference [187] employs DFT-D2 [189] with dispersion coefficients fitted against results from the "van-der-Waals" density functional [72].

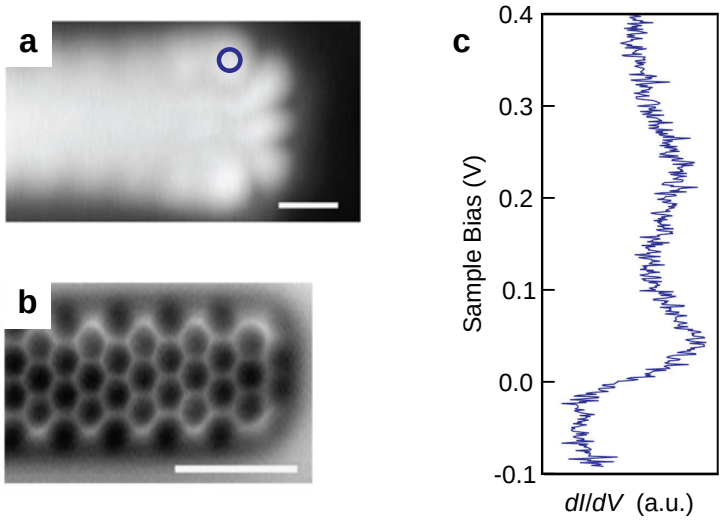

Figure 6.1: Scanning tunneling spectroscopy of CH-terminated 7-AGNRs on Au(111) [143]. (a) Constant-current STM image acquired with CO tip ($U = 0.01$ V, $I = 2$ pA, scale bar 0.5 nm) [143]. (b) Constant-height non-contact AFM image acquired with CO tip (scale bar 1 nm). (c) Scanning tunneling spectrum acquired with metal tip at terminus as indicated in (a). Figure adapted with permission from Macmillan Publishers Ltd: reference [143], Copyright (2013).

in Figure 6.1 using data by van der Lit and coworkers, who rationalize this finding in terms of hole-doping of the GNR [143, 154].[4]

This chapter compares the values for the edge state splitting Δ_{zz} of free-standing 7-AGNRs between different levels of theory and concludes with a discussion of recent experiments testing the electronic decoupling of 7-AGNRs from the Au(111) surface by a monolayer of NaCl [190].

6.2 Tight binding

Figure 6.2 (a) shows the tight binding band structure of graphene, projected onto the zigzag direction. The solid black line corresponds to the non-bonding, zero-energy states that are found to be localized at the zigzag edge of a semi-infinite graphene sheet. An example of such an edge state is sketched in Figure 6.2 (b). The edge states ψ_k live exclusively on the carbon sublattice that includes the outermost carbon sites and their degree of localization is determined by the wave vector k along the zigzag direction (see [97] for their analytical form).

[4]For details of the model, which includes the excitation of vibronic resonances, see reference [143].

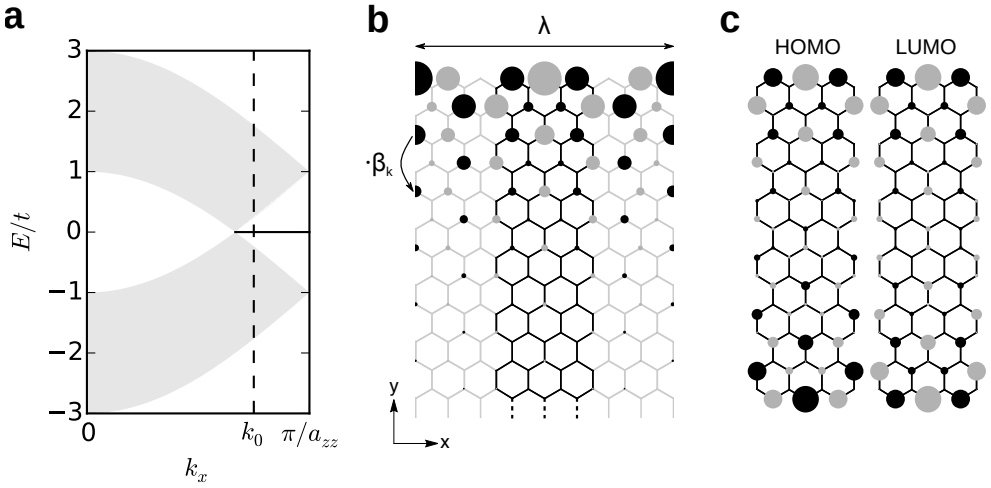

Figure 6.2: Edge states in tight binding. (a) Band structure of graphene projected onto the zigzag direction. The solid black line corresponds to the states localized at the zigzag edge of a semi-infinite graphene sheet. $k_0 = 0.75\frac{\pi}{a_{zz}}$. (b) Semi-infinite graphene sheet and linear combination of Bloch waves with wavelength $\lambda = 8a_{zz}$, satisfying the boundary conditions for the $M = 7$ AGNR. The circle area is proportional to the electron density, while gray/black indicates the sign of the wave function. (c) HOMO and LUMO of $M = 7$ AGNR with finite length $L = Na_{ac}/2$, where $N = 12$ is the number of zigzag lines.

More precisely, ψ_k decays along y by a factor of $\beta_k = (2\cos(\frac{ka_{zz}}{2}))^2$ from one armchair unit cell to the next [97], ranging from complete delocalization for $k = \frac{\pi}{a_{zz}}\frac{2}{3}$ ($\beta_k = 1$) to complete localization at the zigzag edge for $k = \frac{\pi}{a_{zz}}$ ($\beta_k = 0$). This corresponds to an exponential decay with decay constant

$$\alpha_k = -\ln(\beta_k)/a_{ac} = -2\ln\left(2\cos\left(\frac{ka_{zz}}{2}\right)\right)/a_{ac} \quad . \tag{6.1}$$

Here, as usual, $a_{ac} = \sqrt{3}a_{zz} = 3a$, where $a \approx 0.142\,\text{nm}$ denotes the carbon-carbon bond length. It is worth noting that the decay constant is independent of the hopping integral t and instead determined exclusively by the geometry of the lattice.

Figure 6.2 (b) shows a superposition $\psi_{k_0^+} + \psi_{k_0^-}$ of two Bloch states with crystal wave vectors[5]

$$k_0^{\pm} = \frac{\pi}{a_{zz}} \pm \frac{2\pi}{\lambda} = \frac{\pi}{a_{zz}}\left(1 \pm \frac{1}{4}\right) \quad . \tag{6.2}$$

[5]Using the standard convention for the Brillouin zone of zigzag GNRs, as shown in Figure 6.2 (a).

This particular linear combination satisfies the boundary conditions of the $M = 7$ AGNR, namely that the wave function must vanish at the first carbon sites *outside* the GNR, which are separated by $(M+1)\frac{a_{zz}}{2} = 4a_{zz}$. Within the tight binding framework, the edge state at the terminus of a 7-AGNR is therefore directly linked to the Bloch states of the infinite zigzag edge with crystal wave vectors $k = k_0^{\pm}$. Its exponential decay perpendicular to the zigzag edge is given by the constant $\alpha_{k_0} \approx 1.3/\text{nm}$ (with decay constant $2\alpha_{k_0} \approx 2.5/\text{nm}$ for the charge density).

The edge states of the semi-infinite graphene sheet are singly occupied. In chemical terms, the 7-AGNR of infinite length therefore has an *open shell* near the terminus. For 7-AGNRs of finite length, however, the edge states (Tamm states [134]) of its two termini overlap. This gives rise to a finite energy splitting Δ_{zz} between a *bonding* and an *antibonding* linear combination of edge states, depicted in Figure 6.2 (c). As the length $L = Na_{ac}/2$ of the GNR increases, the splitting $\Delta_{zz}(L)$ decays exponentially, with numerical values reported in Table 6.1. Note that the splitting between edge states constitutes the *fundamental gap* of the system: $\Delta_{zz} = \text{IP} - \text{EA}$, where IP is the ionization potential and EA the electron affinity of the GNR.

6.3 Density functional theory

Within spin-restricted Kohn-Sham density functional theory, the Kohn-Sham gap also approaches zero in the limit of of $L \to \infty$ (not shown). When moving to spin-unrestricted DFT, however, the breaking of spin-symmetry, illustrated in Figure 6.3 (b), gives rise to a staggered sublattice potential for each spin channel, which opens a finite gap [88].

Density functional theory calculations of finite 7-AGNRs were performed using the PBE generalized-gradient approximation [63] as implemented in the Quantum ESPRESSO package [155]. The Kohn-Sham orbitals were expanded on a plane-wave basis set with energy cutoff at 120 Ry, using norm-conserving pseudo potentials [191]. The simulation cell was chosen at least twice as large as the $10^{-5}/a_0^3$ isosurface of the charge density in order to enable the use of the Martyna-Tuckerman Poisson solver [192] for the charged systems. Atomic positions were relaxed until the forces acting on the atoms were below $1\,\text{meV/Å}$.

Table 6.1 reports the length-dependence of the Kohn-Sham gap. The gap is found to converge exponentially to the finite value of $0.56\,\text{eV}$ for $L \to \infty$.[6]

However, it is well-known that the Kohn-Sham gaps provided by approximate semi-local exchange-correlation functionals severely underestimate the fundamental gaps of many bulk insulators and molecules. This is not even necessarily a failure of the approximation, since the Kohn-Sham gap lacks the derivative discontinuity of the exchange-correlation functional even within exact DFT [193]. On the other hand, the fundamental gap of finite systems can

[6] Which is slightly larger than in a detailed study by Ijäs and coworkers [154].

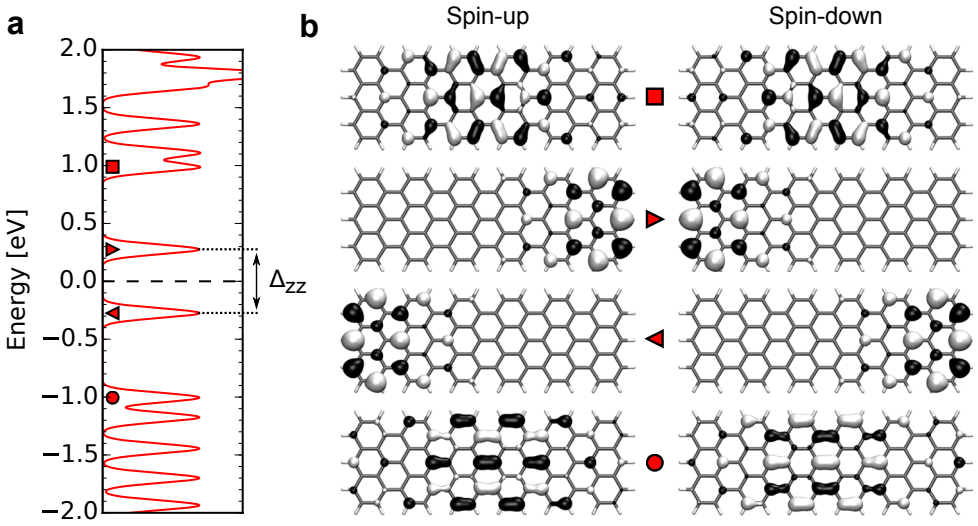

Figure 6.3: Edge states in spin-unrestricted Kohn-Sham DFT. (a) Energy levels and density of states for finite 7-AGNR of length $N = 12$, degenerate between spins. The DOS was obtained by Gaussian broadening with full width 0.1 eV at half-maximum. (b) Isosurfaces of frontier orbitals at $\psi = \pm 0.2\, a_0^{-3/2}$. The sign is indicated by the colors black and white.

be obtained as a difference of *total* energies

$$\Delta = \mathrm{IP} - \mathrm{EA} = E_{N-1} - E_N - (E_N - E_{N+1}) \tag{6.3}$$

where E_N and $E_{N\pm1}$ denote the total energy of the neutral and singly charged systems. Formula (6.3) is exact within exact DFT and this so-called δ-self-consistent-field (δ-SCF) approach is often found to be reasonably accurate for molecules within *approximate* DFT [194, 195].

Δ_{zz} [eV]	$N = 2$	$N = 4$	$N = 6$	$N = 8$	$N = 12$
TB ($t = 3$ eV)	1.06	0.31	0.10	0.03	0.00
PBE (KS)	2.32	0.90	0.57	0.56	0.56
PBE (δ-SCF)	6.3*	4.13	3.30	2.93	2.50
G_0W_0@PBE	6.49	4.03	3.00	2.86	2.85

Table 6.1: Fundamental gap $\Delta_{zz} = \mathrm{IP} - \mathrm{EA}$ of finite CH-terminated 7-AGNRs as a function of length $L = Na_{ac}/2$. Reported are the tight binding gap (TB), PBE Kohn-Sham (KS) gap, PBE δ-SCF gap and the G_0W_0 gap obtained using the PBE orbitals and eigenenergies. Value marked by * involves substantial uncertainty of ± 0.25 eV due to convergence problems of the SCF for the negatively charged system.

Using the same computational setup described before,[7] the δ-SCF approach yields dramatically increased gaps, as reported in Table 6.1. But not only that: Figure 6.4 (a) illustrates that the decay of Δ_{zz} for $L \to \infty$ changes from exponential to $O(1/L)$ (red dots). As explained below, this slowing down of convergence arises from a breakdown of the semi-local approximation to exchange and is qualitatively incorrect.

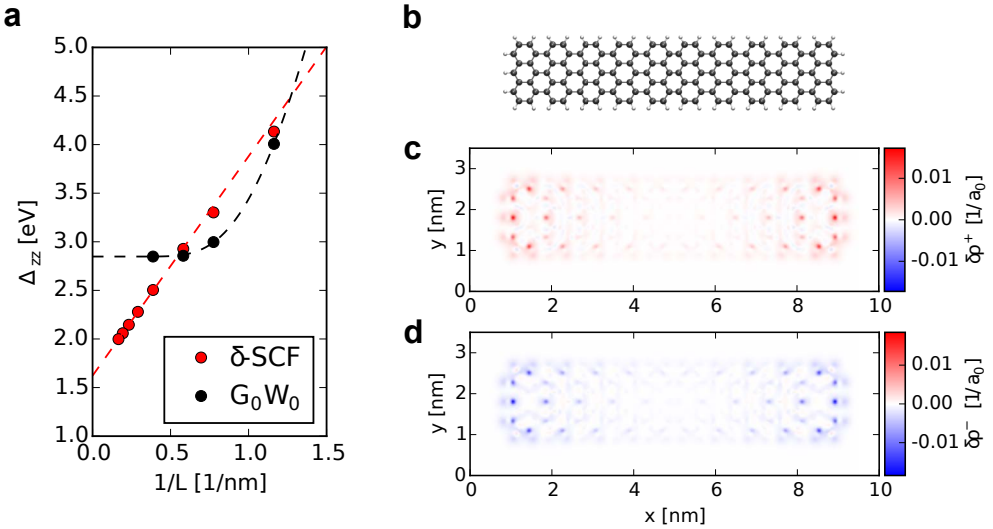

Figure 6.4: δ-SCF approach. (a) Comparing $\Delta_{zz}(1/L)$ between δ-SCF and G_0W_0. A linear fit to the δ-SCF data in the range $1/L \in [0, 0.5\,\mathrm{nm}^{-1}]$ yields $\Delta_{zz}(\infty) \approx 1.6\,\mathrm{eV}$. (b) Model of CH-terminated 7-AGNR of length $N = 20$. (c) Corresponding charge density difference $\delta\rho^+(x,y) = \int \rho_{N+1}(x,y,z) - \rho_N(x,y,z)\,dz$ between negatively charged and neutral GNR. (d) Charge density difference $\delta\rho^-(x,y)$ between positively charged and neutral GNR.

One may first suspect that problems could arise from the lack of the derivative discontinuity in the approximate exchange-correlation functional, which has been shown to imply that the δ-SCF gap converges to the Kohn-Sham gap in the limit of infinite system size [196, 197]. However, the proof of this theorem rests on the assumption that the charge density difference $\delta\rho$ between the neutral and charged system goes to zero everywhere as the system size increases. Figures 6.4 (c) and (d) illustrate that this is not the case here: as $L \to \infty$, the charge density difference upon electron addition ($\delta\rho^+$) and removal ($\delta\rho^-$) remains concentrated near the termini and follows the shape of the edge-localized low-energy states.

The charge-density difference nevertheless holds the key to understanding the large-L limit of $\Delta_{zz}(L)$. The additional (negative or positive) charge is

[7] Employing the Martyna-Tuckerman Poisson solver [192] for the charged systems and ensuring sufficient vacuum between periodic replica, as required.

distributed symmetrically over both termini, i.e., the charged systems have an additional charge of $|q| = 1/2|e|$ near each terminus. While these charges physically belong to the same electron, a semi-local approximation to exchange is, by construction, unable to cancel their electrostatic self-interaction.[8] Thus, the two separate charges repel each other, giving rise to a spurious long-range $1/L$ term that enters E_{N+1} and E_{N-1} with the same sign and dominates the length-dependence of the δ-SCF gap at large lengths L.

A method is therefore needed that includes both long-range exchange and correlation.[9] Knowing from comparison with experiment that the Kohn-Sham wave functions of the neutral system are quite accurate, we have chosen to perform one-shot G_0W_0 calculations.

6.4 Quasiparticle corrections

Quasi-particle corrections for finite 7-AGNRs of lengths $N = 2, 4, 6, 8$ and 12[10] were computed within the framework of many-body perturbation theory, using the G_0W_0 approximation to the self-energy as implemented in the BerkeleyGW package [81, 162]. The electronic structure from DFT was recalculated using 60 Ry plane-wave cutoff, computing sufficient numbers of empty states to cover the energy range up to 1.6 Ry above the highest occupied band. The static dielectric matrix was calculated in the random phase approximation with 8 Ry cutoff for the plane-wave basis. ε^{-1} was extended to the real frequency axis using the generalized plasmon-pole model by Hybertsen and Louie [81]. A rectangular Coulomb-cutoff was employed along the aperiodic dimensions as described in reference [160]. In the calculation of the self-energy, the static remainder approach was used to speed up the convergence with respect to the number of empty bands [163].

The values for the fundamental gap[11] are reported in Table 6.1 and compared against the δ-SCF results in Figure 6.4 (a). While the *GW* gap for the smallest systems is remarkably close to the δ-SCF gap, its length-dependence is again exponential, as illustrated in Figure 6.4 (a). One obtains a value of $\Delta_{zz}(\infty) \approx 2.8 \pm 0.2\,\text{eV}$, where the error bar represents an estimate of the convergence in the number of empty bands as well as the plane-wave cutoff for the dielectric function. Note that this value for $\Delta_{zz}(\infty)$ is significantly larger

[8] Which is contained in the Hartree energy.

[9] We note that the 7-AGNR of length $N = 12$ has been studied within the many-body Hubbard model, including hopping up to third-nearest neighbors [154]. Yet, a value of $U/t \approx 0.7$ yields just a tiny splitting of $\Delta_{zz} = 0.17\,\text{eV}$, which seems to indicate that the on-site approximation for the Coulomb interaction is quite severe in this context.

[10] The 7-AGNR with length $N = 12$ contains 114 atoms.

[11] The value of 6.5 eV found for anthracene ($N = 2$) is reasonably close to the value of 6.7 eV reported for anthracene using *GW* with LDA wave functions and self-consistent determination of the quasiparticle energies [198].

than the gap between even the most strongly localized edge states at *infinite* zigzag edges, for which the G_0W_0 approach predicts a value of $\approx 1.9\,\text{eV}$ [161].

6.5 Electronic decoupling from the metal surface

The bottom-up strategy for the synthesis of GNRs relies on the catalytic activity of the metal substrate, and a direct synthesis on a semiconducting or insulating substrate, is not straightforward.[12] In order to characterize the intrinsic electronic structure of GNRs with zigzag edges, a *transfer* to a more inert substrate is required that does not affect the structural integrity of the atomically precise GNRs.

One possibility is to use atomically thin insulating NaCl films, deposited onto the metal substrate after GNR synthesis. In contrast to bulk insulating substrates, these films enable the investigation of the electronic properties of adsorbed GNRs by STM/STS, while considerably reducing their interaction with the underlying metal [199]. Through a four-step STM manipulation routine devised by Shiyong Wang [190], the transfer of 7-AGNRs with lengths ranging from 2 to 10 nm onto a monolayer of NaCl has been achieved without introducing any defects. The transfer process relies on the weak adhesion of 7-AGNRs to the Au(111) surface, which allows for lateral manipulation and controlled pick-up of individual GNRs by the STM tip [134].

Figure 6.5 (b) shows a typical STM scan of a short 7-AGNR on a NaCl island. Upon positioning the STM tip above the zigzag end of the decoupled GNR, the differential conductance spectrum now shows *two* peaks at bias voltages $-0.5\,V$ and $1.3\,\text{V}$, as displayed in Figure 6.5 (c). This is in stark contrast to the spectra recorded for 7-AGNRs adsorbed directly on Au(111), where no significant splitting was found (see Figure 6.1 (c)). The comparison of $\mathrm{d}I/\mathrm{d}V$ maps taken at these voltages with LDOS simulations shown in Figure 6.5 (d) and (e) prove that these two peaks indeed correspond to the filled and empty edge state at the zigzag edge. While the observed edge state splitting of $\Delta_{zz} \approx 1.9\,\text{eV}$ is still significantly smaller than the *GW* prediction of $2.8\,\text{eV}$, note that the theoretical value applies to free-standing GNRs. In experiment, significant screening is expected both from the NaCl monolayer and the underlying metal substrate, which is easily compatible with a reduction of the splitting by $\approx 1\,\text{eV}$.

Finally, the length-dependence of Δ_{zz} has been investigated experimentally, starting from 7-AGNRs of length $N = 12$ – the shortest GNRs that could be transferred successfully. According to the values reported in Table 6.2, Δ_{zz} is already converged within $0.1\,\text{eV}$ at length $N = 12$, in good agreement with *GW* calculations.

[12] Photoinduced polymerization of dibromo-bianthryl on mica has recently been attempted [25].

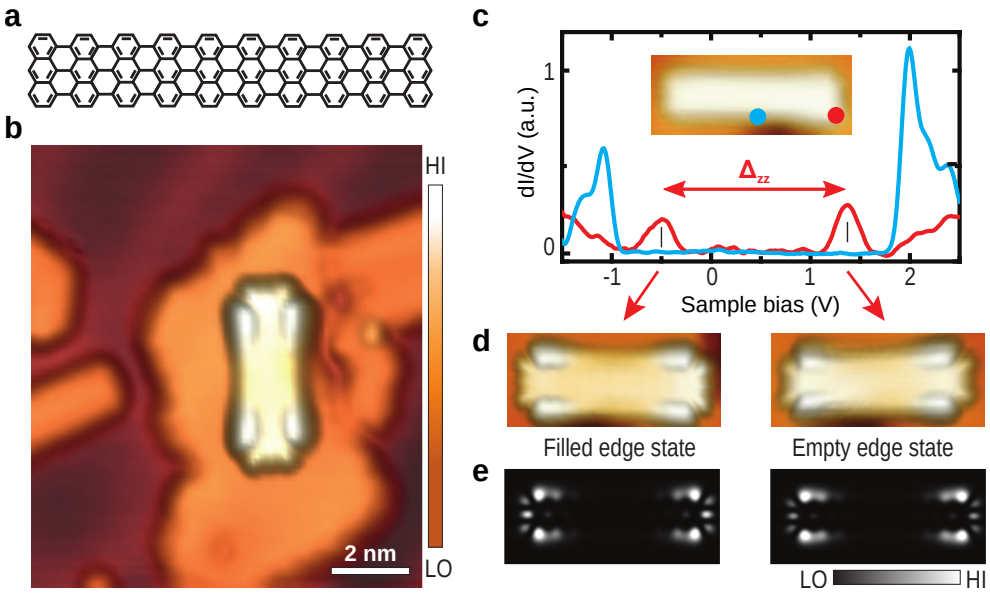

Figure 6.5: Electronic structure of short 7-AGNR on NaCl monolayer. (a) Structural model of 7-AGNR with length $N = 20$. (b) STM topography image of 7-AGNR with length $N = 20$ after transfer to NaCl monolayer island through STM manipulation ($U = -1.0\,\mathrm{V}$, $I = 30\,\mathrm{pA}$). (c) $\mathrm{d}I/\mathrm{d}V$ spectra measured in the center (blue) and at one end (red) of the decoupled GNR. Inset: STM topography image for sample bias in the band gap of the ribbon ($U = -0.1\,\mathrm{V}$,$I = 30\,\mathrm{pA}$). (d) STM topography images showing the orbital shapes of the occupied edge state (left, $U = -1.0\,\mathrm{V}$, $I = 30\,\mathrm{pA}$) and the unoccupied edge state (right, $U = 1.4\,\mathrm{V}$, $I = 30\,\mathrm{pA}$). (e) Local density of states of corresponding PBE Kohn-Sham orbitals at 4 Å tip-sample distance. Experimental data recorded by Shiyong Wang.

L [N]	12	16	20	48
Δ_{zz} [eV]	1.91	1.88	1.87	1.85

Table 6.2: Edge state splitting Δ_{zz} of finite CH-terminated 7-AGNRs as a function of length. Determined by STS on a monolayer of NaCl on Au(111). Data recorded by Shiyong Wang.

6.6 Discussion and outlook

The electronic structure of graphene zigzag edges has been investigated within the frameworks of tight binding, density functional theory and the GW approximation to many-body perturbation theory, focusing in particular on the short zigzag edge found at the termini of 7-AGNRs. In agreement with previous works [132, 154], each terminus is predicted to host one occupied and

one empty localized state, both of which are energetically isolated from the bulk electronic states of the AGNR. This differs from the case of graphene nanostructures with long zigzag edges, where the energies of edge-localized and delocalized states are predicted to overlap [87, 161], and makes this short zigzag edge particularly suitable for experimental investigation. The comparison with scanning tunneling spectroscopy experiments performed on Au(111) indicates that the interaction between monohydrogenated, defect-free zigzag edges and the Au(111) surface is far from negligible, despite the fact that Au is generally considered the most inert of all metals [200].

This is bad news for studying the intrinsic properties of zigzag edges on metal surfaces, in particular concerning more delicate issues, such as the alignment of electronic spins along the zigzag edge. While the observation of magnetic ordering at graphene zigzag edges on Au(111) has been reported in recent years [201, 202], these claims are based merely on the observation of an energy splitting in scanning tunneling spectroscopy. The link is usually established through Kohn-Sham DFT with approximate exchange-correlation functionals or the mean-field approximation to the Hubbard model [201, 202], which indeed predict a gap in the spectrum of the non-interacting system only in the presence of spin polarization. However, these theories lack the derivative discontinuity [203], which can give rise to a finite gap for open-shell systems also in the absence of spin polarization [193]. It is therefore highly questionable, whether the observation of an electronic splitting of edge-localized states *alone* may serve as an indication of spin polarization.

Although it may be difficult to study the intrinsic electronic structure of zigzag edges adsorbed on metals, the experimental and theoretical findings reported here indicate that decoupling by a *single* atomic layer of an insulator can be enough to restore the electronic structure at the zigzag edge to (qualitative) agreement with theoretical predictions for free-standing GNRs that account for many-body effects. Since 7-AGNRs host just a single localized electron at each terminus, they are not suitable for studying the long-predicted alignment of spins *along* the zigzag edge. Nevertheless, the insights gained in this study constitute a significant step forward in the collective effort to access this intriguing phenomenon, especially in view of the fact that the synthesis of *zigzag* GNRs[13] has recently been achieved [204].

[13]Specifically, the $N = 6$ ZGNR was synthesized on Au(111).

Bibliography

[1] Peter Rodgers. „Molecular Magnetism takes off.“ In: *Physics world* (April 1997), p. 28.

[2] Andre Konstantin Geim. „Random walk to graphene (Nobel lecture).“ In: *Angewandte Chemie (International ed. in English)* 50.31 (2011), pp. 6966–85. DOI: 10.1002/anie.201101174.

[3] Takuya Fujimoto and Kunio Awaga. „Electric-double-layer field-effect transistors with ionic liquids.“ In: *Physical chemistry chemical physics* 15 (2013), pp. 8983–9006. DOI: 10.1039/c3cp50755f.

[4] Simon Min Sze and Kwok Kwok Ng. *Physics of Semiconductor Devices*. 3rd ed. 2007.

[5] Mildred S. Dresselhaus and Gene Dresselhaus. „Intercalation compounds of graphite.“ In: *Advances in Physics* 51.1 (2002), pp. 1–186. DOI: 10.1080/00018730110113644.

[6] Konstantin Sergeevich Novoselov, Andre Konstantin Geim, et al. „Electric field effect in atomically thin carbon films.“ In: *Science (New York, N.Y.)* 306.5696 (2004), pp. 666–9. DOI: 10.1126/science.1102896.

[7] Kirill I. Bolotin, Kenneth J. Sikes, et al. „Temperature-Dependent Transport in Suspended Graphene.“ In: *Physical Review Letters* 101.9 (2008), p. 096802. DOI: 10.1103/PhysRevLett.101.096802.

[8] Alexander S. Mayorov, Roman V. Gorbachev, et al. „Micrometer-Scale Ballistic Transport in Encapsulated Graphene at Room Temperature.“ In: *Nano Letters* 11.6 (2011), pp. 2396–2399. DOI: 10.1021/nl200758b.

[9] Changgu Lee, Xiaoding Wei, et al. „Measurement of the Elastic Properties and Intrinsic Strength of Monolayer Graphene.“ In: *Science* 321.5887 (2008), pp. 385–388. DOI: 10.1126/science.1157996.

[10] Alexander A. Balandin, Suchismita Ghosh, et al. „Superior Thermal Conductivity of Single-Layer Graphene.“ In: *Nano Letters* 8.3 (2008), pp. 902–7. DOI: 10.1021/nl0731872.

[11] Rui Cheng, Jingwei Bai, et al. „High-frequency self-aligned graphene transistors with transferred gate stacks.“ In: *Proceedings of the National Academy of Sciences* 109.29 (2012), pp. 11588–92. DOI: 10.1073/pnas.1205696109.

[12] Frank Schwierz. „Graphene Transistors: Status, Prospects, and Problems.“ In: *Proceedings of the IEEE* 101.7 (2013), pp. 1567–1584. DOI: 10.1109/JPROC.2013.2257633.

[13] Nicholas Petrone, Inanc Meric, et al. „Graphene Field-Effect Transistors with Gigahertz-Frequency Power Gain on Flexible Substrates.“ In: *Nano Letters* 13.1 (2013), pp. 121–5. DOI: 10.1021/nl303666m.

[14] Verónica Barone, Oded Hod, and Gustavo E. Scuseria. „Electronic structure and stability of semiconducting graphene nanoribbons.“ In: *Nano letters* 6.12 (2006), pp. 2748–54. DOI: 10.1021/nl0617033.

[15] Liang Ma, Jinlan Wang, and Feng Ding. „Recent Progress and Challenges in Graphene Nanoribbon Synthesis.“ In: *ChemPhysChem* 14.1 (2013), pp. 47–54. DOI: 10.1002/cphc.201200253.

[16] Jinming Cai, Pascal Ruffieux, et al. „Atomically precise bottom-up fabrication of graphene nanoribbons.“ In: *Nature* 466.7305 (2010), pp. 470–3. DOI: 10.1038/nature09211.

[17] Akimitsu Narita, Xinliang Feng, et al. „Synthesis of structurally well-defined and liquid-phase-processable graphene nanoribbons.“ In: *Nature Chemistry* 6.2 (2014), pp. 126–132. DOI: 10.1038/nchem.1819.

[18] Leonhard Grill, Matthew Dyer, et al. „Nano-architectures by covalent assembly of molecular building blocks.“ In: *Nature nanotechnology* 2.11 (2007), pp. 687–91. DOI: 10.1038/nnano.2007.346.

[19] Leif Lafferentz, Francisco Ample, et al. „Conductance of a Single Conjugated Polymer as a Continuous Function of Its Length.“ In: *Science* 323.5918 (2009), pp. 1193–1197. DOI: 10.1126/science.1168255.

[20] Josh A. Lipton-Duffin, Oleksandr Ivasenko, et al. „Synthesis of polyphenylene molecular wires by surface-confined polymerization.“ In: *Small* 5.5 (2009), pp. 592–7. DOI: 10.1002/smll.200801943.

[21] Pascal Ruffieux, Jinming Cai, et al. „Electronic Structure of Atomically Precise Graphene Nanoribbons.“ In: *ACS Nano* 6.8 (2012), pp. 6930–5. DOI: 10.1021/nn3021376.

[22] Stephan Blankenburg, Jinming Cai, et al. „Intraribbon heterojunction formation in ultranarrow graphene nanoribbons.“ In: *ACS nano* 6.3 (2012), pp. 2020–5. DOI: 10.1021/nn203129a.

[23] „Process for preparing graphene nanoribbons.“ WO 2014045148 A1. Tobias Hintermann, Roman Fasel, et al. 2014.

[24] Patrick B. Bennett, Zahra Pedramrazi, et al. „Bottom-up graphene nanoribbon field-effect transistors.“ In: *Applied Physics Letters* 103.25 (2013), p. 253114. DOI: 10.1063/1.4855116.

[25] Carlos-Andres Palma, Katharina Diller, et al. „Photoinduced C-C reactions on insulators toward photolithography of graphene nanoarchitectures.“ In: *Journal of the American Chemical Society* 136.12 (2014), pp. 4651–8. DOI: 10.1021/ja412868w.

[26] Yen-Chia Chen, Dimas G. de Oteyza, et al. „Tuning the Band Gap of Graphene Nanoribbons Synthesized from Molecular Precursors.“ In: *ACS Nano* 7.7 (2013), pp. 6123–8. DOI: 10.1021/nn401948e.

[27] Hajo Söde, Leopold Talirz, et al. „Synthesis and characterization of atomically precise N=9 armchair graphene nanoribbon.“ In preparation.

[28] NIST, Gaithersburg. *X-ray Photoelectron Spectroscopy Database, Version 4.1*. 2015. URL: http://srdata.nist.gov/xps.

[29] Daniel Huertas-Hernando, Francisco Guinea, and Arne Brataas. „Spin-orbit coupling in curved graphene, fullerenes, nanotubes, and nanotube caps.“ In: *Physical Review B* 74.15 (2006), p. 155426. DOI: 10.1103/PhysRevB.74.155426.

[30] Max Born and J. Robert Oppenheimer. „Zur Quantentheorie der Molekeln.“ In: *Annalen der Physik* 389.20 (1927), pp. 457–84. DOI: 10.1002/andp.19273892002.

[31] Max Born and Kun Huang. *Dynamical Theory of Crystal Lattices*. Clarendon press, Oxford, 1954.

[32] Simone Pisana, Michele Lazzeri, et al. „Breakdown of the adiabatic Born-Oppenheimer approximation in graphene.“ In: *Nature Materials* 6.3 (2007), pp. 198–201. DOI: 10.1038/nmat1846.

[33] Manuel Cardona and Mike L. W. Thewalt. „Isotope effects on the optical spectra of semiconductors.“ In: *Reviews of Modern Physics* 77.4 (2005), pp. 1173–1224. DOI: 10.1103/RevModPhys.77.1173.

[34] Samuel Poncé, Gabriel Antonius, et al. „Verification of first-principles codes: Comparison of total energies, phonon frequencies, electron-phonon coupling and zero-point motion correction to the gap between ABINIT and QE/Yambo.“ In: *Computational Materials Science* 83 (2014), pp. 341–8. DOI: 10.1016/j.commatsci.2013.11.031.

[35] Eberhard K. U. Gross. „Reduced-density-matrix-functional theory.“ Technical University of Denmark, Department of Physics, 16.8.2012.

[36] Pierre Hohenberg and Walter Kohn. „Inhomogeneous Electron Gas.“ In: *Physical Review* 136.3B (1964), B864–71. DOI: 10.1103/PhysRev.136.B864.

[37] Thomas L. Gilbert. „Hohenberg-Kohn theorem for nonlocal external potentials.“ In: *Physical Review B* 12.6 (1975), pp. 2111–20. DOI: 10.1103/PhysRevB.12.2111.

[38] Tim Baldsiefen. „Reduced density matrix functional theory at finite temperature.“ Freie Universität Berlin, 2012.

[39] Viktor M. Galitskii and Arkadi B. Migdal. „Application of Quantum field theory methods to the many-body problem.“ In: *Zhurnal Eksperimental'noi i Teoreticheskoi Fiziki* 34.1 (1958), pp. 139–150.

[40] Joaquin M. Luttinger and John C. Ward. „Ground-State Energy of a Many-Fermion System. II.“ In: *Physical Review* 118.5 (1960), pp. 1417–27. DOI: 10.1103/PhysRev.118.1417.

[41] Abraham Klein. „Perturbation Theory for an Infinite Medium of Fermions. II.“ In: *Physical Review* 121.4 (1961), pp. 950–6. DOI: 10.1103/PhysRev.121.950.

[42] Fabien Bruneval. „Ionization energy of atoms obtained from GW self-energy or from random phase approximation total energies.“ In: *Journal of Chemical Physics* 136.2012 (2012), p. 194107. DOI: 10.1063/1.4718428.

[43] Fabio Caruso, Patrick Rinke, et al. „Unified description of ground and excited states of finite systems: The self-consistent GW approach.“ In: *Physical Review B* 86.8 (2012), p. 081102. DOI: 10.1103/PhysRevB.86.081102.

[44] Fabio Caruso, Patrick Rinke, et al. „Self-consistent GW: All-electron implementation with localized basis functions.“ In: *Physical Review B* 88.7 (2013), p. 075105. DOI: 10.1103/PhysRevB.88.075105.

[45] C. David Sherrill and Henry F. Schaefer. „The Configuration Interaction Method: Advances in Highly Correlated Approaches.“ In: *Advances in Quantum Chemistry*. Vol. 34. Academic Press, 1999, pp. 143–269.

[46] Dieter Cremer. „Møller-Plesset perturbation theory: from small molecule methods to methods for thousands of atoms.“ In: *Wiley Interdisciplinary Reviews: Computational Molecular Science* 1.4 (2011), pp. 509–530. DOI: 10.1002/wcms.58.

[47] Rodney J. Bartlett and Monika Musiał. „Coupled-cluster theory in quantum chemistry.“ In: *Reviews of Modern Physics* 79.1 (2007), pp. 291–352. DOI: 10.1103/RevModPhys.79.291.

[48] Brian M. Austin, Dmitry Yu. Zubarev, and William A. Lester. „Quantum Monte Carlo and Related Approaches.“ In: *Chemical Reviews* 112.1 (2012), pp. 263–288. DOI: 10.1021/cr2001564.

[49] Axel D. Becke. „Density-functional thermochemistry. III. The role of exact exchange.“ In: *The Journal of Chemical Physics* 98.7 (1993), pp. 5648–52. DOI: 10.1063/1.464913.

[50] Chengteh Lee, Weitao Yang, and Robert G. Parr. „Development of the Colle-Salvetti correlation-energy formula into a functional of the electron density.“ In: *Physical Review B* 37.2 (1988), pp. 785–9. DOI: 10.1103/PhysRevB.37.785.

[51] Richard Van Noorden, Brendan Maher, and Regina Nuzzo. „The top 100 papers.“ In: *Nature* 514.7524 (2014), pp. 550–3. DOI: 10.1038/514550a.

[52] Eberhard Engel and Reiner M. Dreizler. *Density Functional Theory*. Springer Berlin Heidelberg, 2011.

[53] Richard M. Martin. *Electronic Structure: Basic Theory and Practical Methods*. Cambridge University Press, 2004.

[54] Mel Levy. „Universal variational functionals of electron densities, first-order density matrices, and natural spin-orbitals and solution of the v-representability problem.“ In: *Proceedings of the National Academy of Sciences* 76.12 (1979), pp. 6062–5.

[55] Elliott H. Lieb. „Density functionals for coulomb systems.“ In: *International Journal of Quantum Chemistry* 24.3 (1983), pp. 243–277. DOI: 10.1002/qua.560240302.

[56] Llewellyn H. Thomas. „The calculation of atomic fields.“ In: *Mathematical Proceedings of the Cambridge Philosophical Society* 23.05 (1927), pp. 542–548. DOI: 10.1017/S0305004100011683.

[57] Enrico Fermi. „Un metodo statistico per la determinazione di alcune proprieta dell'atomo.“ In: *Rend. Lincei* 6.6 (1927), pp. 602–7.

[58] Paul A. M. Dirac. „Note on Exchange Phenomena in the Thomas Atom.“ In: *Mathematical Proceedings of the Cambridge Philosophical Society* 26.03 (1930), pp. 376–385. DOI: 10.1017/S0305004100016108.

[59] Edward Teller. „On the Stability of Molecules in the Thomas-Fermi Theory.“ In: *Reviews of Modern Physics* 34.4 (1962), pp. 627–631. DOI: 10.1103/RevModPhys.34.627.

[60] Walter Kohn and Lu J. Sham. „Self-Consistent Equations Including Exchange and Correlation Effects.“ In: *Physical Review* 140.4A (1965), A1133–8. DOI: 10.1103/PhysRev.140.A1133.

[61] David M. Ceperley and Berni J. Alder. „Ground State of the Electron Gas by a Stochastic Method.“ In: *Physical Review Letters* 45.7 (1980), pp. 566–569. DOI: 10.1103/PhysRevLett.45.566.

[62] John P. Perdew and Alex Zunger. „Self-interaction correction to density-functional approximations for many-electron systems.“ In: *Physical Review B* 23.10 (1981), pp. 5048–5079. DOI: 10.1103/PhysRevB.23.5048.

[63] John P. Perdew, Kieron Burke, and Matthias Ernzerhof. „Generalized Gradient Approximation Made Simple.“ In: *Physical Review Letters* 77.18 (1996), pp. 3865–3868. DOI: 10.1103/PhysRevLett.77.3865.

[64] Axel D. Becke. „A new mixing of Hartree-Fock and local density-functional theories.“ In: *The Journal of Chemical Physics* 98.2 (1993), pp. 1372–7. DOI: 10.1063/1.464304.

[65] Axel D. Becke. „Density-functional thermochemistry. V. Systematic optimization of exchange-correlation functionals.“ In: *The Journal of Chemical Physics* 107.20 (1997), pp. 8554–60. DOI: 10.1063/1.475007.

[66] Henrik Rydberg, Max Dion, et al. „Van der Waals Density Functional for Layered Structures.“ In: *Physical Review Letters* 91.12 (2003), p. 126402. DOI: 10.1103/PhysRevLett.91.126402.

[67] Stefan Grimme. „Density functional theory with London dispersion corrections.“ In: *Wiley Interdisciplinary Reviews: Computational Molecular Science* 1.2 (2011), pp. 211–228. DOI: 10.1002/wcms.30.

[68] Stefan Grimme, Jens Antony, et al. „A consistent and accurate ab initio parametrization of density functional dispersion correction (DFT-D) for the 94 elements H-Pu.“ In: *The Journal of chemical physics* 132.15 (2010), p. 154104. DOI: 10.1063/1.3382344.

[69] Alexandre Tkatchenko and Matthias Scheffler. „Accurate Molecular Van Der Waals Interactions from Ground-State Electron Density and Free-Atom Reference Data.“ In: *Physical Review Letters* 102.7 (2009), p. 073005. DOI: 10.1103/PhysRevLett.102.073005.

[70] Victor G. Ruiz, Wei Liu, et al. „Density-Functional Theory with Screened van der Waals Interactions for the Modeling of Hybrid Inorganic-Organic Systems.“ In: *Physical Review Letters* 108.14 (2012), p. 146103. DOI: 10.1103/PhysRevLett.108.146103.

[71] Felix Hanke. „Sensitivity Analysis and Uncertainty Calculation for Dispersion Corrected Density Functional Theory.“ In: *Journal of Computational Chemistry* 32 (2011), pp. 1424–30. DOI: 10.1002/jcc.21724.

[72] Max Dion, Henrik Rydberg, et al. „Van der Waals Density Functional for General Geometries.“ In: *Physical Review Letters* 92.24 (2004), p. 246401. DOI: 10.1103/PhysRevLett.92.246401.

[73] Kyuho Lee, Éamonn D. Murray, et al. „Higher-accuracy van der Waals density functional.“ In: *Physical Review B* 82.8 (2010), p. 081101. DOI: 10.1103/PhysRevB.82.081101.

[74] Ikutaro Hamada. „van der Waals density functional made accurate.“ In: *Physical Review B* 89.12 (2014), p. 121103. DOI: 10.1103/PhysRevB.89.121103.

[75] Andris Gulans, Martti Puska, and Risto Nieminen. „Linear-scaling self-consistent implementation of the van der Waals density functional.“ In: *Physical Review B* 79.20 (2009), p. 201105. DOI: 10.1103/PhysRevB.79.201105.

[76] Friedhelm Bechstedt. *Many-Body Approach to Electronic Excitations*. 1st ed. Springer Berlin Heidelberg, 2015. 584 pp.

[77] Christoph Friedrich and Arno Schindlmayr. „Many-body perturbation theory: the GW approximation.“ In: *NIC Series* 31 (2006), p. 335.

[78] Lars Hedin. „New Method for Calculating the One-Particle Green's Function with Application to the Electron-Gas Problem.“ In: *Physical Review* 139.3A (1965), A796–A823. DOI: 10.1103/PhysRev.139.A796.

[79] Fabien Bruneval and Matteo Gatti. „Quasiparticle Self-Consistent GW Method for the Spectral Properties of Complex Materials.“ In: *Top Curr Chem* (2014), pp. 13–35. DOI: 10.1007/128_2013_460.

[80] Rex W. Godby, Michael Schlüter, and L. J. Sham. „Self-energy operators and exchange-correlation potentials in semiconductors.“ In: *Physical Review B* 37.17 (1988), pp. 10159–10175. DOI: 10.1103/PhysRevB.37.10159.

[81] Mark S. Hybertsen and Steven G. Louie. „Electron correlation in semiconductors and insulators: Band gaps and quasiparticle energies.“ In: *Physical Review B* 34.8 (1986), pp. 5390–5413. DOI: 10.1103/PhysRevB.34.5390.

[82] Rex W. Godby and Richard J. Needs. „Metal-insulator transition in Kohn-Sham theory and quasiparticle theory.“ In: *Physical Review Letters* 62.10 (1989), pp. 1169–1172. DOI: 10.1103/PhysRevLett.62.1169.

[83] Patrick Duffy, Delano P. Chong, et al. „Assessment of Kohn-Sham density-functional orbitals as approximate Dyson orbitals for the calculation of electron-momentum-spectroscopy scattering cross sections.“ In: *Physical Review A* 50.6 (1994), pp. 4707–28. DOI: 10.1103/PhysRevA.50.4707.

[84] Erich Clar. *The aromatic sextet*. J, 1972.

[85] Shintato Fujii and Toshiaki Enoki. „Clar's Aromatic Sextet and π-Electron Distribution in Nanographene.“ In: *Angewandte Chemie* 124.29 (2012), pp. 7348–7353. DOI: 10.1002/ange.201202560.

[86] Tobias Wassmann, Ari P. Seitsonen, et al. „Clar's Theory, π-Electron Distribution, and Geometry of Graphene Nanoribbons.“ In: *Journal of the American Chemical Society* 132.10 (2010), pp. 3440–3451. DOI: 10.1021/ja909234y.

[87] Mitsutaka Fujita, Katsunori Wakabayashi, et al. „Peculiar Localized State at Zigzag Graphite Edge.“ In: *Journal of the Physical Society of Japan* 65.7 (1996), pp. 1920–1923. DOI: 10.1143/JPSJ.65.1920.

[88] Young-Woo Son, Marvin L. Cohen, and Steven G. Louie. „Energy Gaps in Graphene Nanoribbons.“ In: *Physical Review Letters* 97.21 (2006), p. 216803. DOI: 10.1103/PhysRevLett.97.216803.

[89] Marcus Elstner, Dirk Porezag, et al. „Self-consistent-charge density-functional tight-binding method for simulations of complex materials properties.“ In: *Physical Review B* 58.11 (1998), pp. 7260–7268. DOI: 10.1103/PhysRevB.58.7260.

[90] Philip R. Wallace. „The Band Theory of Graphite.“ In: *Physical Review* 71.9 (1947), pp. 622–634. DOI: 10.1103/PhysRev.71.622.

[91] „Tight Binding Calculation of Molecules and Solids.“ In: Riichiro Saito, Gene Dresselhaus, and Mildred S. Dresselhaus. *Physical Properties of Carbon Nanotubes*. 1998, pp. 17–33.

[92] Aaron Bostwick, Taisuke Ohta, et al. „Experimental Determination of the Spectral Function of Graphene.“ In: (2006).

[93] Stephanie Reich, Janina Maultzsch, et al. „Tight-binding description of graphene.“ In: *Physical Review B* 66.3 (2002), p. 035412. DOI: 10.1103/PhysRevB.66.035412.

[94] Erich Hückel. „Die freien Radikale der organischen Chemie.“ In: *Zeitschrift für Physik* 83.9-10 (1933), pp. 632–668. DOI: 10.1007/BF01330865.

[95] Linus Pauling, Lawrence O. Brockway, and J. Y. Beach. „The Dependence of Interatomic Distance on Single Bond-Double Bond Resonance1.“ In: *Journal of the American Chemical Society* 57.12 (1935), pp. 2705–9. DOI: 10.1021/ja01315a105.

[96] Kyoko Nakada, Mitsutaka Fujita, et al. „Edge state in graphene ribbons: Nanometer size effect and edge shape dependence.“ In: *Physical Review B* 54.24 (1996), pp. 17954–17961. DOI: 10.1103/PhysRevB.54.17954.

[97] Katsunori Wakabayashi, Ken-ichi Sasaki, et al. „Electronic states of graphene nanoribbons and analytical solutions.“ In: *Science and Technology of Advanced Materials* 11.5 (2010), p. 054504. DOI: 10.1088/1468-6996/11/5/054504.

[98] Hans H. Günthard and Hans Primas. „Zusammenhang von Graphentheorie und MO-Theorie von Molekeln mit Systemen konjugierter Bindungen." In: *Helvetica Chimica Acta* 39.6 (1956), pp. 1645–1653. DOI: 10.1002/hlca.19560390623.

[99] Xueliang Li, Yongtang Shi, and Ivan Gutman. „The Chemical Connection." In: *Graph Energy*. Springer New York, 2012, pp. 11–17.

[100] Siemion Fajtlowicz, Peter E. John, and Horst Sachs. „On maximum matchings and eigenvalues of benzenoid graphs." In: *Croatica chemica acta* 78.2 (2005), pp. 195–201.

[101] Wei Wang, Oleg Yazyev, et al. „Topological Frustration in Graphene Nanoflakes: Magnetic Order and Spin Logic Devices." In: *Physical Review Letters* 102.15 (2009), p. 157201. DOI: 10.1103/PhysRevLett.102.157201.

[102] Carter T. White, Junwen Li, et al. „Hidden One-Electron Interactions in Carbon Nanotubes Revealed in Graphene Nanostrips." In: *Nano Letters* 7.3 (2007), pp. 825–830. DOI: 10.1021/nl0627745.

[103] Daniel Gunlycke and Carter T. White. „Tight-binding energy dispersions of armchair-edge graphene nanostrips." In: *Physical Review B* 77.11 (2008), p. 115116. DOI: 10.1103/PhysRevB.77.115116.

[104] Timothy B. Boykin, Mathieu Luisier, et al. „Accurate six-band nearest-neighbor tight-binding model for the π-bands of bulk graphene and graphene nanoribbons." In: *Journal of Applied Physics* 109.10 (2011), p. 104304. DOI: 10.1063/1.3582136.

[105] John Hubbard. „Electron Correlations in Narrow Energy Bands." In: *Proceedings of the Royal Society of London A: Mathematical, Physical and Engineering Sciences* 276.1365 (1963), pp. 238–257. DOI: 10.1098/rspa.1963.0204.

[106] Fabian H. L. Essler, Holger Frahm, et al. *The One-Dimensional Hubbard Model*. Cambridge University Press, 2005.

[107] Elliott H. Lieb. „Two Theorems on the Hubbard Model." In: *Physical Review Letters* 62.16 (1989), pp. 1927–1927. DOI: 10.1103/PhysRevLett.62.1927.5.

[108] Sandro Sorella and Erio Tosatti. „Semi-Metal-Insulator Transition of the Hubbard Model in the Honeycomb Lattice." In: *EPL (Europhysics Letters)* 19.8 (1992), p. 699. DOI: 10.1209/0295-5075/19/8/007.

[109] Oleg V. Yazyev. „Emergence of magnetism in graphene materials and nanostructures." In: *Reports on Progress in Physics* 73.5 (2010), p. 056501. DOI: 10.1088/0034-4885/73/5/056501.

[110] Takeo Ito, Hideki Shirakawa, and Sakuji Ikeda. „Simultaneous polymerization and formation of polyacetylene film on the surface of concentrated soluble Ziegler-type catalyst solution." In: *Journal of Polymer Science: Polymer Chemistry Edition* 12.1 (1974), pp. 11–20. DOI: 10.1002/pol.1974.170120102.

[111] Hans Thomann, Larry K. Dalton, et al. „Direct observation of Coulomb correlation effects in polyacetylene." In: *Physical Review B* 31.5 (1985), pp. 3141–3143. DOI: 10.1103/PhysRevB.31.3141.

[112] Martin C. Gutzwiller. „Correlation of Electrons in a Narrow s Band." In: *Physical Review* 137.6A (1965), A1726–A1735. DOI: 10.1103/PhysRev.137.A1726.

[113] William F. Brinkman and Thomas M. Rice. „Application of Gutzwiller's Variational Method to the Metal-Insulator Transition." In: *Physical Review B* 2.10 (1970), pp. 4302–4304. DOI: 10.1103/PhysRevB.2.4302.

[114] Walter Metzner and Dieter Vollhardt. „Correlated Lattice Fermions in d=∞ Dimensions." In: *Physical Review Letters* 62.3 (1989), pp. 324–327. DOI: 10.1103/PhysRevLett.62.324.

[115] Hélène Feldner, Zi Yang Meng, et al. „Magnetism of finite graphene samples: Mean-field theory compared with exact diagonalization and quantum Monte Carlo simulations.“ In: *Physical Review B* 81.11 (2010), p. 115416. DOI: 10.1103/PhysRevB.81.115416.

[116] Yigal Meir and Ned S. Wingreen. „Landauer formula for the current through an interacting electron region.“ In: *Physical Review Letters* 68 (April 1992), pp. 2512–15. DOI: 10.1103/PhysRevLett.68.2512.

[117] Max Koentopp, Kieron Burke, and Ferdinand Evers. „Zero-bias molecular electronics: Exchange-correlation corrections to Landauer's formula.“ In: *Physical Review B* 73 (2006), 121403(R). DOI: 10.1103/PhysRevB.73.121403.

[118] Tonatiuh Rangel, Andrea Ferretti, et al. „Transport properties of molecular junctions from many-body perturbation theory.“ In: *Physical Review B* 84 (2011), p. 045426. DOI: 10.1103/PhysRevB.84.045426.

[119] Chengjun Jin and Kristian S. Thygesen. „Dynamical image-charge effect in molecular tunnel junctions: Beyond energy level alignment.“ In: *Physical Review B* 89 (2014), 041102(R). DOI: 10.1103/PhysRevB.89.041102.

[120] Leo Gross, Nikolaj Moll, et al. „High-Resolution Molecular Orbital Imaging Using a p-Wave STM Tip.“ In: *Physical Review Letters* 107.8 (2011), p. 086101. DOI: 10.1103/PhysRevLett.107.086101.

[121] Fabian Mohn, Bruno Schuler, et al. „Different tips for high-resolution atomic force microscopy and scanning tunneling microscopy of single molecules.“ In: *Applied Physics Letters* 102.7 (2013), p. 073109. DOI: 10.1063/1.4793200.

[122] John G. Simmons. „Generalized Formula for the Electric Tunnel Effect between Similar Electrodes Separated by a Thin Insulating Film.“ In: *Journal of Applied Physics* 34.6 (1963), p. 1793. DOI: 10.1063/1.1702682.

[123] Roberto Gaspari, Stephan Blankenburg, et al. „S-Orbital Continuum Model Accounting for the Tip Shape in Simulated Scanning Tunneling Microscope Images.“ In: *Physical Review B* 84.12 (2011), p. 125417. DOI: 10.1103/PhysRevB.84.125417.

[124] John Bardeen. „Tunnelling from a Many-Particle Point of View.“ In: *Physical Review Letters* 6.2 (1961), pp. 57–59. DOI: 10.1103/PhysRevLett.6.57.

[125] John B. Pendry, A. B. Pretre, and Ben C. H. Krutzen. „Theory of the scanning tunnelling microscope.“ In: *Journal of Physics: Condensed Matter* 3.24 (1991), p. 4313. DOI: 10.1088/0953-8984/3/24/001.

[126] Zhihong Chen, Yu-Ming Lin, et al. „Graphene nano-ribbon electronics.“ In: *Physica E: Low-dimensional Systems and Nanostructures* 40.2 (2007), pp. 228–232. DOI: 10.1016/j.physe.2007.06.020.

[127] Louise K. Dash, Herve Ness, et al. „Functionality in single-molecule devices: Model calculations and applications of the inelastic electron tunneling signal in molecular junctions.“ In: *The Journal of Chemical Physics* 136.6 (2012), p. 064708. DOI: 10.1063/1.3684627.

[128] Jerry D. Tersoff and Donald R. Hamann. „Theory of the scanning tunneling microscope.“ In: *Physical Review B* 31.2 (1985), pp. 805–813. DOI: 10.1103/PhysRevB.31.805.

[129] C. Julian Chen. „Tunneling matrix elements in three-dimensional space: The derivative rule and the sum rule.“ In: *Physical Review B* 42.14 (1990), pp. 8841–8857. DOI: 10.1103/PhysRevB.42.8841.

[130] Jerry D. Tersoff. „Method for the calculation of scanning tunneling microscope images and spectra.“ In: *Physical Review B* 40.17 (1989), pp. 11990–11993. DOI: 10.1103/PhysRevB.40.11990.

[131] Michael Rohlfing, Ruslan Temirov, and Frank Tautz. „Adsorption structure and scanning tunneling data of a prototype organic-inorganic interface: PTCDA on Ag(111).“ In: *Physical Review B* 76.11 (2007), pp. 1–16. DOI: 10.1103/PhysRevB.76.115421.

[132] Leopold Talirz, Hajo Söde, et al. „Termini of bottom-up fabricated graphene nanoribbons.“ In: *Journal of the American Chemical Society* 135.6 (2013), pp. 2060–3. DOI: 10.1021/ja311099k.

[133] Tobias Wassmann, Ari Seitsonen, et al. „Structure, Stability, Edge States, and Aromaticity of Graphene Ribbons.“ In: *Physical Review Letters* 101.9 (2008), p. 096402. DOI: 10.1103/PhysRevLett.101.096402.

[134] Matthias Koch, Francisco Ample, et al. „Voltage-dependent conductance of a single graphene nanoribbon.“ In: *Nature Nanotechnology* 7.11 (2012), pp. 713–7. DOI: 10.1038/nnano.2012.169.

[135] Nora Gonzalez Lakunza. „Study of the Geometry and Electronic Structure of Self-Assembled Monolayers on the Au (111) Surface.“ The University of the Basque Country, 2008.

[136] The CP2K developers group. *CP2K*. URL: http://www.cp2k.org.

[137] Stefan Goedecker, Michael Teter, and Jürg Hutter. „Separable dual-space Gaussian pseudopotentials.“ In: *Physical Review B* 54.3 (1996), pp. 1703–1710. DOI: 10.1103/PhysRevB.54.1703.

[138] Joost VandeVondele and Jürg Hutter. „Gaussian basis sets for accurate calculations on molecular systems in gas and condensed phases.“ In: *The Journal of chemical physics* 127.11 (2007), p. 114105. DOI: 10.1063/1.2770708.

[139] Leopold Talirz. *asetk*. 2015. URL: https://github.com/ltalirz/asetk.

[140] William M. Haynes, ed. *CRC Handbook of Chemistry and Physics*. 95th ed. CRC.

[141] Graeme Henkelman, Blas P. Uberuaga, and Hannes Jónsson. „A climbing image nudged elastic band method for finding saddle points and minimum energy paths.“ In: *The Journal of Chemical Physics* 113.22 (2000), pp. 9901–4. DOI: 10.1063/1.1329672.

[142] M. J. Murphy and Andrew Hodgson. „Internal state distributions for D2 recombinative desorption from Ag(111).“ In: *Surface Science*. Vibrations at Surfaces 368.1-3 (1996), pp. 55–60. DOI: 10.1016/S0039-6028(97)80022-2.

[143] Joost van der Lit, Mark P. Boneschanscher, et al. „Suppression of electron-vibron coupling in graphene nanoribbons contacted via a single atom.“ In: *Nature Communications* 4 (2013). DOI: 10.1038/ncomms3023.

[144] Hajo Söde. „Electronic properties of atomically precise graphene nanoribbons.“ Zürich, 2015. 132 pp.

[145] Steffen Linden, Dingyong Zhong, et al. „Electronic Structure of Spatially Aligned Graphene Nanoribbons on Au(788).“ In: *Physical Review Letters* 108.21 (2012), p. 216801. DOI: 10.1103/PhysRevLett.108.216801.

[146] Christopher Bronner, Felix Leyssner, et al. „Electronic structure of a subnanometer wide bottom-up fabricated graphene nanoribbon: End states, band gap, and dispersion.“ In: *Physical Review B* 86.8 (2012), p. 085444. DOI: 10.1103/PhysRevB.86.085444.

[147] Xiaobin Chen, Fuyang Tian, et al. „Interlayer interactions in graphites.“ In: *Scientific reports* 3 (2013), p. 3046. DOI: 10.1038/srep03046.

[148] Oded Hod, Juan E. Peralta, and Gustavo E. Scuseria. „Edge effects in finite elongated graphene nanoribbons.“ In: *Physical Review B* 76.23 (2007), p. 233401. DOI: 10.1103/PhysRevB.76.233401.

[149] Jochen Heyd, Gustavo E. Scuseria, and Matthias Ernzerhof. „Hybrid functionals based on a screened Coulomb potential.“ In: *The Journal of Chemical Physics* 118.18 (2003), pp. 8207–8215. DOI: 10.1063/1.1564060.

[150] Jochen Heyd, Gustavo E. Scuseria, and Matthias Ernzerhof. „Erratum: “Hybrid functionals based on a screened Coulomb potential” [J. Chem. Phys.118, 8207 (2003)].“ In: *The Journal of Chemical Physics* 124.21 (2006), p. 219906. DOI: 10.1063/1.2204597.

[151] Hajo Söde, Leopold Talirz, et al. „Electronic band dispersion of graphene nanoribbons via Fourier-transformed scanning tunneling spectroscopy.“ In: *Physical Review B* 91.4 (2015), p. 045429. DOI: 10.1103/PhysRevB.91.045429.

[152] Akihito Konishi, Yasukazu Hirao, et al. „Synthesis and Characterization of Quarteranthene: Elucidating the Characteristics of the Edge State of Graphene Nanoribbons at the Molecular Level.“ In: *Journal of the American Chemical Society* (2013). DOI: 10.1021/ja309599m.

[153] Katsunori Wakabayashi, Susumu Okada, et al. „Edge States and Flat Bands of Graphene Nanoribbons with Edge Modification.“ In: *Journal of the Physical Society of Japan* 79.3 (2010), p. 034706. DOI: 10.1143/JPSJ.79.034706.

[154] Mari Ijäs, Mikko Ervasti, et al. „Electronic states in finite graphene nanoribbons: Effect of charging and defects.“ In: *Physical Review B* 88.7 (2013), p. 075429. DOI: 10.1103/PhysRevB.88.075429.

[155] Paolo Giannozzi, Stefano Baroni, et al. „QUANTUM ESPRESSO: a modular and open-source software project for quantum simulations of materials.“ In: *Journal of Physics: Condensed Matter* 21.39 (2009), p. 395502. DOI: 10.1088/0953-8984/21/39/395502.

[156] Andrea Dal Corso. „Pseudopotentials periodic table: From H to Pu.“ In: *Computational Materials Science* 95 (2014), pp. 337–350. DOI: 10.1016/j.commatsci.2014.07.043.

[157] Denis A Areshkin and Carter T White. „Building Blocks for Integrated Graphene Circuits.“ In: (2007).

[158] D. Gunlycke, D. A. Areshkin, and C. T. White. „Semiconducting graphene nanostrips with edge disorder.“ In: *Applied Physics Letters* 90.14 (2007), p. 142104. DOI: 10.1063/1.2718515.

[159] Zhengfei Wang, Qunxiang Li, et al. „Tuning the electronic structure of graphene nanoribbons through chemical edge modification: A theoretical study.“ In: *Physical Review B* 75.11 (2007), p. 113406. DOI: 10.1103/PhysRevB.75.113406.

[160] Carlo Rozzi, Daniele Varsano, et al. „Exact Coulomb cutoff technique for supercell calculations.“ In: *Physical Review B* 73.20 (2006), p. 205119. DOI: 10.1103/PhysRevB.73.205119.

[161] Li Yang, Cheol-Hwan Park, et al. „Quasiparticle Energies and Band Gaps in Graphene Nanoribbons.“ In: *Physical Review Letters* 99.18 (2007), p. 186801. DOI: 10.1103/PhysRevLett.99.186801.

[162] Jack Deslippe, Georgy Samsonidze, et al. „BerkeleyGW: A massively parallel computer package for the calculation of the quasiparticle and optical properties of materials and nanostructures.“ In: *Computer Physics Communications* 183.6 (2012), pp. 1269–89. DOI: 10.1016/j.cpc.2011.12.006.

[163] Jack Deslippe, Georgy Samsonidze, et al. „Coulomb-hole summations and energies for GW calculations with limited number of empty orbitals: A modified static remainder approach.“ In: *Physical Review B* 87.16 (2013), p. 165124. DOI: 10.1103/PhysRevB.87.165124.

[164] Paolo E. Trevisanutto, Christine Giorgetti, et al. „Ab Initio GW Many-Body Effects in Graphene.“ In: *Physical Review Letters* 101.22 (2008), p. 226405. DOI: 10.1103/PhysRevLett.101.226405.

[165] Jeff Neaton, Mark Hybertsen, and Steven Louie. „Renormalization of Molecular Electronic Levels at Metal-Molecule Interfaces.“ In: *Physical Review Letters* 97.21 (2006), p. 216405. DOI: 10.1103/PhysRevLett.97.216405.

[166] Christoph Freysoldt, Patrick Rinke, and Matthias Scheffler. „Controlling Polarization at Insulating Surfaces: Quasiparticle Calculations for Molecules Adsorbed on Insulator Films.“ In: *Physical Review Letters* 103.5 (2009), p. 056803. DOI: 10.1103/PhysRevLett.103.056803.

[167] Juan M. Garcia-Lastra and Kristian S. Thygesen. „Renormalization of Optical Excitations in Molecules near a Metal Surface.“ In: *Physical Review Letters* 106.18 (2011), p. 187402. DOI: 10.1103/PhysRevLett.106.187402.

[168] Xueping Jiang, Neerav Kharche, et al. „Giant quasiparticle bandgap modulation in graphene nanoribbons supported on weakly interacting surfaces.“ In: *Applied Physics Letters* 103.13 (2013), p. 133107. DOI: 10.1063/1.4822427.

[169] Yan Li, Deyu Lu, and Giulia Galli. „Calculation of Quasi-Particle Energies of Aromatic Self-Assembled Monolayers on Au(111).“ In: *Journal of Chemical Theory and Computation* 5.4 (2009), pp. 881–6. DOI: 10.1021/ct800465f.

[170] Lukas Bürgi, Harald Brune, et al. „Quantum coherence and lifetimes of surface-state electrons.“ In: *Journal of Electron Spectroscopy and Related Phenomena* 109.1-2 (2000), pp. 33–49. DOI: 10.1016/S0368-2048(00)00105-5.

[171] Anders Bergvall and Tomas Löfwander. „Spectral footprints of impurity scattering in graphene nanoribbons.“ In: *Physical Review B* 87.20 (2013), p. 205431. DOI: 10.1103/PhysRevB.87.205431.

[172] Eva Y. Andrei, Guohong Li, and Xu Du. „Electronic properties of graphene: a perspective from scanning tunneling microscopy and magnetotransport.“ In: *Reports on progress in physics* 75.5 (2012), p. 056501. DOI: 10.1088/0034-4885/75/5/056501.

[173] Gilles Buchs, Dario Bercioux, et al. „Electron Scattering in Intrananotube Quantum Dots.“ In: *Physical Review Letters* 102.24 (2009), p. 245505. DOI: 10.1103/PhysRevLett.102.245505.

[174] Alexander V. Balatsky, Ilya Vekhter, and Jian-Xin Zhu. „Impurity-induced states in conventional and unconventional superconductors.“ In: *Reviews of Modern Physics* 78.2 (2006), pp. 373–433. DOI: 10.1103/RevModPhys.78.373.

[175] Dario Bercioux, Gilles Buchs, et al. „Defect-induced multicomponent electron scattering in single-walled carbon nanotubes.“ In: *Physical Review B* 83.16 (2011), p. 165439. DOI: 10.1103/PhysRevB.83.165439.

[176] Min Wang and Chang Ming Li. „Excitonic properties of hydrogen saturation-edged armchair graphene nanoribbons.“ In: *Nanoscale* 3.5 (2011), pp. 2324–8. DOI: 10.1039/c1nr10095e.

[177] Shiyong Wang, Weihua Wang, and Nian Lin. „Emergence of localized in-gap states in conjugated polymers of branched topology.“ In: *Physical Review B* 86.4 (2012), p. 045428. DOI: 10.1103/PhysRevB.86.045428.

[178] Yan Sun, Henrik Mortensen, et al. „From tunneling to point contact: Correlation between forces and current.“ In: *Physical Review B* 71.19 (2005), p. 193407. DOI: 10.1103/PhysRevB.71.193407.

[179] Markus Ternes, César González, et al. „Interplay of Conductance, Force, and Structural Change in Metallic Point Contacts.“ In: *Physical Review Letters* 106.1 (2011), p. 016802. DOI: 10.1103/PhysRevLett.106.016802.

[180] Yen-Chia Chen, Ting Cao, et al. „Molecular bandgap engineering of bottom-up synthesized graphene nanoribbon heterojunctions.“ In: *Nature Nanotechnology* 10.2 (2015), pp. 156–160. DOI: 10.1038/nnano.2014.307.

[181] Oliver Gröning. *Private Communication.* 2014.

[182] Haiming Zhang, Haiping Lin, et al. „On-Surface Synthesis of Rylene-Type Graphene Nanoribbons.“ In: *Journal of the American Chemical Society* 137.12 (2015), pp. 4022–4025. DOI: 10.1021/ja511995r.

[183] Hong Lin, Jérôme Lagoute, et al. „Many-body effects in electronic bandgaps of carbon nanotubes measured by scanning tunnelling spectroscopy.“ In: *Nature Materials* 9.3 (2010), pp. 235–238. DOI: 10.1038/nmat2624.

[184] Kai-Felix Braun and Karl-Heinz Rieder. „Engineering Electronic Lifetimes in Artificial Atomic Structures.“ In: *Physical Review Letters* 88.9 (2002), p. 096801. DOI: 10.1103/PhysRevLett.88.096801.

[185] Lukas E. M. Steinkasserer, Beate Paulus, and Elena Voloshina. „Impact of the metal substrate on the electronic structure of armchair graphene nanoribbons.“ In: *Chemical Physics Letters* 597.111 (2014), pp. 148–152. DOI: 10.1016/j.cplett.2014.02.038.

[186] Michael Golor, Cornelie Koop, et al. „Magnetic Correlations in Short and Narrow Graphene Armchair Nanoribbons.“ In: *Physical Review Letters* 111.8 (2013), p. 085504. DOI: 10.1103/PhysRevLett.111.085504.

[187] Yan Li, Wei Zhang, et al. „Electronic and Magnetic Properties of Zigzag Graphene Nanoribbons on the (111) Surface of Cu, Ag, and Au.“ In: *Physical Review Letters* 110.21 (2013), p. 216804. DOI: 10.1103/PhysRevLett.110.216804.

[188] Aron J. Cohen, Paula Mori-Sánchez, and Weitao Yang. „Insights into current limitations of density functional theory.“ In: *Science (New York, N.Y.)* 321.5890 (2008), pp. 792–4. DOI: 10.1126/science.1158722.

[189] Stefan Grimme. „Semiempirical GGA-type density functional constructed with a long-range dispersion correction.“ In: *Journal of computational chemistry* 16 (2006). DOI: 10.1002/jcc.20495.

[190] Shiyong Wang, Leopold Talirz, et al. „Edge state splitting at atomically precise graphene zigzag edges.“ Submitted.

[191] Christian Hartwigsen, Stefan Goedecker, and Jürg Hutter. „Relativistic separable dual-space Gaussian pseudopotentials from H to Rn.“ In: *Physical Review B* 58.7 (1998), pp. 3641–3662. DOI: 10.1103/PhysRevB.58.3641.

[192] Glenn J. Martyna and Mark E. Tuckerman. „A reciprocal space based method for treating long range interactions in ab initio and force-field-based calculations in clusters.“ In: *The Journal of Chemical Physics* 110.6 (1999), pp. 2810–2821. DOI: 10.1063/1.477923.

[193] John P. Perdew and Mel Levy. „Physical content of the exact Kohn-Sham orbital energies: Band gaps and derivative discontinuities.“ In: *Physical Review Letters* 51.6 (1983), pp. 1884–1887. DOI: 10.1103/PhysRevLett.51.1884.

[194] Carsten Rostgaard, Karsten W. Jacobsen, and K. S. Thygesen. „Fully self-consistent GW calculations for molecules.“ In: *Physical Review B* 81.8 (2010), p. 085103. DOI: 10.1103/PhysRevB.81.085103.

[195] Meng-Sheng Liao and Steve Scheiner. „Electronic structure and bonding in metal phthalocyanines, Metal=Fe, Co, Ni, Cu, Zn, Mg.“ In: *The Journal of Chemical Physics* 114.22 (2001), pp. 9780–9791. DOI: 10.1063/1.1367374.

[196] Lu J. Sham and Michael Schlüter. „Density-Functional Theory of the Energy Gap.“ In: *Physical Review Letters* 51.20 (1983), pp. 1888–91. DOI: 10.1103/PhysRevLett.51.1888.

[197] Rex W. Godby and Ian D. White. „Density-Relaxation Part of the Self-Energy.“ In: *Physical Review Letters* 80.14 (1998), pp. 3161–3161. DOI: 10.1103/PhysRevLett.80.3161.

[198] Xavier Blase, Claudio Attaccalite, and Valerio Olevano. „First-principles GW calculations for fullerenes, porphyrins, phtalocyanine, and other molecules of interest for organic photovoltaic applications.“ In: *Physical Review B* 83.11 (2011), p. 115103. DOI: 10.1103/PhysRevB.83.115103.

[199] Jascha Repp, Gerhard Meyer, et al. „Molecules on Insulating Films: Scanning-Tunneling Microscopy Imaging of Individual Molecular Orbitals.“ In: *Physical Review Letters* 94.2 (2005), p. 026803. DOI: 10.1103/PhysRevLett.94.026803.

[200] Bjørk Hammer and Jens K. Norskov. „Why gold is the noblest of all the metals.“ In: *Nature* 376.6537 (1995), pp. 238–240. DOI: 10.1038/376238a0.

[201] Chenggang Tao, Liying Jiao, et al. „Spatially resolving edge states of chiral graphene nanoribbons.“ In: *Nature Physics* 7.8 (2011), pp. 616–620. DOI: 10.1038/nphys1991.

[202] Gábor Zsolt Magda, Xiaozhan Jin, et al. „Room-temperature magnetic order on zigzag edges of narrow graphene nanoribbons.“ In: *Nature* 514.7524 (2014), pp. 608–11. DOI: 10.1038/nature13831.

[203] Paula Mori-Sánchez and Aron J. Cohen. „The derivative discontinuity of the exchange-correlation functional.“ In: *Physical Chemistry Chemical Physics* 16.28 (2014), p. 14378. DOI: 10.1039/c4cp01170h.

[204] Pascal Ruffieux, Shiyong Wang, et al. „On-surface synthesis of graphene nanoribbons with zigzag edge topology.“ Submitted.

[205] Jinming Cai, Carlo A. Pignedoli, et al. „Graphene nanoribbon heterojunctions.“ In: *Nature Nanotechnology* 9.11 (2014), pp. 896–900. DOI: 10.1038/nnano.2014.184.

[206] Leopold Talirz, Prashant Shinde, et al. „Synthesis of Atomically Precise Graphene-Based Nanostructures: a Simulation Point of View.“ In: *On-Surface Synthesis*. Ed. by Christian Joachim. Vol. 8. Advances in Atom and Single Molecule Machines. Springer (in press).

[207] Carlos Sánchez-Sánchez, Sebastian Brüller, et al. „On-Surface Synthesis of BN-Substituted Heteroaromatic Networks.“ In: *ACS Nano* 9.9 (2015), pp. 9228–9235. DOI: 10.1021/acsnano.5b03895.

[208] Leopold Talirz, Hajo Söde, et al. „Band gap of atomically precise graphene nanoribbons as a function of ribbon length and termination.“ In preparation.

APPENDIX A

Band gap of finite AGNRs in tight binding

In the following, we adopt the notation used in reference [97] for zigzag GNRs. It is related to the notation used elsewhere in this thesis by

$$\begin{array}{rcl} k & \leftrightarrow & k_x a_{zz} = r\frac{2\pi}{M+1} \\ p & \leftrightarrow & k_y \frac{a_{ac}}{2} := s\frac{\pi}{N+\delta} \end{array} \tag{A.1}$$

We focus on monohydrogenated armchair graphene nanoribbons of sufficient length, i.e. large N, and would like to derive an analytic expression for the wave vector p_1 along the armchair direction that corresponds to the highest occupied and lowest unoccupied molecular orbital. Since the electronic gap of armchair GNRs is always located at Γ ($p = 0$), p_1 will be small for large N.

The transcendental equation for p is given by [97]

$$0 = \sin[pN] + g_k \sin[p(N+1)] \tag{A.2}$$

$$= \sin[pN] + g_k \left(\sin[pN] + \cos[pN]p\right) + O(p^2) \tag{A.3}$$

where $g_k = 2\cos(\frac{k}{2})$.

The case $g_k = -1$ occurs for $\frac{r}{M+1} \in \{\frac{1}{3}, \frac{2}{3}\}$, which is possible if and only if the GNRs belong to the metallic family with $M = 3m - 1$. Apart from the unphysical solution $p = 0$, one finds the solutions

$$p = \left(s - \frac{1}{2}\right)\frac{\pi}{N}, \quad s \in \{1 \ldots N\},\, s \ll N \quad M = 3m-1 \tag{A.4}$$

For $g_k \neq 1$, we choose to write $p := s\frac{\pi}{N+\delta}, s \in \{1, \ldots, N\}$ with an unknown δ. Assuming δ to be finite, we have $pN = s\pi - sp\delta = s\pi + O(p)$. Equation

(A.3) simplifies to

$$\begin{aligned} 0 &= \sin[pN] + g_k\left(\sin[pN] + \cos[pN]p\right) + O(p^2) \\ &= (-1)^s(pN - s\pi) + g_k\left((-1)^s(pN - s\pi) + (-1)^s p\right) + O(p^2) \\ &= pN(1+g_k) - s\pi(1+g_k) + pg_k + O(p^2) \\ \Rightarrow p &= s\frac{\pi}{N + \frac{g_k}{1+g_k}} + O(p^2) \end{aligned} \tag{A.5}$$

We identify $\delta = \frac{g_k}{1+g_k}$.

From equation (A.5), we obtain the desired wave vector p_1 by setting $s = 1$. By plugging p_1 into the graphene dispersion $E(k, p)$, we obtain an approximation for the length-dependent band gap

$$\Delta(k, p_1) = 2t\sqrt{1 + g_k^2 + 2g_k\cos(p_1)} \tag{A.6}$$

$$= 2t\left(|1+g_k| - \frac{g_k\pi^2}{2|1+g_k|}\frac{1}{N^2}\right) + O\left(\frac{1}{N^3}\right) \tag{A.7}$$

$$= 2t\left(|1+g_k| - \frac{g_k\pi^2}{2|1+g_k|}\frac{1}{(N+\delta)^2}\right) + O\left(\frac{1}{(N+\delta)^4}\right) \tag{A.8}$$

for $N \to \infty$, i.e., the expansion in $1/(N+\delta)$ is more rapidly convergent.

As noted in formula (2.60), valence and conduction band are selected by $r = 2m + 1$ for AGNRs of the semiconducting families with widths $M = 3m$ and $M = 3m+1$. For $m \geq 1$, we therefore have $g_k = 2\cos\left[(2m+1)\frac{2\pi}{M+1}\right] < 0$ and thus $\Delta(N, \delta) \approx a + b/(N+\delta)^2$ with $a > 0,\ b > 0$.

For the length δ, we find

$$\delta = \begin{cases} \left[1 + 1/\left(2\cos\left[\frac{2m+1}{3m+1}\pi\right]\right)\right]^{-1} > 0 & M = 3m \\ \left[1 + 1/\left(2\cos\left[\frac{2m+1}{3m+2}\pi\right]\right)\right]^{-1} \leq 0 & M = 3m+1 \end{cases} \tag{A.9}$$

Within each family, $|\delta|$ increases monotonously with increasing width of the armchair GNR. More specifically, $|\delta| = \frac{3\sqrt{3}}{\pi}m + O(1)$ for $m \to \infty$. I.e., the wider the GNR, the more strongly the "effective electronic length" $L = (N+\delta)\frac{a_{ac}}{2}$ for valence and conduction band deviates from the geometric length $N\frac{a_{ac}}{2}$.

For the 7-AGNR, we have $m = 2$ and $g_k = 2\cos\left[\frac{5}{8}\pi\right] \approx -0.765$. We find

$$\delta = \frac{g_k}{1+g_k} \approx -3.26 \tag{A.10}$$

$$\Delta(N) \approx 2t\left(0.470 + \left(\frac{4.01}{N+\delta}\right)^2\right) \tag{A.11}$$

APPENDIX B

Fourier transform of the local density of states

B.1 Particles in a box

In the Tersoff-Hamann approximation, scanning tunneling spectroscopy probes the local density of states of the sample. When aiming to determine band structures, however, this still leaves the task of extracting the crystal wave vector k of the Bloch states that give rise to the LDOS.

To first approximation, the electrons in a finite GNR may be described as particles in a box. Assuming for the moment that the influence due to the particular boundary conditions at the termini can be neglected, the states of a finite GNR with length L are obtained from the Bloch states[1] $\psi_{n,k}(x) = u_{n,k}(x)e^{ikx}$ of the infinite periodic crystal by introducing hard-wall boundary conditions at positions $x = 0, \pm L, \pm 2L, \ldots$

This gives rise to a discretization of the crystal wave vector to values $k = m\frac{\pi}{L}$, $m \in \mathbb{N}$. Furthermore, it selects the linear combination of left- and right-moving Bloch states with nodes at the hard walls:

$$\varphi_{n,k}(x) = \frac{1}{\sqrt{2}i} u_{n,k}(x) \left(e^{+ikx} - e^{-ikx} \right) = \sqrt{2} u_{n,k}(x) \sin(kx) \tag{B.1}$$

The standing wave (B.1) gives rise to a density

$$\rho_k(x) = |\varphi_{n,k}(x)|^2 = u_{n,k}^2(x) \left(1 - \cos(2kx)\right) \tag{B.2}$$

[1] $u_{n,k}(x+a) = u_{n,k}(x)$ shares the periodicity of the crystal lattice with lattice constant a. For armchair and zigzag GNRs, time-reversal symmetry yields $u^*_{n,k}(x) = u_{n,-k}(x)$ and left-right symmetry yields $u_{n,-k}(x) = u_{n,k}(x)$. The lattice-periodic function $u_{n,k}(x)$ is therefore real-valued.

In the following, just a single band is considered for simplicity and, accordingly, the index n is dropped.

We now aim to retrieve the wave vector k from $\rho_k(x)$ by performing a Fourier transform (FT). Since $\rho_k(x)$ is a product involving the lattice-periodic function $u_k(x)$, we make use of the fact that $\mathcal{F}[f \cdot g] = \mathcal{F}[f] * \mathcal{F}[g]$, where $*$ denotes the convolution, and obtain

$$u_k(x) = \sum_G \hat{u}_{k,G} e^{iGx} \tag{B.3}$$

$$u_k^2(x) = \sum_G \left(\sum_{G'} \hat{u}_{k,G'} \hat{u}_{k,G'-G} \right) e^{iGx} \quad , \tag{B.4}$$

$$\text{where} \quad \hat{u}_{k,G} = \frac{1}{2\pi} \int_0^L u_k(x) e^{-iGx}\, dx \quad . \tag{B.5}$$

For the second term, we have

$$\mathcal{F}[1 - \cos(2kx)](q) = \begin{cases} 1 & q = 0 \\ -1 & |q| = 2k \\ 0 & \text{otherwise} \end{cases} \tag{B.6}$$

and thus obtain

$$\hat{\rho}_k(q) := \mathcal{F}[\rho_k](q) = \begin{cases} \sum_{G'} \hat{u}_{k,G'} \hat{u}_{k,G'-G} & q = G \\ -\sum_{G'} \hat{u}_{k,G'} \hat{u}_{k,G'-G} & q \pm 2k = G \end{cases} \tag{B.7}$$

The Fourier transform $\hat{\rho}_k(q)$ of the charge density differs from zero only, when either q or $q \pm 2k$ coincide with a reciprocal lattice vector $G = r\frac{2\pi}{a}$. Here, $r \in \mathbb{Z}$ and a is the lattice parameter.

For $G = 0$, one obtains $|\hat{\rho}_k(q)| = \sum_{G'} \hat{u}_{k,G'} \hat{u}_{k,G'} = \frac{1}{2\pi} \int \rho_k(x) dx$, which is simply the integral of the charge density. Since this integral is necessarily non-vanishing, the positions of the side-peaks at $q = 0 \pm 2k$ can be used to extract the wave vector k of the underlying Bloch state $\psi_k(x)$.[2]

Whether $|\hat{\rho}_k(q)|$ will be significant when q or $q \pm 2k$ coincide with *finite* reciprocal lattice vectors G, depends on the particular shape of $u_k(x)$ – specifically, on the Fourier component $\mathcal{F}\left[u_k^2\right](G)$. Figure B.1 shows an example of $\mathcal{F}\left[u_k^2\right](G)$ for the valence band of the $M = 7$ AGNR, as obtained within DFT using the PBE functional. The $G = 0$ coefficient clearly dominates, but contributions from finite G can be significant, in particular with increasing tip-sample distance.

Note that the above analysis is generalized to multiple overlapping bands in a straight-forward manner. In the picture of independent particles that is

[2] When $\mathcal{F}[\rho_{nk}](q)$ is plotted against $k = \frac{q}{2}$ (for comparison with band structures), the next copy of the 3-stencil appears already at $k = \frac{G}{2}$.

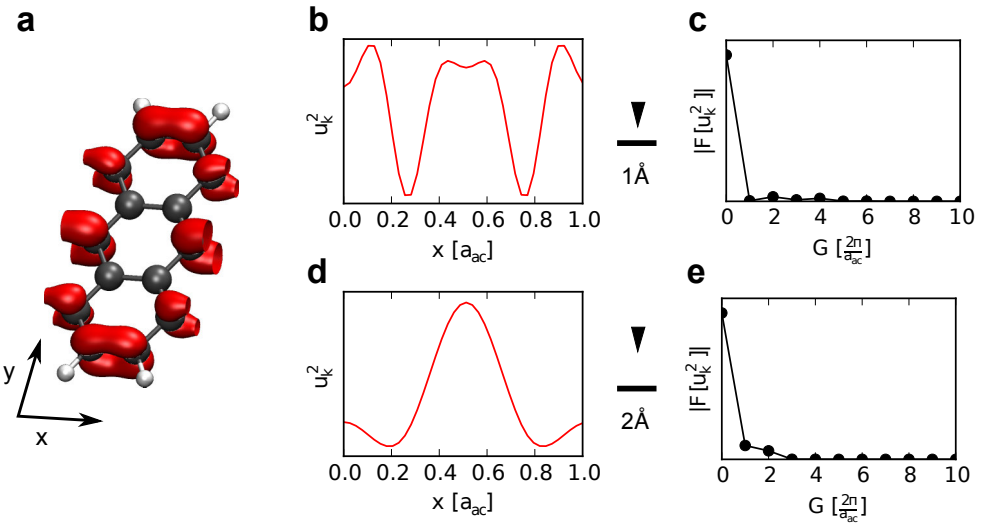

Figure B.1: Fourier components of lattice-periodic function u_k. (a) Isosurface of $u_k^2(\mathbf{r})$ corresponding to the valence band of the $M = 7$ AGNR at $k = 0$. (b-c) Plotted are $u_k^2(x) = \int_y u_k^2(x, y, z_0)\, dy$ and $\mathcal{F}[u_k^2](G)$ for $z_0 = 1\,\text{Å}$ above the atoms. (d-e) As (b-c), but for $z_0 = 2\,\text{Å}$ above the atoms.

considered here, additional bands simply give rise to a superposition of the electron densities corresponding to the individual states.[3] Since the Fourier transform is a linear operator, the superposition principle also holds in momentum space.[4]

B.2 Realistic systems

If the boundary conditions at the termini of finite GNRs were hard walls, separated by the geometric length L of the GNR, the approach outlined in the previous section would provide direct access to the band structure of the infinite GNR.

However, this is an approximation. First, as discussed in chapter 4, the boundary conditions at the termini can be viewed as giving rise to an effective length $L + \delta'$, where the shift δ' depends both on the band index n and the atomic structure of the terminus. And second, the potential well that confines the electrons to the finite GNR is not infinitely deep. The tails of the elec-

[3] Recall that the electron density corresponding to the Slater determinant of a set of Bloch states $\{\psi_{n,k}(x)\}$ is given by $\rho(x) = \sum_{n,k} |\psi_{n,k}(x)|^2$.

[4] Care must still be taken in the interpretation of spectra, since the superposition principle does *not* hold for the *absolute value* of the Fourier transform, which is the quantity that is usually plotted.

tronic states penetrate the potential barrier, and penetration depth generally increases with increasing eigenenergy of the state.

Due to both of these factors, the wave vectors k that best describe the standing waves of the finite GNR do not necessarily fall onto the frequency grid defined by $k = \frac{q}{2} = r\frac{\pi}{L}$, $r \in \mathbb{Z}$. In chapter 5, this fact is taken into consideration by repeating the dispersion analysis for varying widths W of the window chosen for the Fourier series and incorporating the corresponding deviations into the error bars of extracted quantities. The advantage of this option lies in the simplicity of the interpretation of each calculated Fourier series, which can be borrowed from the picture of particles in a box.

An alternative option is to present the Fourier *transform* of an isolated GNR, surrounded by an infinite amount of vacuum. The advantage of this option is that no choice is required and all possible wave vectors can be realized.

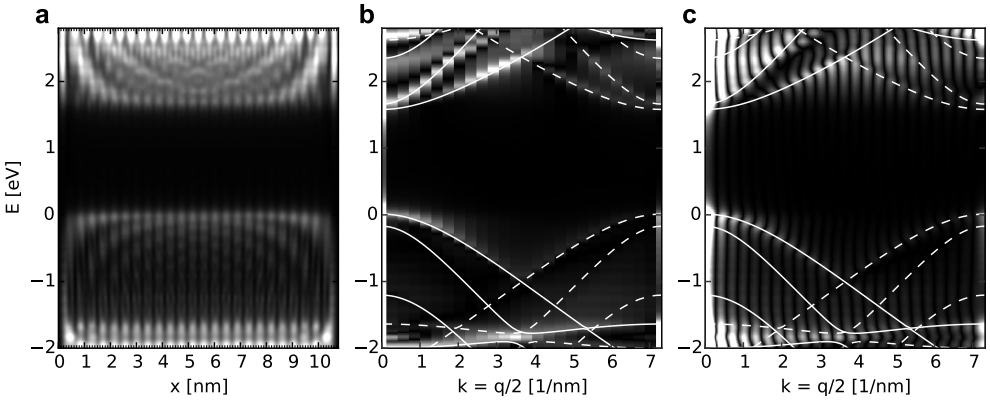

Figure B.2: Comparing Fourier series and Fourier transform. (a) LDOS along CH_2-terminated 7-AGNR at $z = 4\,\text{Å}$ above the GNR. (b) Fourier series of periodically repeated LDOS (a). (c) Fourier transform of LDOS (a) surrounded by vacuum. The band structure of the periodic GNR is indicated by white lines (centered at $k = 0$) and dashed white lines (centered at $k = \pi/a_{ac}$).

Figure B.2 compares both options. The process of going from a (fake) periodic system with period L to an isolated system of length L can be described by multiplication with a rectangular function:

$$\rho_{nk}(x) \to \rho_{nk}(x)\Pi\left(\frac{x}{L}\right) \quad , \tag{B.8}$$

$$\text{where} \quad \Pi(x) = \begin{cases} 1 & |x| < \frac{1}{2} \\ \frac{1}{2} & |x| = \frac{1}{2} \\ 0 & |x| > \frac{1}{2} \end{cases} \quad . \tag{B.9}$$

The Fourier transform of the isolated system is then obtained by folding

the Fourier series $\mathcal{F}[\rho_{nk}](q)$ of the periodic system with

$$\mathcal{F}[\Pi](q) = \sqrt{\frac{L}{2\pi}} \frac{\sin\left(q\frac{L}{2}\right)}{\pi\frac{qL}{2}} \tag{B.10}$$

This results in a broadening of width $\approx \frac{2\pi}{L}$, as well as the appearance of side peaks, spaced by $\approx \frac{2\pi}{L}$. As illustrated by Figure B.2 (c), however, the extraction of the band structure from the Fourier transform is less straightforward. For this reason, the first option has been adopted in chapter 5.

On a final note, it would seem tempting to eliminate the influence of boundary effects simply by investigating very long GNRs. Unfortunately, this does not solve the problem: The finite life time (and corresponding energetic broadening) of states gives rise to an exponential decay of the variations in the LDOS with increasing distance from the potential barrier [170]. In the cases studied here, this limits the useful signal to a range of a few nm near the terminus.

APPENDIX C

Decay of local density of states

C.1 Paraxial approximation

In deriving the equations for the extrapolation of wave functions (chapter 2.5.3), assumptions have been made only about the shape of the potential $V(\mathbf{r})$, which the wave functions are subjected to in the Schrödinger equation.

The extrapolation starts from the values of the wave function $\chi_\nu(x, y, z)$ on a plane $z = z_0$. Using a notation for non-periodic systems, the in-plane Fourier components are given by

$$\chi_\nu(k_x, k_y; z_0) = \frac{1}{(2\pi)^2} \int \chi_\nu(x, y, z_0) e^{-ik_x x - ik_y y}\, dx\, dy \quad . \tag{C.1}$$

From $\chi_\nu(k_x, k_y; z_0)$, the wave function for all $z > z_0$ is obtained by the inverse Fourier transform

$$\chi_\nu(x, y, z) = \int \chi_\nu(k_x, k_y; z_0) e^{-\kappa(z-z_0)} e^{ik_x x + ik_y y}\, dk_x\, dk_y \tag{C.2}$$

$$\text{where} \quad \kappa = \sqrt{k_x^2 + k_y^2 - \frac{2m}{\hbar^2}(E_\nu - V_0)} \quad . \tag{C.3}$$

Equation (C.2) states that Fourier components corresponding to larger in-plane wave vectors $\mathbf{k} = (k_x, k_y)$ decay faster with increasing z than those corresponding to shorter wave vectors. It is therefore clear that sharp oscillations are damped more strongly than smooth variations of $\chi_\nu(\mathbf{r})$.

However, this analysis relies on the concept of reciprocal space and it can be helpful to develop an alternative view based completely in real space. In

this respect, it is instructive to consider the limit

$$k_x^2 + k_y^2 \ll \frac{2m}{\hbar^2} |E_\nu - V_0| =: \kappa_\nu^2 \quad , \tag{C.4}$$

$$\text{yielding} \quad \kappa \approx \kappa_\nu \left(1 + \frac{k_x^2 + k_y^2}{2\kappa_\nu^2} \right) \quad . \tag{C.5}$$

For waves propagating in all directions, this limit is commonly known as the *paraxial* or *Fresnel* approximation. In the paraxial approximation, $\chi_\nu(k_x, k_y; z)$ assumes the form of a Gaussian function in k_x, k_y and the inverse Fourier transform (C.2) can be rewritten as a real-space integral

$$\chi_\nu(x, y, z) = \int \chi_\nu(x - x', y - y', z_0)\, h(x', y', z - z_0)\, dx'\, dy' \quad , \tag{C.6}$$

$$\text{where} \quad h(x, y, z) = \frac{\kappa_\nu}{2\pi z} \exp\left(-\kappa_\nu z \left(1 + \frac{x^2 + y^2}{2z^2} \right) \right) \tag{C.7}$$

is the impulse response function of free space.

Apart from prefactors, $h(x, y, z)$ has the form of a Gaussian

$$g(x, y) = \frac{1}{\sqrt{2\pi}\sigma} \exp\left(-\frac{x^2 + y^2}{2\sigma^2} \right) \tag{C.8}$$

with standard deviation $\sigma = \sqrt{z/\kappa_\nu}$. Besides a general attenuation, the effect of increasing distance from $z = z_0$ to $z_0 + \Delta z$ is therefore equivalent to a two-dimensional Gaussian filtering with standard deviation $\sqrt{\Delta z/\kappa_\nu}$.

Figure C.1 shows an example comparing the extrapolation performed via the inverse Fourier transform (C.2) to the paraxial approximation (C.5). For wave vectors that violate the assumption $k_x^2 + k_y^2 \ll \kappa_\nu^2$, the paraxial approximation overestimates κ, leading to an over-attenuation of Fourier components at large wave vectors. For practical purposes, however, the agreement can be considered quite acceptable.

C.2 Symmetry of tight binding wave function

The unit cell of graphene contains two carbon atoms and we label the corresponding carbon sublattices by A and B. In the single-orbital nearest-neighbor tight binding model of graphene's π-electronic structure, the wave function on the two sublattices is given by [97]

$$\psi_{\mathbf{k}} \quad = \quad \begin{pmatrix} \psi_{\mathbf{n},A} \\ \psi_{\mathbf{n},B} \end{pmatrix} = \begin{pmatrix} 1 \cdot e^{i\mathbf{k}(\mathbf{r_n} + \mathbf{r}_A)} \\ -s e^{i\varphi(\mathbf{k})} e^{i\mathbf{k}(\mathbf{r_n} + \mathbf{r}_B)} \end{pmatrix} \tag{C.9}$$

where $\mathbf{r_n}$ is the position of the unit cell, $\mathbf{r}_A, \mathbf{r}_B$ are the positions of the respective carbon atom within the unit cell and

$$\varphi(\mathbf{k}) = \arg\left(\sum_{l=1}^{3} e^{-i\mathbf{k}\tau_l} \right) \tag{C.10}$$

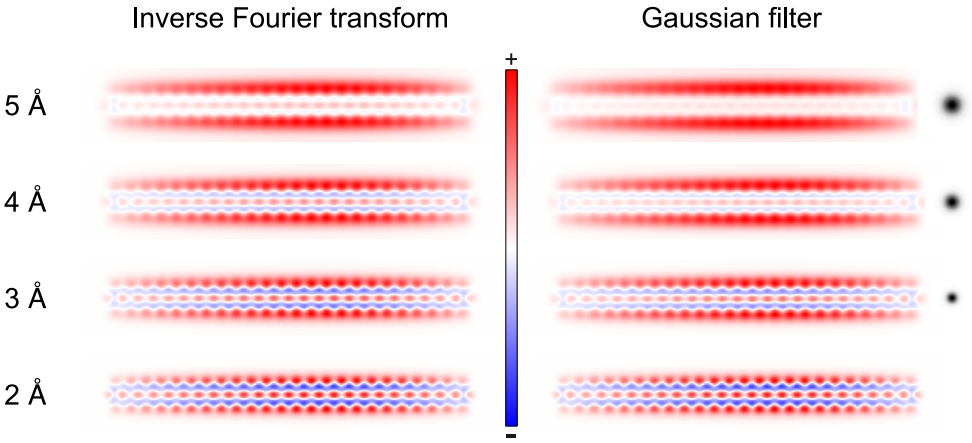

Figure C.1: Comparing wave function extrapolation via inverse Fourier transform (C.2) and Gaussian filtering (C.7). Both methods use the same starting point: the HOMO of a finite 7-AGNR, evaluated at a plane positioned 2Å above the GNR. The color scale is adapted to the full range of each plot, while remaining symmetric with respect to 0. A grayscale plot of the Gaussian function used for filtering is shown next to the filtered images ($\kappa_\nu \approx 1.1/\text{Å}$).

with vectors τ_l as indicated in Figure C.2. The sign s equals $+1$ for the empty states and -1 for the occupied states.

As a side note, placing a p_z orbital $p_z(\mathbf{r}) \propto z e^{-\alpha|\mathbf{r}|}$ on each carbon site yields a corresponding real-space wave function

$$\psi_\mathbf{k}(\mathbf{r}) = e^{i\mathbf{kr}} u_\mathbf{k}(\mathbf{r}) \tag{C.11}$$

$$\text{with} \quad u_\mathbf{k}(\mathbf{r}) = \sum_\mathbf{n} \Big(p_z(\mathbf{r} - \mathbf{r}_A - \mathbf{r}_\mathbf{n}) - s e^{i\varphi(\mathbf{k})} p_z(\mathbf{r} - \mathbf{r}_B - \mathbf{r}_\mathbf{n}) \Big) \quad , \tag{C.12}$$

which allows to perform qualitative STS simulations on the tight binding level.

One question arising in chapter 5 concerns the relative phase of the wave function at sites along the armchair direction. In the tight binding model, the wave functions of periodic AGNRs are simply a standing wave obtained from the linear combination of two graphene eigenstates with wave vectors $\mathbf{k} = (\pm k_x, k_y)$. It is therefore sufficient to directly analyse the phase for the graphene eigenstates (C.9).

Figure C.2 shows two sites along an armchair direction, marked in red. According to equation, (C.9) the corresponding values of ψ are given by

$$\psi_B = -s e^{i\varphi(\mathbf{k})} e^{i\mathbf{kr}_B} \tag{C.13}$$

$$\psi_A = e^{i\mathbf{k}(\mathbf{r}_A + \mathbf{a}_2)} \tag{C.14}$$

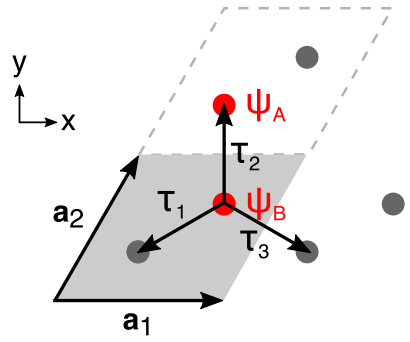

Figure C.2: Graphene lattice with unit cell, lattice vectors and definition of τ_1, τ_2, τ_3. The lattice sites considered in the text are denoted as ψ_A, ψ_B.

with ratio

$$\psi_B/\psi_A = -se^{i\varphi(\mathbf{k})} \underbrace{e^{i\mathbf{k}(\mathbf{r}_B - \mathbf{r}_A - \mathbf{a}_2)}}_{=1} \quad . \tag{C.15}$$

In the following, we restrict the discussion to the Γ-point of the Brillouin zone for armchair GNRs, which corresponds to $k_y = 0$ along the armchair direction. Writing

$$\varphi(\mathbf{k}) = \frac{f(\mathbf{k})}{|f(\mathbf{k})|}, \quad \text{where} \quad f(\mathbf{k}) = \sum_{l=1}^{3} e^{-i\mathbf{k}\tau_l}, \tag{C.16}$$

we obtain[1]

$$f(k_x, 0) = e^0 + e^{-ik_x a\sqrt{3}/2} + e^{ik_x a\sqrt{3}/2} = 1 + 2\cos(k_x a\sqrt{3}/2) \tag{C.17}$$

As discussed in chapter 2.4.2, confinement by armchair edges gives rise to a simple discretization of the transverse wave vector $k_x = \frac{r}{M+1}\frac{2\pi}{a_{zz}}$, where $a_{zz} = \sqrt{3}a$. Using this relation, we find

$$\psi_B/\psi_A = -s\,\mathrm{sgn}\left(1 + 2\cos\left(\frac{r}{M+1}\pi\right)\right) = \begin{cases} s, & \frac{r}{M+1} > \frac{2}{3} \\ -s, & \frac{r}{M+1} < \frac{2}{3} \end{cases} \tag{C.18}$$

For the Γ-point $k_y = 0$, we thus find only two possibilities: Either ψ simply remains constant along the armchair direction or its sign alternates between the two sublattices. For the valence and conduction bands of the different AGNR families, we obtain:

- $M = 3m$: We have $r = 2m + 1$ and $\frac{r}{M+1} > \frac{2}{3}$. Therefore, the occupied frontier orbitals change sign along the GNR, while the empty frontier orbitals do not.

[1] Note that $f(k_x, 0)$ is independent of the sign of k_x and thus identical for both eigenstates of the linear combination.

- $M = 3m+1$: $r = 2m+1$ yields $\frac{r}{M+1} < \frac{2}{3}$. The occupied frontier orbitals do *not* change sign along the GNR, while the empty frontier orbitals *do*.
- $M = 3m-1$: $r = 2m$ yields $\frac{r}{M+1} = \frac{2}{3}$ and equation (C.18) does not apply.

  Note, however, that (C.18) *does* apply to all bands *except* the valence and conduction band.

For $M = 3m-1$, the frontier bands at the Γ point of the armchair Brillouin zone arise from a linear combination of graphene eigenstates corresponding to the **K** point, i.e., the tip of the Dirac cone.

At $\mathbf{K} = (\pm\frac{4}{3}\frac{\pi}{\sqrt{3}}, 0)$, the relative phase of the graphene wave function on the two sublattices is completely arbitrary. In a finite AGNR, it is therefore determined exclusively by the boundary conditions at the terminus, making it necessary to take the finite size and the atomic structure at the terminus into consideration.

APPENDIX D

Broadening of the density of states

In one-dimensional periodic systems, such as graphene nanoribbons, band onsets are characterized by a van-Hove singularity in the density of states. In the following, the broadening of a van-Hove singularity is considered for three different types of broadening: Lorentzian, Lock-in and Gaussian.

The function

$$f(E) = \begin{cases} \frac{1}{\sqrt{E}} & E > 0 \\ 0 & E \leq 0 \end{cases} \quad , \tag{D.1}$$

represents the density of states for a band onset at $E = 0$. It is convoluted with a broadening function $g(E)$ in order to obtain the broadened density of states

$$h(E) = \int_{-\infty}^{\infty} f(E')g(E - E')\, dE' \quad . \tag{D.2}$$

Figure D.1 illustrates the convolution of $f(E)$ with a Lorentzian function of full-width Δ at half-maximum (FWHM). Note that the broadened density of states $h(E)$ assumes its maximum at $E = E_M$ *above* the band onset at $E = 0$, while the half-maximum is assumed at $E = E_{HM}$ *below* the band onset. This also holds for the other types of broadening considered here. The common conventions of using either the half-maximum or the maximum to mark the band onset in a scanning tunneling spectrum therefore both introduce a systematic bias.

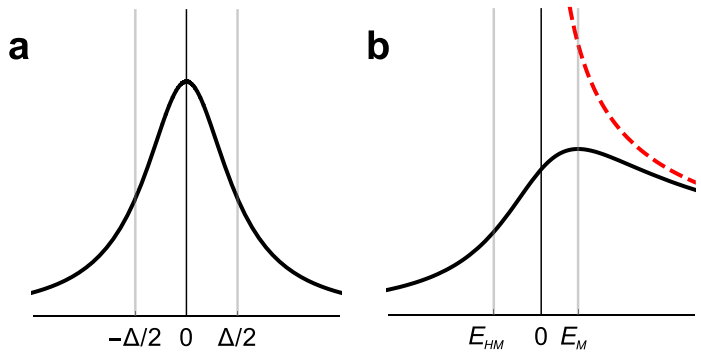

Figure D.1: (a) Lorentzian function with full-width Δ at half-maximum. (b) Convolution $h(E)$ (black) of van-Hove singularity $f(E)$ (dashed red) with Lorentzian. The positions of half-maximum (E_{HM}) and maximum (E_M) are indicated.

	Lorentzian	Lock-in	Gaussian
E_M [Δ]	+0.289	+0.377	+0.325
E_{HM} [Δ]	-0.371	-0.258	-0.296

Table D.1: Numerical values of positions E_M of the maximum and E_{HM} of the half-maximum of $h(E)$, given in units of the full-width at half-maximum Δ of the broadening function. Band onset is at $E = 0$.

The energies E_{HM}, E_M are proportional to the FWHM of the broadening function[1] and the corresponding proportionality factors are given in table D.1. The following sections provide mathematical details.

D.1 Lorentzian broadening

The coupling between molecules and the underlying substrate gives rise to a finite life time of excited states, leading to a Lorentzian broadening of the corresponding energy levels.

For a Lorentzian broadening

$$g(E) = \frac{1}{\pi}\frac{\Gamma}{2} / \left(E^2 + (\Gamma/2)^2\right) \tag{D.3}$$

[1] If $g(E, \Delta)$ denotes a broadening function with FWHM Δ, then $g(E, 1) \propto g(E\Delta, \Delta)$ and also $h(E, 1) \propto h(E\Delta, \Delta)$.

with FWHM $\Delta = \Gamma$, we obtain

$$\begin{aligned} h(E) &= \frac{1}{\sqrt{2}} \left(\frac{1}{\sqrt{2E + i\Gamma}} + \frac{1}{\sqrt{2E - i\Gamma}} \right) \\ &= \frac{\sqrt{1 + \mathrm{sgn}(E)/\sqrt{1 + (\Gamma/2E)^2}}}{\sqrt[4]{4E^2 + \Gamma^2}} \end{aligned}$$

which assumes its maximum at $E_M = \Gamma/(2\sqrt{3}) \approx 0.289\,\Delta$.

Half-maximum is assumed at

$$\begin{aligned} E_{HM} &= -\frac{1}{3}\sqrt{\frac{229}{12} + \frac{4}{3}\beta - \frac{4}{3}\sqrt{494 - 9/\alpha - 9\alpha + 7760/\beta}}\;\Gamma \\ \text{where} \quad \alpha &= \sqrt[3]{31 + 8\sqrt{15}} \quad \text{and} \\ \beta &= \sqrt{247 + 9/\alpha + 9\alpha} \end{aligned}$$

with numerical value $E_{HM} \approx -0.371\,\Delta$.

D.2 Lock-in broadening

Experimentally, the derivative of the tunneling current I with respect to the bias voltage V is approximated by the lock-in derivative

$$\frac{dI}{dV}(V, \delta V) \propto \int_0^{2\pi/\omega} \cos(\omega t)\, I\left(V + \frac{\delta V}{2}\cos(\omega t)\right) dt \tag{D.4}$$

The bias voltage V is modulated with a reference signal $\frac{\delta V}{2}\cos(\omega t)$ and the time-integral of the product between tunneling current $I(V)$ and reference signal is recorded. In the limit $\delta V \to 0$, the exact derivative $dI/dV(V)$ is recovered.

Setting $\omega = 1$ for convenience, the expression for $\frac{dI}{dV}(V, \delta V)$ can be transformed into a convolution of the exact derivative $\frac{dI}{dV}(V)$ with a broadening function:

$$\begin{aligned}
\frac{dI}{dV}(V,\delta V) &\propto \int_0^{2\pi} \cos(t)\, I\left(V+\frac{\delta V}{2}\cos(t)\right) dt \\
&\overset{x=\cos t}{=} 2\int_{-1}^{1} \frac{x}{\sqrt{1-x^2}}\, I\left(V+\frac{\delta V}{2}x\right) dx \\
&= 2I\left(V+\frac{\delta V}{2}x\right)\left(-\sqrt{1-x^2}\right)\Big|_{x=-1}^{1} \\
&\quad - 2\int_{-1}^{1} \left(-\sqrt{1-x^2}\right)\frac{\delta V}{2}\frac{dI}{dV}\left(V+\frac{\delta V}{2}x\right) dx \\
&= \delta V \int_{-1}^{1} \sqrt{1-x^2}\,\frac{dI}{dV}\left(V+\frac{\delta V}{2}x\right) dx \\
&\overset{y=\frac{\delta V}{2}x}{=} 2\int_{-\delta V/2}^{\delta V/2} \sqrt{1-\left(\frac{2y}{\delta V}\right)^2}\,\frac{dI}{dV}\,(V+y)\, dy
\end{aligned}$$

After normalization, we obtain

$$g(E) = \begin{cases} \frac{4}{\pi}\frac{1}{e\delta V}\sqrt{1-\left(\frac{2E}{e\delta V}\right)^2} & -\frac{e\delta V}{2} < E < \frac{e\delta V}{2} \\ 0 & \text{otherwise} \end{cases} \tag{D.5}$$

with FWHM $\Delta = \frac{\sqrt{3}}{2} e\delta V$.

In lack of an analytical solution for the convolution, numerical values are given. $h(E)$ assumes its maximum at $E_M \approx 0.326115\, e\delta V \approx 0.377\, \Delta$, and the half-maximum at $E_{HM} \approx -0.223072\, e\delta V \approx -0.258\, \Delta$.

Note: Lock-in broadening has not been considered in the STS simulations, since the experimental peak-peak modulation of $\delta V = 2 \cdot 20\,\text{mV} \cdot \sqrt{2} \approx 56\,\text{mV}$ was significantly smaller than the effective broadening observed. It was verified that the effect of lock-in broadening on the simulated spectrum can be neglected.

D.3 Gaussian broadening

For completeness, we also provide results for Gaussian broadening

$$g(E) = \frac{1}{\sqrt{2\pi}\sigma} \exp\left(-\frac{E^2}{2\sigma^2}\right) \tag{D.6}$$

with FWHM $\Delta = \sqrt{8\ln(2)}\,\sigma$.

For the convolution, we obtain

$$h(E) = \frac{1}{\sqrt{2\pi}\sigma}\frac{\pi}{2}\sqrt{|E|}\exp\left(-\frac{E^2}{4\sigma^2}\right)\left[I_{-\frac{1}{4}}\left(\frac{E^2}{4\sigma^2}\right) + \text{sgn}(E) I_{\frac{1}{4}}\left(\frac{E^2}{4\sigma^2}\right)\right]$$

where $I_\alpha(x)$ denotes the modified Bessel function of the first kind.

In lack of analytical expressions for E_M and E_{HM}, numerical values are given. The maximum of $h(E)$ is assumed at $E_M \approx 0.764951\,\sigma \approx 0.325\,\Delta$, the half-maximum at $E_{HM} \approx -0.697669\,\sigma \approx -0.296\,\Delta$.

List of publications and author contributions

(I) Leopold Talirz, Hajo Söde, Jinming Cai, Pascal Ruffieux, Stephan Blankenburg, Rached Jafaar, Reinhard Berger, Xinliang Feng, Klaus Müllen, Daniele Passerone, Roman Fasel, and Carlo A. Pignedoli. „Termini of bottom-up fabricated graphene nanoribbons." In: *Journal of the American Chemical Society* 135.6 (Feb. 2013), pp. 2060–3. DOI: 10.1021/ja311099k.

The author performed all density functional theory calculations and Clar's theory considerations, devised and organized experiments concerning tip-induced dehydrogenation and wrote the manuscript with help from Carlo Pignedoli, Pascal Ruffieux and Roman Fasel.

(II) Jinming Cai, Carlo A. Pignedoli, Leopold Talirz, Pascal Ruffieux, Hajo Söde, Liangbo Liang, Vincent Meunier, Reinhard Berger, Rongjin Li, Xinliang Feng, Klaus Müllen, and Roman Fasel. „Graphene nanoribbon heterojunctions." In: *Nature Nanotechnology* 9.11 (Nov. 2014), pp. 896–900. DOI: 10.1038/nnano.2014.184.

The author performed DFT calculations of doped and undoped chevron GNRs and assisted Carlo Pignedoli in the calculation of the heterojunction.

(III) Hajo Söde, Leopold Talirz, Oliver Gröning, Carlo Antonio Pignedoli, Reinhard Berger, Xinliang Feng, Klaus Müllen, Roman Fasel, and Pascal Ruffieux. „Electronic band dispersion of graphene nanoribbons via Fourier-transformed scanning tunneling spectroscopy." In: *Physical Review B* 91.4 (Jan. 23, 2015), p. 045429. DOI: 10.1103/PhysRevB.91.045429.

The author contributed density functional theory calculations, FT-STS simulations and analytical models for broadening of the DOS and wrote the manuscript together with Hajo Söde and Pascal Ruffieux.

(IV) Leopold Talirz, Prashant Shinde, Daniele Passerone, and Carlo Antonio Pignedoli. „Synthesis of Atomically Precise Graphene-Based Nanostruc-

tures: a Simulation Point of View.“ In: *On-Surface Synthesis*. Ed. by Christian Joachim. Vol. 8. Advances in Atom and Single Molecule Machines. Springer (in press).

In this invited review, the author wrote the computational methods section, major parts of the introduction and revised the whole chapter for publication.

(V) Carlos Sánchez-Sánchez, Sebastian Brüller, Hermann Sachdev, Klaus Müllen, Matthias Krieg, Holger F. Bettinger, Adrien Nicolaï, Vincent Meunier, Leopold Talirz, Roman Fasel, and Pascal Ruffieux. „On-Surface Synthesis of BN-Substituted Heteroaromatic Networks.“ In: *ACS Nano* 9.9 (Sept. 22, 2015), pp. 9228–9235. DOI: 10.1021/acsnano.5b03895.

The author performed DFT-based STM simulations in order to pin down the orientation of the borazine core in the molecular network.

Works in preparation

(VI) Leopold Talirz, Hajo Söde, Shigeki Kawai, Akimitsu Narita, Pascal Ruffieux, Xinliang Feng, Klaus Müllen, Roman Fasel, and Carlo Antonio Pignedoli. „Band gap of atomically precise graphene nanoribbons as a function of ribbon length and termination.“ In preparation.

The author performed Clar's theory considerations as well as tight binding and DFT calculations, identified the dependence of the band gap on termination and developed the model for its length-dependence.

(VII) Shiyong Wang, Leopold Talirz, Klaus Müllen, Roman Fasel, and Pascal Ruffieux. „Edge state splitting at atomically precise graphene zigzag edges.“ Submitted.

The author performed electronic structure calculations of finite 7-AGNRs within DFT and GW (up to 100 atoms) and contributed major sections to the manuscript.

(VIII) Hajo Söde, Leopold Talirz, Carlo Antonio Pignedoli, Reinhard Berger, Xinliang Feng, Klaus Müllen, Roman Fasel, and Pascal Ruffieux. „Synthesis and characterization of atomically precise N=9 armchair graphene nanoribbon.“ In preparation.

The author performed DFT-based STS simulations and generalized the findings concerning the STS intensity of frontier bands by a symmetry analysis.

(IX) Pascal Ruffieux, Shiyong Wang, Bo Yang, Carlos Sanchez, Jia Liu, Thomas Dienel, Leopold Talirz, Prashant Shinde, Carlo A. Pignedoli, Daniele Passerone, Tim Dumslaff, Xinliang Feng, Klaus Müllen, and Roman

Fasel. „On-surface synthesis of graphene nanoribbons with zigzag edge topology.“ Submitted.

The author calculated the band structure and density of states of the 6-ZGNR within the GW approximation.

Closing remarks and acknowledgements

When Daniele Passerone first got me interested in the science carried out at the nanotech@surfaces lab, it was the spring of 2009. There was promising experimental data on newly synthesized phthalocyanine-based nanowires and it seemed like a good opportunity for a Master's thesis to try rationalizing these wires' high conductivity based on *ab initio* simulations. While the calculations were done relatively quickly, they were not able to explain the experimental findings. Further, temperature-dependent measurements would have to be performed in order to pin down the mechanism of conduction.

The tiny dimensions of these wires, paired with the weak resistance of molecular crystals to electron and ion beams, made the experiments rather challenging for an inexperienced Master's student. After some unsuccessful initial attempts, the project was postponed, allowing me to complete the Master's thesis in Bertram Batlogg's group at ETH (testing the gelation of ionic liquids for use as gate dielectrics in organic field effect transistors). However, experiments on the original project continued and when I started my Ph.D. at the nanotech@surfaces lab in the summer of 2011, the tentative title of my thesis was "Organic nanowires with unusual transport properties – a theoretical study".

Although the final thesis does not include any of the results obtained in this line of research, I need to begin by thanking the very many people that have helped me in this quest. My thanks go to Susanne Dröscher and Theodore Choi from the Ensslin group for helping me produce a suitable wafer and depositing electrodes via electron-beam lithography. At the Batlogg group, I thank Jakob Kanter and Philipp Moll for shooting at tiny nanowires with ion guns and for never being short of new crazy ideas to measure the wires – alignment by dielectrophoresis, contactless resistivity measurements, you name it! Thanks go to Thomas Mathis for his help in performing temperature-dependent resistivity measurements inside glove boxes and, of course, for being a great captain of the SC60 team during our five-year domination of the Boltzmann soccer cup at the ETH physics department. At Empa, I want to thank Fabio Lamattina, Ivan Shorubalko and Michael Stiefel, who not only let me use their micromanipulator station and scanning electron microscope, but also contacted wires

with the helium focused ion beam and produced a set of electrodes, allowing me to measure their resistivity without having to worry about high-energy particles bombarding the sensitive wires. Juan-Ramon Sanchez took time off his busy schedule to grow the nanowires at Empa, and Stefan Egger performed nanostenciling experiments, which might (or might not) turn out to be the final nail in the coffin of this project – thank you!

Luckily, members of the nanotech@surfaces lab were working also on other topics that provided exciting opportunities for atomistic simulations. Over the course of the Ph.D. studies, my focus shifted more and more towards the bottom-up fabrication of graphene nanoribbons. I would like to thank Roman Fasel and Pascal Ruffieux for trusting me with the work on the termini of the 7-AGNRs, which turned out to be a very interesting and gratifying entry point to the field. I have learned a great deal from your scientific expertise as well as your patient advice and mindful comments on writing scientific papers and giving presentations. My heartfelt thanks go to Oliver Gröning for always being available for discussions, for many great lessons concerning tight binding and for never turning down a request for new calculations. I am much obliged to Hajo Söde, for being my main and ever reliable experimental partner and for always remaining in good spirits, even in the face of tedious new experiment proposals. In general, I would like to thank the experimentalists in the nanotech@surfaces team for always being friendly to a "theorist" outside of his natural territory, peeking over their shoulder in the lab and asking trivial questions (or even worse – not so trivial questions) about their work.

In the theory division, I thank Daniele Passerone for bringing me to Empa in the first place and for introducing me to the world of atomistic simulations. I particularly enjoyed the amicable atmosphere in your group, where people look out for each other and feel free to joke and laugh together (tolerating even my enduring refusal of the fundamental after-lunch coffee!). Thanks go to all members of the group, in particular to Roberto Gaspari who introduced me to STM simulations and Andrea Benassi who introduced me to the inexhaustible abundance of Italian profanity. I am indebted to Andrea Ferretti for being an incredibly kind host during my stay in Modena in 2012, for making me realize that I need to change operating systems and for setting my personal benchmark in terms of programming speed. Finally, I would like to thank my supervisor Carlo Pignedoli. Not only was he available day and night to discuss my numerous scientific questions, he also cared deeply about my scientific development and professional career, giving me the opportunity to attend numerous fascinating work shops and introducing me to his esteemed scientific contacts in Italy. I consider myself very fortunate to have been a Ph.D. student under his supervision – thank you for making it the wonderful time that it was!

At the University of Zurich, I thank Jürg Hutter for kindly agreeing to be my doctoral adviser. Thanks go to Ari Seitsonen for fun times during the preparation of molecular dynamics exercises and to Dorothea Golze and Ralph

Koitz for advice regarding CP2K and always keeping me up to date with the latest news in the group. Furthermore, I thank the members of the doctoral committee, Jürg Osterwalder, Oleg Yazyev and Thomas Greber for taking the time to evaluate and discuss this thesis.

I gratefully acknowledge funding from the Swiss National Science Foundation, who have been very understanding concerning the challenges faced in the original line of research and generously supported the completion of the research line of the nanoribbons by granting a one-year extension. Financial support from the CMSZH graduate school is acknowledged for the attendance of two conferences as well as for the printing of this thesis.


CMSZH
CHEMICAL MOLECULAR SCIENCES ZURICH
GRADUATE SCHOOL